Selective catalytic reduction for 'light-duty' diesel engines using ammonia gas

Sturgess, M. P.

Award date:
2012

Awarding institution:
Coventry University

Coventry University Automotive Engineering Applied Research Group in
collarboration with Jaguar Land-Rover, Faurecia, Johnson Matthey, and EPSRC

Selective Catalytic Reduction for 'Light-Duty' Diesel Engines using Ammonia Gas

A thesis submitted in partial fulfilment for
'Doctor of Philosophy'

M P Sturgess

April 2012

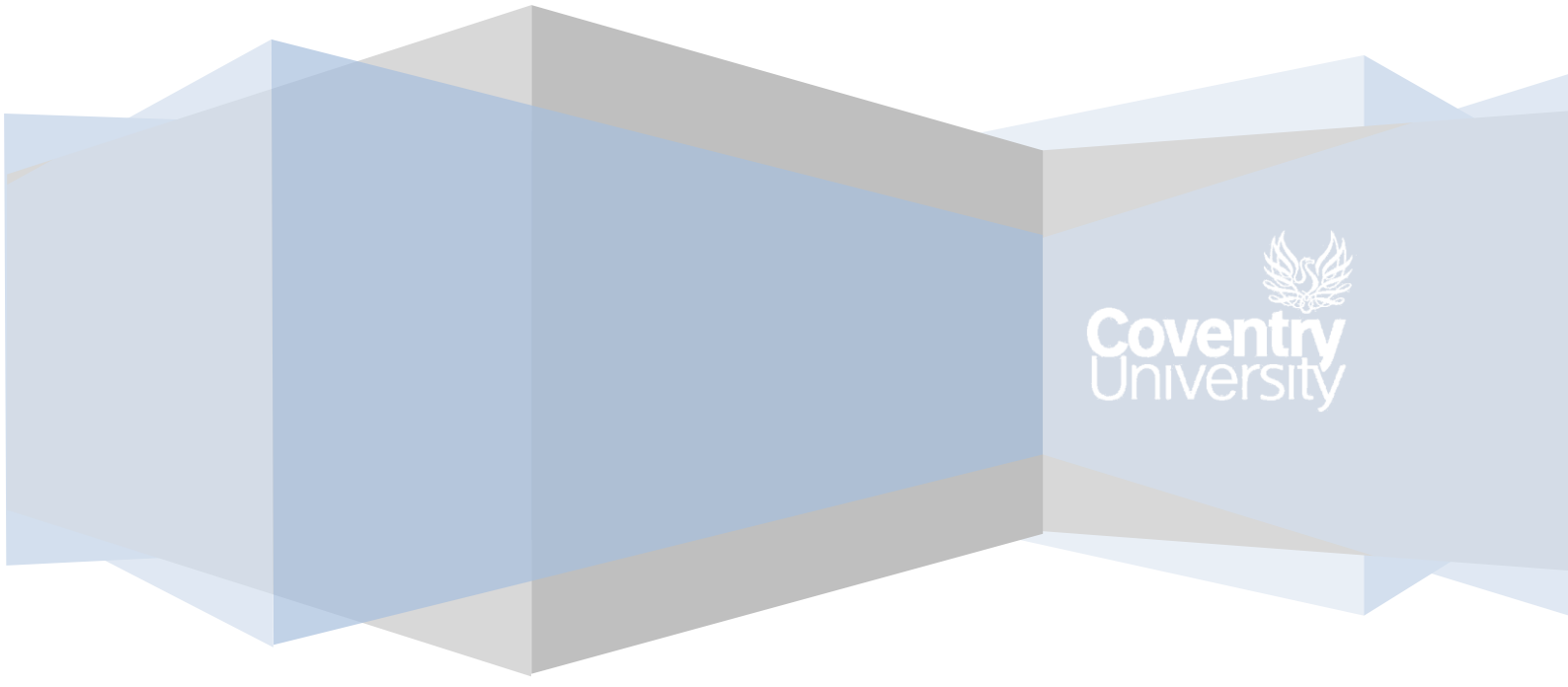

Contents

Abstract

This thesis describes an investigation into the spatial species conversion profiles of a Cu-zeolite SCR under engine conditions at low exhaust gas temperatures; this was then compared with a CFD model that models the catalyst via a porous medium measuring 5 x 5 x 91 cells assuming a uniform cross-sectional flow distribution. Species conversion rates were sampled at fixed points in the axial direction. The analysis of the spatial conversion profiles is a more rigorous method in assessing the ability of a mathematical model to predict the experimental data. It can also assist in the optimisation of the catalyst size, minimising packaging requirements and manufacturing costs.

The experiments were undertaken on a light-duty diesel engine at a speed of 1500rpm, and at a load of 6bar BMEP; this provided exhaust gas temeraqtures between 200 and 220°C. NO_2: NO_x ratios were controlled by changing the size and position of the diesel oxidation catalyst, the inlet NH_3: NO_x ratio was also also varied, ammonia gas was used instead of urea for the purposes of simlicity. The advantage of testing on an actual engine over lab-babed studies is that the conditions such as exhaust gas composition are more realistic. A 1D CFD model was constructed using the 'porous medium approach' with kinetics obtained from open literature. Results from the simulations were then compared with the experimental data for the same engine conditions.

It was observed that the majority of the NO_x conversion took place in the first half of the brick for all NH_3: NO_x ratios investigated, and that the formation of N_2O via NO_2 and ammonia had the same influence as the 'fast' SCR reaction just after the inlet, which the CFD model failed to predict for the base case analyses. The influence of the inlet ammonia on the model was also noticed to be greater than in the experiments. Simple transient analyses were also undertaken on the short SCR bricks for NO_2: NO_x ratios of 0.6 and 0.07, and it was observed that the response time to steady-state was noticeably higher in the experiments than in the model.

Modifications made to the model, including decreasing the influence of the 'fast' SCR reaction, and the addition of an empirical term onto the ammonia adsorption provided a noticeably better agreement for different NH_3: NO_x injection ratios. The desorption kinetics in the model were also altered by increasing the strength of the bonding of the ammonia onto the adsorption sites.This improved the transient agreement between the model and the experiments, but reduced the steady-state concentrations at the exit of the brick for all NH_3: NO_x ratios investigated.

Acknowledgements

The author would like to acknowledge the following people for their assistance in the completion of this thesis:

Professor Stephen Benjamin for his support and input throughout this study. Doctor Carol Roberts for her input and advice, particularly on the CFD studies.

Mr Robert Gartside for his assistance and expertise in the undertaking of the engine tests. Mr Gary Deakin from Froude Hofmann for helping in setting up and commissioning of the engine test cell. The help of Colin, Barry, Martin, Steve, and Lawrence for the manufacruring of key exhaust components is also greatly appreciated.

Rick Spurgeon, Jason Turnbull, and Brad Moyler from Horiba for help in keeping the analysers in working condition, and their input with regards to the ammonia scrubbers and analyser maintenance.

Froude Hofmann and CD-Adapco are also acknowledged for allowing he eingine tests to be undertaken at their facility, and supplying and providing valuable assistance with STAR CD version 4 respectively.

The following external parties are also acknowledged, with whom this study was undertaken in collaboration with:

Harry Christer and Doctor Andrew Hatton from Faurecia for supplying exhaust components, for canning the catalyst bricks, and for their inputwith regards to the CFD modelling. Doctor Steve Pearson and Paul Duggelby from Jaguar Land-Rover for their input with regards to the engine testing and CFD modelling. Doctor Graham Avery from Johnson Matthey for being able to supply the diesel oxidation catalysts, the SCR bricks and for his input throughout the project.

The research grant for this project was provided by EPSRC.

Nomenclature

Standard Symbols

Symbol	Description	Units
A	Cross-sectional area.....	m^2
A_v	Reactor surface area per unit-volume.....	$m^2.m^{-3}$
BaO	Barium Oxide.....	-
CFD	Computational Fluid Dynamics.....	-
CH_4	Methane.....	-
C_3H_6	Propane.....	-
C_i	Concentration of species *i*.....	*Units are equation specific
$C_{i\text{-}gas}$	Concentration of species *i* in the gas phase.....	*Units are equation specific
$C_{i\text{-}sol}$	Concentration of species *i* in the solid phase.....	*Units are equation specific
CLD	Chemiluminescense detector.....	-
CO	Carbon Monoxide.....	-
CO_2	Carbon Dioxide.....	-
$CO=(NH_2)_2$	Urea.....	-
$Cp\text{-}_{Gas}$	Specific heat in the gas phase.....	$kJ.kg.K^{-1}$
Cu	Copper.....	-
D	Diffusivity coefficient.....	$m^2.s^{-1}$
D_h	Hydraulic diameter.....	m
DOC	Diesel oxidation catalyst.....	-
DPF	Diesel particulate filter.....	-
E_A	Activation energy.....	$kJ.mol^{-1}$
ECU	Engine control unit.....	-
EGR	Exhaust gas re-circulation.....	-
EPA	Environmental Protection Agency.....	-
ETC	European Transient Cycle.....	-
EUDC	Extra Urban Drive Cycle.....	-
f	Fanning friction factor.....	-
Fe	Iron.....	-

Symbol	Description	Units
FID	Flame ionisation detector	-
FT	Federal Tier	-
FTIR	Fourier transform infrared detector	-
GHSV	Gas hourly space velocity	hr^{-1}
h	Convection heat transfer coefficient	$W.m^{-2}.K^{-1}$
H_2	Hydrogen	-
HC	Hydrocabons	-
HCNO	Isocyanic acid	-
HGV	Heavy goods vehicle	-
HNO_3	Nitric acid	-
H_2O	Water	-
H_2SO_4	Sulphuric acid	-
JC	Japanese City	-
k	Reaction rate constant	-
k_{Gas}	Thermal conductivity in the gas phase	$W.m^{-1}.K^{-1}$
K	Mass transfer coefficient	$m.s^{-1}$
K_{Bulk}	Total mass transfer coefficient	$m.s^{-1}$
LNT	Lean NO_x Trap	-
m_i	Mass of species *i*	kg
$\dot{m}$	Exhaust gas mass flow rate	$kg.s^{-1}$
MF	Mass fraction	-
MM_i	Molecular mass of species *i*	$mol.m^{-3}$
N_2	Nitrogen	-
NDIR	Non-dispersive infrared detector	-
NH_3	Ammonia	-
NH_4NO_3	Ammonium nitrate	-
NO	Nitric oxide	-
NO_2	Nitrogen dioxide	-
N_2O	Nitrous oxide	-

Symbol	Description	Units
NO_x	Oxides of nitrogen.....	-
Nu	Nusselt Number.....	-
O_2	Oxygen.....	-
O_3	Ozone.....	-
O_i	Stoichiometric coefficient of species *i*.....	-
PM	Particulate matter.....	-
P_{O2}	Mole fraction of oxygen (equation (23)).....	-
PPM	Particles per million.....	ppm
Pt	Platinum.....	-
q	Mass transfer.....	$kg.m^{-2}.s^{-1}$
$\dot{Q}$	Heat transfer.....	$W.m^{-3}$
r_i	Reaction rate of species *i*.....	$mol.mol\text{-}sites^{-1}.s^{-1}$
$r_{i\text{-}\Omega}$	Reaction rate of species *i* when multiplied by the number of available reaction sites (Ω).....	$mol.m^{-3}.s^{-1}$
$r_{i\text{-}Cons}$	Reaction rate of species *i* (consumption) (Appendix 2.3.3).....	$mol.m^{-3}.s^{-1}$
$r_{i\text{-}Prod}$	Reaction rate of species *i* (production) (Appendix 2.3.3).....	$mol.m^{-3}.s^{-1}$
R	Gas constant.....	$kJ.mol^{-1}$
Re	Reynolds Number.....	-
Re_c	Reynolds Number inside the monolith channels.....	-
SCR	Selective Catalytic Reduction.....	-
SO_2	Sulphur dioxide.....	-
t	Time.....	s
T	Temperature.....	°C (Unless specified)
T_{Gas}	Gas temperature.....	°C (Unless specified)
T_{Sol}	Solid temperature.....	°C (Unless specified)
T_{Mean}	Mean temperature.....	°C (Unless specified)
Th	Wall thickness.....	m

Symbol	Description	Units
THC	Total hydrocarbons.....	-
TiO_2	Titanium oxide.....	-
U	Inlet (superficial) velocity.....	$m.s^{-1}$
U_C	Channel velocity.....	$m.s^{-1}$
US	United States.....	-
$\dot{V}$	Exhaust gas volume flow rate.....	$m^3.s^{-1}$
V_2O_5	Vanadium.....	-
V_W	Catalyst pore volume per unit volume of the catalyst..	$m^3.m^{-3}$
W_c	Washcoat thickness.....	m
x	X axis.....	-
y	Y axis.....	-
z	Z axis.....	-
Z_{NH3}	Number of available ammonia storage sites (equation (30), and equations (33) – (36).....	-
$Z^*_{NH3}(S)$	Ammonia surface coverage (equation (30), and equations (33) – (36).....	-

Greek Symbols

Symbol	Description	Units
α_1	NH_3: NO_x injection ratio.....	-
α_2	Permeability coefficient (equations (60) and (61)).....	-
α_3	Arbitrary constant determining the strength of the bonding of ammonia molecules to the storage sites on the catalyst.....	-
β_1	Power term (equation (23)).....	-
β_2	Permeability coefficient.....	-
γ	Parameter for surface coverage dependence.....	-
ε_1	Constant (equation (25)).....	-
ε_2	Monolith porosity.....	-
θ	Surface coverage of component.....	-

Symbol	Description	Units
λ	Logging interval.....	Hz
Λ	Power term (Appendix 2.3.3).....	-
μ	Dynamic viscosity.....	$kg.m^{-1}.s^{-1}$
ν	Kinematic viscosity.....	$m^2.s^{-1}$
$\left\lvert\vec{v}\right\rvert$	Inlet velocity on the z-plane (equation (60)).....	$m.s^{-1}$
ρ	Density.....	$kg.m^{-3}$
ρ_{Gas}	Density of air in the gas phase.....	$kg.m^{-3}$
ρ_{Sol}	Density of air in the solid phase.....	$kg.m^{-3}$
ω_i	Molecular mass ratio for species *i*.....	-
Ω	Number of available reaction sites.....	$mol\text{-}sites.m^{-3}$
σ_s	Turbulent Schmidt Number.....	-

List of Figures

The numbering of the figures relates to the chapter of the report, which is the first digit, and the image number.

List of Tables

The numbering of the tables relates to the chapter of the report, which is the first digit, and the image number.

Chapter 1: Introduction

1.1 Background

Diesel engines have been seen as a popular alternative to petrol engines for automotive applications over the past few years due to their superior fuel economy and lower CO_2 emissions than their equivalent petrol counterparts. The main disadvantages of using diesel engines are an increase in NO_x emissons, and particulate matter.

NO_x, or oxides of nitrogen, is made up of NO and NO_2. Although small amounts of NO can prove beneficial to human health as it increases vasodilation of the blood cells, and kills viruses and tumour [Miller, 1995], excessive exposure could cause drowsiness, irritation of the eyes, and lead to unconsciousness. NO_2 can be considered more hazardous to human health, as even exposure to very small quantities can lead to conditions such as pulmonary edema, bronchitis, respiratory problems, and emphysema. Because of the issues posed to human health, governments have begun to adopt regulations limiting the amount of NO_x emitted by road vehicles.

1.2: Emissions Regulations Overview

Fig 1.1 provides an overview of the current regulations being put into practice. It can be seen that there is a trend in how the more established economies, such as the US, those in the EU, and Japan have more stringent regulations than the emerging economies.

Fig 1.1: Emissions laws for passenger cars currently in operation around the world. NO_x values for China and India are based on those in implemented across those countries. [Dieselnet, 2007]

Emissions regulations in the US are governed by the 'Environmental Protection Agency' or the EPA for short. Currently the US employs 'Federal Tier 2' regulations, however California, Connecticut, New Jersey and Rhode Island employ the 'California' emissions regulations.

In the countries that are members of the European Union, Euro V is currently in use, which will be replaced by Euro VI in 2014.

The regulations governing engine emissions in Japan, are the second most stringent in the world with regards to NO_x emissions, behind the US. In 2009 new and more stringent regulations were introduced, where the mean NO_x emissions must not exceed $0.08 g.km^{-1}$.

China and India are two of the worlds fastest growing economies, they are also two of the most densely populated, each with a population in excess of a billion people. In recent years China's greenhouse gas emissions have eclipsed those produced by the US, and they are predicted to only increase further. The emissions regulations in China are based on the Euro IV protocol, with Euro V being introduced to Bejing in 2012, however, different different drive cycles are used; 6this could have an impact on emissions levels. [Dieslenet, 2011]

The nationwide emissions regulations employed in India are based on Euro III, with the Bharat Stage IV regulations, which are based on Euro IV laws, currently in operation in the national capital region, and the 11 biggest cities. [Dieselnet, 2009]

1.3 Drive Cycles

Each government employs a standard drive cycle to evaluate a vehicle's emissions levels before that vehicle can legally go into production. Fig 1.2 and Fig 1.3 display the two drive cycles employed by the EU and Japan respectively.

Fig 1.2: ECE 15 urban drive cycle. The EUDC was added to simulate faster driving. [Dieselnet, 2007] The ECE 15 section is designed to simulate the stop-start conditions of a busy urban road, such as Paris, London, and Rome.

Fig 1.3: Japan's JC08 drive cycle compared with the original 10-15 modes cycle. [Dieselnet, 2007]

The JC08 cycle described in Fig 1.3 is designed to be more aggressive than the previous 10-15 modes cycle, also a greater range of driving conditions are also covered. Emissions are measured under both 'cold' and 'warm-start' conditions. The cycle is also considerably more rigorous on vehicle fuel economies and emissions levels. [Green Car Congress, 2007]

It is observed that both drive cycles are very similar with a particular emphasis being placed on acceleration and deceleration, which has a particularly strong effect on emissions levels, therefore the transient performance of an after-treatment system could be considered to be of considerable importance.

1.4 Concluding Remarks

It can be seen that due to the potential risks posed to human health, the reduction of NO_x emissions from road-based vehicles is an important consideration for designers and manufacturers of diesel engines, particularly if they are to meet with the ever more stringent emissions regulations.

The introduction of new drive cycles provides a more rigorous assessment of the vehicles' capability to reach the emissions targets. Combined with the ever-tightening legislation, the use of specialist NO_x after-treatment systems is becoming more common amongst manufacturers for both heavy and light-duty diesel vehicles.

A greater understanding of the performance of NO_x after-treatment systems is therefore very important, particularly for meeting increasingly stringent emissions regulations whislt minimising the effect on engine performance and costs.

Chapter 2: Literature Review

2.1 Overview

One of the main drawbacks in the reduction of NO_x emissions produced by diesel vehicles is that diesel engines operate under 'lean' conditions, where there is a high amount of oxygen present in the exhaust ; this means that reduction of NO_x using a conventional three-way catalyst is incredibly difficult. Whilst NO_x reduction is possible, it can have a negative effect on the fuel economy of the engine. [Kaneko et al, 1975] and [Khair et al, 2000].

Currently the most common method of NO_x reduction is to use 'Exhaust Gas Recirculation' (EGR). More recently, however, two new promising reduction techniques are being investigated: 'Lean NO_x Traps' (LNT), and 'Selective Catalytic Reduction' (SCR).

2.2 NO_x Emission Reduction Systems

2.2.1 Exhaust Gas Re-Circulation

Fig 2.1 displays a simple diagram of an EGR system. EGR has been used as a NO_x reduction technique for both diesel and petrol engines for some considerable time, up to 20% of the exhaust gas is capable of being re-circulated. [Hawley et al, 1999] and [Khair et al, 2000].

EGR involves re-injecting some of the exhaust gas from the manifold and dumping it back into the engine. The use of an EGR system can reduce emissions by up to 50%, although an increase in PM is likely to arise. [Khair et al, 2000]

Fig 2.1: Typical EGR setup. [Electropaedia, 2005]

One of the main disadvantages of using EGR is that it can impact on engine durability, particularly with heavy-duty diesel engines. The main components subjected to wear on a diesel engine when using EGR are the piston rings, the cylinder, and the oil. The use of aged oil is limited with regards to neutralising acid effects, which is caused by the sulphur content in the fuel that could increase the wear rate on both the liner and the piston rings, especially with EGR levels as low as 15%. The presence of

soot in the exhaust might also inhibit the anti-wear additives in the oil. [Dennis et al, 1999] Some doubt may arise as to whether the effects experienced with heavy-duty diesels are present in smaller power plants.

Alone, high NO_x reduction levels, as seen with LNTs and SCRs may be extremely hard to replicate using EGR. A 100% NO_x reduction would be impossible under any conditions with an EGR unless nearly all of the exhaust gas was to be re-circulated.

2.2.2 Lean NO_x Traps

LNTs store NO_x under lean conditions and release the NO_x under rich conditions (when very little O_2 is present). One of the advantages of using LNTs is that a second reductant is not needed as diesel fuel can be used as a purging agent when the trap has adsorbed its maximum capacity of NO_x. LNTs can also be used on spark ignition engines. [Asik et al, 2000] A simple schematic of an LNT system is shown in Fig 2.2:

Fig 2.2: A typical NO_x trap. The hydrocarbons are injected prior to the trap. [Autoblog, 2008]

NO_x traps are essentially three-way catalysts that contain either alkali metals or alkali-earth metals. An oxidation catalyst is usually located upstream of the trap. As the gas enters the trap under lean conditions, NO_2 is formed via the oxidation of NO; this is then adsorbed onto the trap via the precious metal to form nitrates. [Alimin, 2010] Once the trap is full, hydrocarbons are injected into the exhaust to consume the oxygen; the NO_x is then released from the trap and can react with CO, HC, or H_2.

Equation (1) the oxidation of NO before and on the trap; this reaction is not considered to be rate determining as it is very fast [Benjamin et al, 2007]:

$$2NO + O_2 \leftrightarrow NO_2 \qquad (1)$$

The NO_2 is then absorbed onto an alkali metal or an alkali earth metal on the catalyst surface (in this case barium oxide (BaO) as explained in equation (2) [Benjamin et al, 2007]:

$$4NO_2 + 2BaO + O_2 \rightarrow 2Ba(NO_3)_2 \qquad (2)$$

Once the trap has reached its full storage capacity the oxygen in the exhaust is removed by injecting hydrocarbons (in this case propane, however, diesel can also be used):

$$2C_3H_6 + 9O_2 \rightarrow 6CO_2 + 6H_2O \quad (3)$$

Under these conditions the NO_x is purged from the trap as NO, and then reacts with, C_3H_6, CO and H_2 with the primary reductant being CO [Alimin, 2006]:

$$2CO + 2NO \rightarrow 2CO_2 + N_2 \quad (4)$$

$$2H_2 + 2NO \rightarrow 2H_2O + N_2 \quad (5)$$

$$2C_3H_6 + 18NO \rightarrow 6CO_2 + 6H_2O + 9N_2 \quad (6)$$

After regeneration it can be expected that some of the adsorbed NO may be released from the DOC and pass directly through the trap. [Alimin, 2006] Fig 2.3 describes the reaction process during lean-burning and rich burning, and also provides a schematic of the catalyst:

Fig 2.3: Trap schematic including burning phases and conditions. [Cataler, n.d.]

One of the main inhibiters in the functioning of a LNT is sulphates in the exhaust gas that are preferentially adsorbed by the trap; this effect is amplified for fuels with higher sulphur content.

Whilst LNTs are still considered to be a promising method of NO_x reduction, they have considerable disadvantages. Although they don't require a second reactant, the use of fuel as the reductant can have an effect on the fuel efficiency of the vehicle, storage and overall efficiencies are low (28-33% and 22-28% respectively [Alimin, 2006]) at low temperatures, and to avoid preferential adsorbing of sulphur compounds a low sulphur based fuel would need to be used. LNTs are also very difficult to control effectively.

2.2.3 Selective Catalytic Reduction

SCR technology is already a well established technology for reducing NO_x emissions from stationary diesel engines, but recently this technology has been investigated for mobile power plants, such as cars, trucks, and buses. Advantages of using an SCR system include: being cost effective and a better fuel economy than LNTs, diesel is not used as a NO_x reductant, and they also require a less complicated control system. There is also very little loss in engine performance.

SCR systems usually include a three-way (oxidation) catalyst, a particulate filter, a urea/ammonia injector, and another catalyst (SCR catalyst). As the exhaust gas enters the oxidation catalyst some of the NO reacts with O_2 to form NO_2, which can aid in the NO_x conversion efficiency. An aqueous-urea

solution is then injected; this decomposesinto ammonia and water. The ammonia then reacts inside the SCR to form atmospheric nitrogen and water. Fig 2.4 shows a typical SCR system:

Fig 2.4: A typical SCR assembly. The urea/ammonia is injected upstream of the SCR catalyst. [The Auto Industrie Blog, 2008]

Vanadium and zeolite are the most common types of catalyst, although other catalyst materials can also be used. [Hamada et al ,2005].

2.2.4 Summary

It can be seen that although EGR is a widely used method, the limitations on the amount of exhaust gas that can be recirculated mean that its long-term suitability for complying with the ever more stringent regulations is limited. Therefore an additional or replacement system would be required.

Although LNT's do not require a separate reductant, the less complicated control system, better fuel economy, and potential for high NO_x conversion rates make SCR systems an attractive technology for NO_x reduction for automotive applications. Whilst it is possible use LNT+SCR systems [Theis et al, 2006], the increased production costs, packaging requirements, and the complexity of the control system could mean that this would be unsuitable for automotive applications, particulary passenger cars.

2.3 SCR Overiew

2.3.1 SCR Reactions with Ammonia

Equations (7) – (9) describe the three principle reactions that take place inside the SCR catalyst involving NO_x and ammonia:

$$4NH_3 + 4NO + O_2 \rightarrow 6H_2O + 4N_2 \quad (7)$$

$$4NH_3 + 3NO_2 \rightarrow 6H_2O + 7N_2 \quad (8)$$

$$2NH_3 + NO + NO_2 \rightarrow 3H_2O + 2N_2 \quad (9)$$

where reaction schemes (7), (8), and (9) can be labelled as 'standard,' 'slow,' and 'fast' respectively.

The 'standard' SCR reaction is the predominant reaction when the NO content is higher than 90% [Khair et al ,2000]. The most desirable reaction, however, is equation (9), known as the "fast" SCR reaction; this can provide a considerable improvement in the low-temperature conversion rate. [Ciardelli et al, 2004] and [Koebel et al, 2002].

The 'fast' SCR reaction is the most sought after reaction, particularly for light-duty applications as it offers much improved NO_x reduction rates at lower exhaust gas temperatures, as shown in Fig 2.5:

This graph has been removed due to third party copyright. The unabridged version of the thesis can be viewed at the Lanchester Library, Coventry University

Fig 2.5: Steady-state NO_x conversion for different NO_2: NO_x ratios at varying temperatures for a vanadium-based catalyst. [Ciardelli et al, 2007]

The data obtained in Fig 2.5 was for V-based catalysts, however, since the 'fast' SCR reaction has a higher low-temperature activity on zeolite-based catalysts, the NO_x conversion rate would be expected to be higher, although the basic profiles are expected to be quite similar.

The fast SCR reaction has two different mechanisms, each depending on the catalyst material used. The first mechanism is based on catalyst re-oxidation by NO_2; this is more predominant over V_2O_5 based catalysts than over zeolites as zeolite does not have the tendency to oxidise very well when compared to V_2O_5.

The re-oxidation scheme is based on NO_2 acting as a more efficient oxidising agent than O_2 as an intermediate step for SCR reactions for V2O5 at temperatures between 300°C and 450°C. [Koebel et al, 2002] Equation (10) describes this [Koebel et al, 2002]:

$$2V^{+4}OH + NO_2 \rightarrow 2V^{+5}{=}O + NO + H_2O \quad (10)$$

A preferred mechanism for the "fast" SCR reaction is the 'nitrate route' [Ciardelli et al, 2004], as it provides a considerably quicker reaction than the re-oxidation scheme at lower temperatures. Instead of

re-oxidising the catalyst surface, NH_4NO_3 is formed on the catalyst surface from a reaction with ammonia and NO_2.

$$4NH_3 + 4NO_2 \rightarrow 2NH_4NO_3 + 2N_2 + 2H_2O \quad (11)$$

$$2NH_4NO_3 \leftrightarrow 2NH_3 + 2HNO_3 \quad (12)$$

$$NO + 2HNO_3 \rightarrow 3NO_2 + H_2O \quad (13)$$

Summing equations (12) and (13) gives:

$$2NH_4NO_3 + NO \rightarrow 3NO_2 + 2NH_3 + H_2O \quad (14)$$

Adding equation (11) to equation (14) gives:

$$4NH_3 + 4NO_2 + 2NH_4NO_3 + NO \rightarrow 2NH_4NO_3 + 2N_2 + 3NO_2 + 2NH_3 + 3H_2O$$

Simplifying this leads to:

$$2NH_3 + NO + NO_2 \rightarrow 3H_2O + 2N_2 \quad (15)$$

It is observed that the role of NH_4NO_3 is purely as an intermediate within the reaction as it is featured on both sides of the reaction scheme. [Ciardelli et al, 2004] If this scheme is believed to be faster than the re-oxidation method, it could be observed that with zeolite's apparent unwillingness to re-oxidise, 'fast' SCR reactions that do occur over zeolite can be attributed to nitrate formation. The formation of surface nitrates is also a more efficient method for converting NO, rather than as a method of catalyst re-oxidation, as described in equation (14). [Tronconi et al, 2007]

Although the 'standard' SCR reaction has been comprehensively investigated, due to its suitability for heavy-duty applications, such as power stations, there is currently only a limited amount of knowledge on the kinetics of the more complex 'fast' SCR reaction, particularly with zeolite-based SCRs.

One of the potential drawbacks with using SCR technology is the occurrence of ammonia slip, or the unreacted ammonia exiting the exhaust pipe. The amount of ammonia slip depends on the upstream NH_3: NO_x ratio (denoted by α_1 in this study) , the exhaust gas temperature, and the temperature of the catalyst formulation. Figs 2.6 andd 2.7 plot the ammonia slip against the catalyst temeperature for different values of α, ranging from 0.7 to 2.0.

Fig 2.6: Ammonia slip for different inlet NH_3: NO_x ratios for an SCR catalyst formulated at a low temperature. [Girard et al, 2007]

Fig 2.7: Ammonia slip for different inlet NH_3: NO_x ratios for an SCR catalyst formulated at higher temperatures. [Girard et al, 2007]

It is observed in Fig 2.6 and Fig 2.7 that the ammonia slip becomes less apparent at higher exhaust gas temperatures; this can be attributed to improved NO_x conversion for NH_3: NO_x ratios of < 1, and for higher ratios, where the excess ammonia is surplus to requirements; this oxidises as described in equation (16):

$$4NH_3 + 3O_2 \rightarrow 2N_2 + 6H_2O \quad (16)$$

Catalyst formulation is also observed to play a considerable role in governing the levels of un-reacted ammonia exiting the exhaust system, where SCRs formulated at lower temperatures perform better than the ones at higher temperatures in minimising ammonia slip.

To limit the amount of ammonia slip it is desirable to optimise the NH_3: NO_x ratio via closed-loop control. Oxidation catalysts can also be placed downstream of the SCR to convert any un-reacted ammonia. [Nakayama et al ,2006], [Servati et al, 2005], and [Tennison et al, 2004].

2.3.2 Species Adsorption

The performance of a catalyst not only depends on its active temperature, but also its ability to absorb/desorb different species. The primary species of interest is ammonia for SCR catalysts.

Fig 2.8 plots typical ammonia and NO transient behaviour over an SCR catalyst, where ammonia and NO are injected into a micro-reactor as step inputs for a certain period of time, then shut off. As one can witness, there is a considerable response time for the outlet ammonia levels to reach the inlet levels; this delay can be attributed to ammonia adsorption taking place on the catalyst surface. The adsorption period occurs roughly for the first 500 seconds, until subsequently no more ammoniacan be adsorbed.

Fig 2.8: Ammonia and NO adsorption/desorption for an exhaust gas temperature of 220°C [Lietti et al, 1998].

After the ammonia 'shut-off', ammonia is still being detected, due to catalyst desorption taking place. One may also notice that A_2 is smaller than A_1; this indicates that some of the ammonia is strongly absorbed onto the catalyst surface [Lietti et al, 1998], to fully desorb the catalyst of ammonia it is necessary to increase the exhaust gas temperature.

Graph B in Fig 2.8 displays the effect of NO adsorption onto the catalyst washcoat, it shows that NO adsorption is minimal, and therefore, for mathematical modelling, can be neglected. Oxygen adsorption can also play a significant role in NO_x reduction for V_2O_5-based catalysts; however, this is generally not associated with zeolite, so therefore is ignored.

Species adsorption can play an important role particularly under transient conditions, therefore gaining a thorough understanding of this particular area could lead to effective use of adsorbed ammonia as a NO_x reductant, optimising NO_x conversion, and minimising any slip [Nakayama et al, 2006]. However, it is currently unknown whether the amount of ammonia stored along the surface of the SCR is constant for the entire length of the SCR brick.

2.3.3 The use of Urea as an Additive

Although it is possible to inject ammonia directly into the exhaust, health and safety concerns do arise with this method, particularly as ammonia is a highly toxic substance. Instead, the injection of aqueous urea is preferred, which decomposes into ammonia once it enters the exhaust pipe, coming into contact with the hot exhaust gas.

$$(NH_2)_2CO + \text{heat} \rightarrow NH_3 + HCNO \quad (17)$$

$$HCNO + H_2O \rightarrow NH_3 + CO_2 \quad (18)$$

Reaction (17) is known as thermolysis, and takes place above 137°C (the sublimation point of urea). A heating filament may be used, but this may consume considerable amounts of energy if the filament is too big. [Kowatari et al, 2006] and [Nakayama et al, 2006]. Reaction (18) is the hydrolysis of HCNO, where the HCNO reacts with the water vapour in the exhaust, to accelerate this reaction at low temperatures a hydrolysis catalyst is often used upstream of the SCR. [Kowatari et al, 2006], and [Nakayama et al, 2006]. It is also observed in equation (18) that some CO_2 is produced, however, this is very small when compared with the amount produced from combustion inside the engine. The concentration of each of these varies according to exhaust gas temperature; this can be seen in Fig 2.9. As the temperature increases, the amount of urea decomposed into ammonia increases because of the accelerated sublimation and hydrolysis at higher temperatures.

Fig 2.9: Urea species decomposition with respect to temperature at the entrance of an SCR catalyst. Measurements were likely to have been made immediately after the urea injection point due to the incomplete decomposition at high temperatures. [Koebel et al ,2000]

Aqueous-urea is widely considered to be one of the most promising methods of storing and injecting ammonia into the vehicles exhaust system, however this is not without its problems.

The primary concern with the storing of aqueous urea is the potential freezing, particularly in regions where the climate favours colder conditions [Servati et al ,2005]; this can be solved with appropriate positioning of the urea storage tank in the vehicle, and the addition of extra insulation.

Other problems may relate to the distribution of urea inside the exhaust system, particularly under non-mixed flow. A common solution is to use mixing plates and axial vanes. [Kowatari et al, 2006] The disadvantages of this are urea to deposit on the plates, and an increase in exhaust back pressure. It is therefore expected that automotive companies may want to move away from this method. A more desirable alternative would be to perhaps use a 'dog-legged' exhaust pipe, and position the injector at the outer-edge radius. [Oesterle et al, 2008]

The complete decomposition of urea at low exhaust gas temperatures may also be problematic. One solution is to inject a small amount of urea through a small bypass, containing a heating filament and a hydrolysis catalyst; this has the potential assist in some of the decomposition of the urea, therefore

increasing the NO_x conversion at temperatures of around 150°C. [Kowatari et al, 2006], [Nishioka et al, 2006], and [Nishioka et al, 2008]. Other solutions include the application of extra insulation, or injecting the urea further upstream of the SCR. It may also be desired to restrict the gas flow through the exhaust under low-speed and idle conditions, however, this may lead to stalling on small vehicles such as cars and vans. [Saito et al 2003]

2.3.4 Diesel Oxidation Catalysts

One of the main concerns with the use of SCRs for light-duty diesel vehicles is the low exhaust gas temperatures, which can limit the conversion rates. One of the most important objectives is to obtain an NO: NO_2 ratio of 50:50 to satisfy conditions for the 'fast' SCR reaction, described in equation (9); this is particularly desirable for zeolites at low exhaust gas temperatures, which is particularly significant with zeolite-based catalysts. NO_2 is achieved by the oxidation of NO, as described in equation (19) below:

$$2NO + O_2 \leftrightarrow 2NO_2 \quad (19)$$

Equation (3) is satisfied with the addition of an oxidation catalyst, which also eliminates hydrocarbons and CO, also via oxidation.

$$2CO + O_2 \rightarrow 2CO_2 \quad (20)$$

$$HC + O_2 \rightarrow CO_2 + H_2O \quad (21)$$

The principal factors that can affect the performance of a DOC are the noble metal loading, the aged status of the catalyst, the exhaust gas temperature. Fig 2.10 describes the NO conversion efficiency of a typical DOC with respect to temperature for different exhaust gas mass flow rates:

Fig 2.10: NO conversion over a range of temperatures for different mass flow rates. From the left: m_{exh} = 400kgh^{-1}, and 700kgh^{-1} respectively. Conversion rates are likely to vary for different types of DOC. [Chatterjee et al, 2008]

It is observed in Fig 2.10 that peak performance occurs at temperatures around 350°C, and then decreases considerably. The NO_2: NO_x ratio finally begins to stabilise at around 550°C due to thermodynamic equilibrium occurring, where the forward chemical process is the same as its reverse. The effect at lower temperatures is likely due to catalyst activity being limited at temperatures below 300°C.

Fig 2.11: Overall NO_x consumption rates for different noble metal loadings and age status. [Chatterjee et al, 2008]

Fig 2.11 describes the effect that different noble metal loadings and age status have on the NO oxidation performance of the DOC. Once can see that a DOC with a higher noble metal loading and in a 'de-greened' status will give a higher reduction rates than one that is aged, has a lower noble metal loading, or both. The presence of particulates may also have an effect on the performance of the DOC.

One disadvantage with using a DOC is that it is very difficult for the NO_2: NO_x ratio to be controlled for all engine conditions [Forzatti et al, 2010], although allowing some of the exhaust gas to bypass the DOC could be considered a plausible solution to this problem. [Nakayama et al, 2006]

2.3.5 Commercial Applications for SCRs

Initially it was seen that the use of an SCR to reduce NO_x on small transportation (such as cars, mini buses, vans, and small trucks) was impractical due to the low exhaust gas temperatures, cost, administration of the aqueous-urea/ ammonia, and packaging considerations. [Koebel et al, 2000] and [Oesterle et al, 2008]. Methods to increase low-temperature activity such as the development of low-temperature zeolites , the introduction of aqueous NH_4NO_3 into the exhaust, and assisiting with the decomposition of urea into ammonia have been shown to be promising solutions. [Forzatti,et al 2010] and [Kowatari et al, 2006].

Currently SCRs are being used on heavy-duty vehicles, such as HGVs, and large buses/coaches because of their suitability for heavy-duty applications. NO_x reduction in these applications can reach up to 72% for a complete test cycle. V_2O_5 is the most common catalyst material in heavy duty applications due to its high selectivity across the temperature region in which heavy-duty vehicles primarily operate. Fig 2.12 and Fig 2.13 show two applications of SCRs:

Fig 2.12: Volvo FH scr truck. [Road Transport, 2008]

Fig 2.13: Volkswagen CC 2.0 TDI 'Blue-Motion'. [What Car?, N.D.]

Volkswagen are currently one of the pioneers in commercially applying SCRs to their production cars with their 'Blue-Motion' technology. [Volkswagen, N.D.] Ford have also undertaken research into the application of SCR technology onto passenger cars, where NO_x conversion rates of 92% were achieved. [Tennison et al, 2004]

It is also possible to use SCR in retrofit applications by using open-loop control in which NO_x reduction rates of 70% are possible. It would be anticipated that these reduction rates would be higher with a closed-loop control system, however, closed-loop control is difficult because of the difficulty in accessing the ECU. Another potential drawback of the retrofit application is that unless the vehicle has an onboard air supply, a separate compressor would be required as a urea transportation device. [Servati et al, 2005]

2.3.6 Summary

With SCRs becoming an ever more popular choice in the automotive industry as a method of NO_x reduction, it is important to design a system that gives optimum performance at a broad range of temperatures. One of the key areas is selecting the most appropriate catalyst material for the application concerned, as different catalysts deliver different levels of NO_x reduction at different temperatures.

Issues still surrounding SCRs however are the availability of an accurate 3D model that can predict spray and flow distribution that can be integrated into a CFD package. Access to a 3D simulation would lead to a more refined SCR system design that has a higher NO_x reduction rate; this is discussed in further detail in Section 2.5 of this thesis.

2.4 Catalyst Types

2.4.1 Overview

There are currently three main materials that SCR catalysts are made of, these are: platinum, vanadium, and zeolite. Whilst vanadium-based catalysts have been studied extensively, zeolites, in recent years have being considered more and more as a viable alternative, especially for light-duty applications, such as passenger cars, and small trucks. Tab 2.1 displays the types of materials used on SCRs and their temperature ranges, due to commercial sensitivity, manufacturers do not disclose the exact composition of their zeolite-based catalysts:

Tab 2.1: Catalyst operating temperatures [Tamaldin, 2010].

Vanadium-based catalysts have been studied extensively for heavy-duty applications, however, in recent years, zeolites have being considered more and more as a suitable option for light-duty vehicles.

2.4.2 Zeolite Based Catalysts

Zeolite catalysts are generally renowned for their good conversion efficiencies at high temperatures, however, they have recently become a popular choice for applications that involve low exhaust gas temperatures. Zeolite-based catalysts can be split into two categories: high temperature and low temperature.

High temperature zeolites are mainly constructed from mordernite; these usually have a structure containing SiO_2 and Al_2O_3, and have a ratio of 10:1 [Chen et al, 1995]. Out of the four catalyst materials described in Tab 2.1, zeolites can operate at higher temperatures than both V_2O_5 and Pt; this is because, unlike Pt and V_2O_5, zeolites do not oxidise, unlike Pt and V_2O_5.

Low temperature zeolites were developed for mobile engine applications, such as cars, small trucks, and buses. [Girard et al, 2008] These new zeolites are generally either copper-based (Cu) or iron based (Fe), and are active between 200 - 400°C. [Tamaldin, 2010]

The main disadvantages of zeolites are that at temperatures exceeding 600°C, and in high water concentrations, deactivation may occur, and in the worse case scenario, complete collapse of the crystalline structure [Tamaldin, 2010], however, such temperatures are highly unlikely in light-duty

applications. Difficulties may also arise on the long-term durability of the catalyst, specifically in the presence of engine oil and un-burnt fuel. Formation of sulphates or phosphorous on the catalyst washcoat could reduce the NO_x conversion efficiency by up to 30% for quantities as low as $0.6gl^{-1}$. [Shibata et al, 2007] A low-sulphur fuel would therefore be recommended to maintain the durability of the catalyst, as well as to reduce unwanted SO_2 emissions.

Fig 2.14: Ammonia outlet concentration for Cu-zeolite and Fe-zeolite catalysts. [Colombo et al, 2010]

It can be seen in Fig 2.14 that the Cu-zeolite catalyst is able to store noticeably higher amounts of strongly bonded ammonia when compared with the Fe-zeolite catalyst. Complete ammonia desorption of the ammonia from the surface of the Fe-zeolite catalyst is also noticed to occur at about 500°C, whilst complete ammonia desorption from the Cu-zeolite catalyst is not observed until 550°C. Desorption does not begin to occur until the gas temperature reaches about 450°C.

Fig 2.15 and Fig 2.16 plot the conversion dependency on the inlet NO_2: NO_x ratio and exhaust gas temperature for Cu-zeolite and Fe-zeolite SCR catalysts respectively:

Fig 2.15: NO_2: NO_x and temperature dependency on NO_x conversion for Cu-based zeolites. [Colombo et al, 2010]

Fig 2.16: NO_2: NO_x and temperature dependency on NO_x conversion for Fe-based zeolites. [Colombo et al, 2010]

It is observed from Figs 2.15 and 2.16 that the Fe-based zeolite offers a superior NO_x conversion efficiency at lower temperatures, when compared with the Cu-based zeolite. The dependency on the inlet NO_2: NO_x ratio, however, is noticeably greater with the Fe-zeolites up to about 500°C. One also notices that at temperatures > 350°C, the conversion efficiency of the Cu-zeolite SCR begins to decline, this is not observed with the Fe-based zeolite catalyst and could be attributed to a higher thermal durablilty associated with Fe-zeolites. [Narayanaswamy et al, 2008]

Fig 2.17 and Fig 2.18 plot the spatial conversion profiles for Cu-based zeolite SCRs, whilst Fig 2.19 and Fig 2.20 plot the spatial conversion profiles for Fe-based zeolites:

Fig 2.17: Spatial conversion profiles for a Cu-based zeolite when NO: NO_x = 1.0 at 250°C. Hou et al, 2011]

Fig 2.18: Spatial conversion profiles for a Cu-based zeolite when NO_2: NO_x = 0.5 at 250°C. [Hou et al, 2011]

The channel numbers are the radial measurement distances from the washcoat, channel 1 is furthest from the washcoat whilst channel 6 is closest. [Hou et al, 2011] The catalyst was aged for about 72 hours at 500°C. [Hou et al, 2011]

Fig 2.19: Spatial conversion profiles for an Fe-based zeolite at different temperatures when NO: NO_x = 1.0. [Luo et al, 2010]

Fig 2.20: Spatial conversion profiles for an Fe-based zeolite at different temperatures when NO_2: NO_x = 0.5. [Luo et al, 2010]

When Figs 2.17 – 2.18 are compared with Figs 2.19 – 2.20, it is observed that at 250°C, for both cases, the Cu-based zeolite catalyst compares favourably with the Fe-based zeolite, particularly when one takes into consideration the fact that the Cu-zeolite SCR was aged, whilst the Fe-zeolite wasn't. This contradicts findings from earlier in this section, and could suggest a difference in the catalyst formulations. It can also be seen that for both cases, most of the NO_x conversion takes place in the first half of the catalyst. More investigation into this area, particularly at the entrance of the catalyst, where the space velocities are very high, would be required. This method could assist in optimising the size of the catalyst, which could lead to a reduction in manufacturing costs, and packaging.

One of the main disadvantages with Fe-based zeolites, is the effect of ammonia inhibition of SCR reactions at low exhaust gas temperatures, such an effect is not as noticeable with Cu-zeolites. [Colombo et al, 2010] This inhibition effect could mean a less aggressive dosing strategy for Fe-zeolite SCRs than for their Cu-based counterparts, and also more control over the injection of the additives. The sensitivity to the upstream NO_2: NO_x ratio would also require a more complicated control system, which could mean an increase in costs, and also have an impact on the levels of other emissions. The use of Cu-based zeolites could therefore provide a more cost effective solution than their Fe-based counterparts.

Reactivity with zeolites can further be improved by using mesoporous catalysts that have a greater number of acid sites. Fig.2.21 describes the differences in catalyst performance for conventional and mesoporous Fe-based zeolites [Kustov et al, 2007]:

Fig 2.21: Comparison between conventional (c) and mesoporous zeolites (m). [Kustov et al, 2007]

Recent work undertaken at the University of Waterloo investigates the spatial conversion profiles of Fe-based zeolites and Cu-based zeolites. [Luo et al, 2010], and [Hou et al, 2011]. The work on Cu-zeolite catalysts investigates the effect of hydrothermal aging on the NO_x conversion efficiency, which decreased the reactivity of SCR reactions, ammonia oxidation, and NO_2 decompostion at high

temperatures. [Hou et al, 2011] The effect of hyrdrothermal aging on NO oxidation, however, was shown to be minimal. [Hou et al, 2011]

2.4.3 Vanadium Based Catalysts

V_2O_5 with TiO_2 is the most common SCR catalyst material, its operating range is in-between Pt and high-temperature zeolites. Unlike zeolites, V_2O_5 is capable of storing O_2 on the catalyst washcoat. Modern V-based catalysts are wash-coated onto cordierite monoliths; these produce better conversion rates at higher space velocities. [Girard et al, 2008] Their temperature range is smaller than zeolites, but bigger than Pt.

The main components are V_2O_5, TiO_2, and WO_3. V_2O_5 is generally considered to be responsible for the conversion of NO_x via ammonia. TiO_2 is the high surface area carrier, and the presence of WO_3 increases durability, and the acidity, which increases NO_x conversion rates. [Tamaldin, 2010]

V_2O_5 has the advantage that it is relatively immune to sulphur and hydrocarbon poisoning, although its thermal durability is less than its zeolite counterparts. The "light-off" temperatures are also less than zeolites. With newer V_2O_5 catalysts, it is possible to reduce the catalyst volume without compromising selectivity. [Girard et al, 2008]

Some of the major environmental concerns about using V-based catalysts are the potential toxicity of vanadium (in 2005 vanadium pentoxide was listed as a cancer causing chemical [Tamaldin, 2020]), and its low conversion efficiency at higher temperatures due to competitive ammonia oxidation. [Kustov et al, 2007] The most undesired effect, however, is the oxidation of sulphur to form SO_2 that can then react with water in the atmosphere to form H_2SO_4, which is known to be a cause of acid rain. Low-sulphur fuels would still be a necessity in the reduction of automotive emissions.

2.4.4 Platinum Based Catalysts

Platinum catalysts operate at lower temperatures than V_2O_5 and zeolite (175 - 250°C). Maximum conversion, however, does not occur over a large span like the other two catalysts discussed in this section. Consequently, Pt is not a common choice for the majority of applications that may wish to use an SCR.

Pt is more commonly used in oxidation catalysts as it is un-reactive to poisons such as calcium, zinc, and sulphur that are common additives in diesel fuel, although it is poisoned by phosphorous. [Tamaldin, 2010] One of the disadvantages of using Pt is the tendency to convert excessive amounts of NO to NO_2 if used in an oxidation catalyst. In some cases palladium is also used alongside platinum to increase the HC conversion efficiency. [Mannula et al, 22007]

2.4.5 Other Types of SCR

Although V_2O_5 is one of the most common catalyst materials, and is highly suited to heavy-duty applications the presence of V_2O_5 does present hazards. An alternative to V_2O_5 is to use V-free catalysts, based primarily on TiO_2, which also act as an ammonia oxidation component. Several advantages are offered over conventional V-based SCRs, such as reduced catalyst volume (which can lead to an increase in space velocities), the elimination of a post-SCR oxidation catalyst, and also a reduced risk to human health. [Hamada et al, 2005] and [Tamaldin, 2010]. The difference in the volume between a standard commercial SCR catalyst and V-free SCR is presented in Fig 2.22:

Fig 2.22: Schematic demonstrating the differences in catalyst volume. [Hamada et al, 2005]

Fig 2.23: NO_x and excess ammonia reduction rates for V_2O_5 catalyst (blue) and TiO_2-based SCR (red). [Hamada et al, 2005]

It can be seen that in Fig 2.23 that TiO_2 based catalysts offer similar NO_x reduction rates when compared with conventional V-based catalysts, but the ammonia slippage is noticeably less when the exhaust gas temperature exceeds 250°C.

Aluminium oxide (Al_2O_3) is also known to be used in SCR systems, although instead of aqueous-urea being used, methanol is required. This can give overall NO_x reduction rates of up to 70% [Tabata et al, 1994], but the potential drawbacks of using methanol include are its high flammability, and its toxicity to humans. Al_2O_3 is also better suited to heavy-duty applications, where gas temperatures are known to reach its peak performance (400°C).

2.5 SCR System Modelling

2.5.1 Overview

Due to the ever increasing commercial use of 'Selective Catalytic Reduction' for various types of diesel application, more knowledge into their performance characteristics is inevitably required. Currently there are two methods of investigation: laboratory (engine and micro-reactor), and computer-based. Although laboratory-based work is representative of the real world, it can be expensive, time consuming, and also lead to potentially considerably quantities of harmful gases emitted into the atmosphere.

Modelling SCR systems is widely acknowledged to be "fruitful" [Tronconi, 1997] as it has the advantage of reducing the use of test cells and labs; this can help reduce costs, save time, and be potentially less harmful to the environment. Such a device is also favourable due to the number of different parameters and input conditions involved. [Chatterjee et al, 2005]

The main processes involved in SCR simulation are: fluid flow, heat transfer, mass transfer, spray behaviour, and chemical kinetics. There are currently numerous kinetic schemes available, each scheme includes different influencing factors that will be discussed throughout this chapter. The schemes currently adopted by Coventry University are the schemes by Chalmers University and General Motors [Olsson et al, 2008], and IMCC and AVL [Wurzenburger et al, 2005], although other kinetic schemes have also been assessed. The main purpose of this chapter is to evaluate different kinetic schemes available to validate an SCR model.

2.5.2 Vanadium Based Catalysts

Considerable research has already been undertaken to model the behaviour of V_2O_5 catalysts, the vast majority of these models have been analysed in a one-dimensional format; this assumes uniformity across the entire catalyst cross-section.

Early work on V_2O_5-based catalysts had predominantly focused on SCR catalysts for stationary applications, such as power stations, where the operating conditions were steady-state. [Tronconi, 1997] However, now that SCR systems have been implemented for mobile applications, more complex models have subsequently superseded earlier models, these take into account different types of SCR reaction.

Due to the increasing use of SCR technology for transport applications, where conditions are transient, the 'standard' SCR reaction alone is not considered to be adequate enough to fully describe SCR behaviour, nor is it the most desirable under these conditions. Reactions described in Section 2.3.1 are also included, whilst other reactions such as, CO_2, and N_2 could be considered, these have no direct influence on the SCR process, they can be excluded from any future models that are SCR-specific. [Chi et al, 2005] and [York et al, 2004].

Further work began to investigate transient conditions; this led to the development of a '1D + 1D' simulation for V-based SCRs under transient conditions. [Ciardelli et al, 2004] A '1D + 1D' model also exists for zeolites; which is discussed in Section 2.5.3. One of the major limitations of this V_2O_5-based model is that the ammonia adsorption capacity for the catalyst was a low temperature estimate, which is likely to change for increasing temperature.

2.5.3 Zeolite Based Catalysts

Until recently most of the mathematical models have focused on V_2O_5 catalysts, however, with the emergence of zeolite as an alternative catalyst material, particularly for light-duty applications, mathematical models for zeolites have been developed. Since the work currently been embarked on at Coventry University is solely based on zeolites, zeolite kinetic studies will be the main focal point of this report chapter. [Benjamin et al, 2007]

When describing SCR behaviour it is often best to reduce the number chemical activities to only a few, as to not complicate the model. The following reaction scheme is for the 'standard' SCR reaction on zeolite catalysts, which focuses on the oxidation of NO to NO_2 as the rate determining step [Kustov et al, 2007]; this shows a strong agreement with all schemes described in this section.

$$2NH_3 + 2H^+ \rightarrow 2NH_4^+ \quad \text{(Fast Reaction)}$$

$$NO + 1/2O_2 \rightarrow NO_2 \quad \text{(Slow Reaction)}$$

$$NO_2(NH_4^+)_2 + NO \rightarrow 2N_2 + 3H_2O + 2H^+ \quad \text{(Standard Reaction)} \qquad (22)$$

The reactions described in equation (22) are ammonia adsorption, NO oxidation, and the the 'standard' SCR reaction.

2.5.3.1 Daimler-Chrysler Scheme

The first reaction model was developed by Daimler-Chrysler and Milan Polytechnic. Equation (23) described above is particularly effective for Fe-zeolites, where NO oxidation takes place on Fe^{3+} sites. [Kustov et al, 2007] The kinetic shceme below describes the 'standard' SCR reaction, where not only ammonia travelling into the catalyst is accounted for, but also the ammonia inhibition; the oxygen concentration is also accounted for [Chatterjee et al, 2007]:

$$r_{NO} = k_{NO} \times \exp\left[\frac{E_{NO}}{R}\left[\frac{1}{T} - \frac{1}{473}\right]\right] \times \frac{C_{NO}\theta_{NH3}}{1 + K_{LH} \times \left[\frac{\theta_{NH3}}{1-\theta_{NH3}}\right]} \times \left[\frac{P_{O2}}{0.02}\right]^{\beta} \ldots \quad (23)$$

As described in equation (14) the oxidation of NO is also significant when describing the 'standard' SCR reaction [Chatterjee et al, 2007]:

$$r_{NOox} = k_{NOox} \times \exp\left[\frac{E_{NOox}}{RT}\right]\left[C_{NO}\sqrt{P_{O2}} - \frac{C_{NO2}}{Keq}\right] \ldots\ldots\ldots\ldots\ldots\ldots\ldots \quad (24)$$

The 'fast' SCR reaction described earlier uses a different mechanism, with NH_4NO_3 as an intermediate step, for simplicity this step is ignored in the kinetic scheme explained in equation (25), [Chatterjee et al, 2007]:

$$r_{Fast} = k_{Fast} \times \exp\left[\frac{E_{Fast}}{R}\left[\frac{1}{T} - \frac{1}{473}\right]\right] \times \frac{C_{NO2}}{\varepsilon + C_{NO2}} \times C_{NO}\theta_{NH3} \ldots\ldots\ldots\ldots \quad (25)$$

One must also take into consideration the potential differences between 'fast' SCR reactions over V_2O_5 and zeolite, with particular attention being paid to the fact that V_2O_5 oxidises much more readily than zeolite. The kinetic scheme in equation (25) does not feature oxygen concentration due to the 'fast' SCR reaction being completely independent of oxygen (O_2).

A major factor in determining the rate of reaction of NO_x and ammonia is the amount of ammonia adsorbed/desorbed onto and from the catalyst surface. Also if the ammonia feed is suddenly stopped, the conversion process will still continue due to ammonia being chemically desorbed from the catalyst surface. This is true for both V_2O_5 and zeolite. Equations (26) – (28) describe ammonia adsorption, ammonia desorption, and competitive ammonia oxidation respectively [Chatterjee et al, 2007]:

$$r_{ads} = k_{ads} \times C_{NH3}\left[-\theta_{NH3}\right] \ldots\ldots\ldots\ldots\ldots\ldots\ldots\ldots\ldots\ldots\ldots\ldots\ldots\ldots\ldots\ldots\ldots\ldots \quad (26)$$

$$r_{des} = k_{des} \times \exp\left[-\frac{E_{des}}{RT}\left[-\gamma\theta_{NH3}\right]\right]\theta_{NH3} \ldots\ldots\ldots\ldots\ldots\ldots\ldots\ldots\ldots\ldots\ldots\ldots\ldots\ldots\ldots\ldots\ldots\ldots \quad (27)$$

$$r_{OX} = k_{OX} \times \exp\left[-\frac{E_{OX}}{RT}\right]\theta_{NH3} \ldots\ldots\ldots\ldots\ldots\ldots\ldots\ldots\ldots\ldots\ldots\ldots\ldots\ldots\ldots\ldots\ldots\ldots\ldots\ldots\ldots\ldots \quad (28)$$

Competitive ammonia oxidation, described in equation (28), is also present in the model, for light-duty applications that involve lower exhaust gas temperatures, however, this is not expected to have a noticeable impact for the model concerned, where gas temperatures will not even reach 400°C. One

may also notice the absence of a temperature term in equation (26), however this is present in the pre-exponential term (k_i) described in equation (37).

The main differences between this reaction scheme and the other schemes discussed in this section are the presence of an inhibition factor concerning ammonia, and O_2. Both of these might be considered to be very small however, so doubts may arise as to the relative merits of their inclusion. [Olsson et al, 2008] Varying the quantities of O_2 in the exhaust pipe of an engine test bed under a fixed load would also be very difficult to do without chaning the NO_2: NO_x ratio.

The results shown in Fig 2.24 display a strong correlation between mathematical and experimental data for transient test runs using a zeolite based catalyst. The model was also observed to work particularly well for V-based catalysts. [Chatterjee et al, 2007]

Fig 2.24: Mathematical and experimental correlation for different NO_2: NO_x ratios over ETC test cycle. [Chatterjee et al, 2007]

Previous investigations by Coventry University have shown that the agreement between this model and the experimental data undertaken on an engine test bed was quite poor. [Tamaldin et al, 2010]

2.5.3.2 IMCC and AVL Scheme

The scheme described previously can be considered to be fairly simple, due to the number of rate expressions used. An alternative scheme, devised by the IMCC and AVL is described below, which also investigates the slow SCR reaction involving NO_2 and ammonia [Wurzenberger et al, 2005]:

$$r_{NO} = 3200 \times \exp\left[\frac{-7500}{T_s}\right] \times C_{NO} \times \frac{1 \times 10^{-14} \times \exp\left[\frac{34850}{T_s}\right]}{1 + 1 \times 10^{-14} \times \exp\left[\frac{34850}{T_s}\right]} \times C_{NH3} \qquad (29)$$

Equation (28) describes the 'standard' SCR reaction under steady-state conditions, this assumes that the ammonia adsorption/desorption rate is under equilibrium; this expression is insufficient to describe the kinetics of an SCR catalyst under transient conditions due to the varying amounts of ammonia

adsorbed and desorbed. Therefore an alternative transient scheme, described in equation (30), is required that factors this into account [Wurzenberger et al, 2005]:

$$r_{NO} = 1\times10^{6}\times\exp\left[\frac{-9552}{T_s}\right]\times C_{NO}Z^{*}_{NH3}(S)\times\left[1-\exp\left[\frac{Z_{NH3}(S)}{Z^{*}_{NH3}(S)}\right]\right]\ldots. \quad (30)$$

The number of sites containing ammonia (Z_{NH3}) is expressed as a fraction of the total number of ammonia storage sites on the catalyst as the formulation varies from catalyst to catalyst, the other schemes discussed in this chapter denote this term as θ_{NH3}. The NO reaction rate with ammonia for surface fractions of $Z^{*}_{NH3}(S) \geq 0.06$ can be considered to be independent of stored ammonia, because of the continuing rise of ammonia, even when the NO concentrations have reached a steady-state value, shown in Fig 2.25. [Lietti et al, 1998] and [Wurzenberger et al, 2005]. One may also observe that equations (29) and (30) do not include the effect of oxygen concentration on the SCR reactions that is included in equation (23). [Chatterjee et al, 2007]

Fig 2.25: Transient species concentrations for a step input of ammonia with respect to time (seconds). [Lietti et al, 1998]

The main difference with the 'standard' reaction model proposed by Wurzenbeger et al, and Chatterjee et al is the exclusion of the NO oxidation expression, however, since NO is shown to oxidise on Fe and Cu-based zeolites, an inclusion may well be desired. [Kustov et al, 2007] and [Olsson et al, 2008].

Equation (31) below describes the 'fast' SCR reaction [Wurzenberger et al, 2005], like the model devised by Daimler-Chrysler [Chatterjee et al, 2007], the fast SCR reaction has been simplified to exclude any intermediate reactions:

$$r_{FAST} = 5\times10^{12}\times\exp\left[\frac{-9700}{T_s}\right]\times C_{NO}C_{NO2}\times\frac{3\times10^{-16}\times\exp\left[\frac{35420}{T_s}\right]}{1+3\times10^{-16}\times\exp\left[\frac{35420}{T_s}\right]}C_{NH3} \quad (31)$$

Equation (32) describes the 'slow' SCR reaction, which was excluded from the Daimler-Chrysler scheme [Wurzenberger et al, 2005]:

$$r_{NO2} = 3000 \times \exp\left[\frac{-8800}{T_s}\right] \times C_{NO2} \times \frac{1\times10^{-14}\left[\frac{32000}{T_s}\right]}{1+1\times10^{-14}\left[\frac{32000}{T_s}\right]} C_{NH3} \ldots\ldots\ldots \qquad (32)$$

The inclusion of the kinetic expression given above depends on the SCR system, as, in some cases it has been discovered that an NO: NO_2 ratio of approximately 30:70 is shown to give optimum conversion rates for some SCRs.

Ammonia adsorption and desorption, as well as ammonia oxidation are also described in this model:

Steady-state oxidation [Wurzenberger et al, 2005]:

$$r_{NH3ox} = 1000 \times \left[\frac{-10320}{T_s}\right] \times C_{NH3} \ldots\ldots\ldots\ldots\ldots\ldots\ldots\ldots\ldots\ldots\ldots\ldots\ldots\ldots\ldots.. \qquad (33)$$

Transient oxidation [Wurzenberger et al, 2005]:

$$r_{NH3ox} = 7\times10^{3} \times \exp\left[\frac{-16400}{T_s}\right] \times Z_{NH3(S)} \ldots\ldots\ldots\ldots\ldots\ldots\ldots\ldots\ldots\ldots\ldots\ldots \qquad (34)$$

Ammonia adsorption and desorption respectively [Wurzenberger et al, 2005]:

$$r_{ads} = 4\times10^{9} \times \exp\left[\frac{-10100}{T_s}\right] \times C_{NH3} \times \left[- Z_{NH3}(S)\right] \ldots\ldots\ldots\ldots\ldots\ldots\ldots\ldots \qquad (35)$$

$$r_{des} = 8\times10^{4} \times \exp\left[\frac{-10482\left[-0.256 Z_{NH3}(S)\right]}{T_s}\right] \times Z_{NH3}(S) \ldots\ldots\ldots\ldots..(36)$$

Equation (37) describes the reaction rate constant calculation used in the schemes discussed in this section:

$$k_i = \exp\left[\frac{E_i(T)}{RT}\right] \ldots\ldots\ldots\ldots\ldots\ldots\ldots\ldots\ldots\ldots\ldots\ldots\ldots\ldots\ldots\ldots\ldots\ldots\ldots\ldots\ldots\ldots. \qquad (37)$$

2.5.3.3 Chalmers University Scheme

The scheme by Chalmers University focuses on transient runs with particular emphasis being placed on the role of adsorbed ammonia on the catalyst bed. Equations (38), (39), and (40) describe ammonia adsorption, ammonia oxidation and NO oxidation respectively [Olsson et al, 2008]:

$$r_{ads} = k_{1,f} C_{NH3} \theta_{S1-vacant} - k_{1,b} \theta_{NH3-S1} \ldots\ldots\ldots\ldots\ldots\ldots\ldots\ldots\ldots\ldots\ldots\ldots\ldots.. \qquad (38)$$

$$r_{NH3ox} = k_2 C_{O2} \theta_{NH3-S1} \ldots\ldots\ldots\ldots\ldots\ldots\ldots\ldots\ldots\ldots\ldots\ldots\ldots\ldots\ldots\ldots\ldots\ldots\ldots\ldots \qquad (39)$$

$$r_{NOox} = k_{3,f} C_{O2}^{1/2} C_{NO} - k_{3,b} C_{NO2} \quad (40)$$

The reaction described in expression (40) is reversible, which is denoted by the second term. [Olsson et al, 2008] Equations (42), (44), and (46) describe the 'standard,' 'fast,' and 'slow' SCR reactions respectively. The scheme focuses on adsorbed ammonia only, and for simplicity, only one adsorption site, denoted by S1, is used [Olsson et al, 2008]:

$$4NH_3\text{–}S1 + 4NO + O_2 \rightarrow 4N_2 + 6H_2O + 4S1 \quad (41)$$

$$r_{NO} = k_4 C_{NO} \theta_{NH3-S1} \quad (42)$$

$$2NH_3\text{–}S1 + NO + NO_2 \rightarrow 2N_2 + 3H_2O + 2S1 \quad (43)$$

$$r_{FAST} = k_5 C_{NO} C_{NO2} \theta_{NH3-S1} \quad (44)$$

$$8NH_3\text{–}S1 + 6NO_2 \rightarrow 7N_2 + 12H_2O + 4S1 \quad (45)$$

$$r_{NO2} = k_6 C_{NO2} \theta_{NH3-S1} \quad (46)$$

One of the major problems with SCRs can be slippage of N_2O into the atmosphere; this is caused by a version of the 'slow' SCR reaction, where instead of N_2O, as well as nitrogen is produced [Olsson et al, 2008]:

$$2NH_3 + 2NO_2 \rightarrow N_2 + N_2O + 3H_2O \quad (47)$$

Chalmers University [Olsson et al, 2008]:

$$2NH_3\text{–}S1 + 2NO_2 \rightarrow N_2 + N_2O + 3H_2O + 2S1 \quad (48)$$

In some of the models this reaction is neglected [Chatterjee et al, 2007], however, in situations where excess NO_2 is produced prior to entering the SCR it is important to at least consider the importance of this reaction, ultimately, it is the quantity of N_2O created that determines whether this reaction is included or not.

$$r_{N2O} = k_7 C_{NO2} \theta_{NH3-S1} \quad (49)$$

The rate constants (k_i) features a pre-exponential factor, which varies depending on catalyst age, formulation and temperature.

It can be stated that although all of the schemes discussed can present accurate predictions of SCR behaviour, the main limitation of using these schemes in a 1D format is that a 1D model is unable to model non-uniform flow distribution inside the catalyst. Models can be equipped, however, to represent individual channels, where flow can be assumed to be uniform inside each channel, and the fluid flow modelled in three dimensions upstream of the catalyst. Although potentially more accurate, the drawback of this method would be increased computational time.

Fig 2.26 shows the main transport effects on an exhaust pipe: heat transfer, mass transfer, and momentum transfer. Heat transfer occurs via conduction and convection in the gas phases, and by conduction in the solid phases. Momentum transfer and mass transfer are only considered in the exhaust gas when modelling the pipe, however, mass transfer between the solid and gas phases must be considered when modelling the catalyst, as chemical reactions occur on the catalyst washcoat.

Fig 2.26: Main transport effects in an exhaust pipe with multiple layers of insulation. [Wurzenburger et al, 2005]

It is only necessary to consider a non-uniform gas temperature distribution in the axial direction if only a small cross-sectional portion of the exhaust is modelled, and assuming the model is 1D and adiabatic. [Chi et al, 2005]

2.5.4 The 'Porous Medium' Approach

The 'porous medium' approach is a technique to model the thermodynamic, fluid, and chemistry behaviour of exhaust gases in an SCR catalyst in 3D. The technique works by applying a porosity value to the catalyst section of the model; this restricts the available area that the fluid can travel through. The lower the porosity value, the less space the fluid has to travel through. Previous work has already been undertaken by Coventry University into fluid dynamics and heat transfer inside the catalyst. [Day, 2001] The 'porous medium' approcach has already proven successful for conventional three-way catalysts and LNTs as it is able to conveniently model the chemistry, fluid dynamics, and heat transfer. [Benjamin et al, 2007] A three-dimensional model of an SCR catalyst using the porous medium method is displayed in Fig 2.27:

Fig 2.27: "Porous Medium" CFD model showing the SCR catalyst (light blue). The dark blue section is the solid material; this models the catalyst wall and the washcoat. The model shown is based on an actual test exhaust, containing an inlet pipe (red and green cells), a long-diffuser (yellow), and an outlet (purple) to complete the model. [Benjamin et al, 2007]

Previous work at Coventry University has focused on the development of the 'porous medium' by validating different reaction models against steady-state engine test data on a 1D format. [Tamaldin et al, 2010] The exhaust is equipped with an expansion box to allow a mixing of the urea-spray, and a narrow-angled diffuser to ensure that no flow separation occurs before the gas enters the SCR. The urea is injected into the exhaust stream from the top of the expansion box, although other injection positions could also be considered. The 'porous medium' approach is explained in greater detail in Chapter 5 of this thesis.

Despite the recent interest in low-temperature zeolites, there are still some unknowns, such as catalyst 'light-off,' transient behaviour, which can have an impact on the exhaust gas temperature that is crucial for SCR reactions, and the spatial species conversion profiles.

2.6 Concluding Remarks

After undertaking a literature review into the mechanism of SCR systems and their applications, the following observations were made:

- Selective Catalytic Reduction (SCR) of NO_x via aqueous-urea is a promising technique for reducing NO_x emissions from light-duty diesel engines due to its low costs, low health and safety risk, good conversion rates, minimal impact on fuel economy and exhaust back pressure, and ease of control when compared NO_x traps.

- High NO_x reduction witnessed in light-duty diesel vehicles have been made possible because of the development of low-temperature zeolite catalysts.

- The inlet ratio of NO_2: NO_x is critical for obtaining the optimum reaction rates, at exhaust gas temperatures of around 200°C; an NO_2: NO_x ratio of about 0.5 is desired.

- Although Fe-based zeolites have a higher activity than their Cu-based counterparts at lower temperatures, they are more sensitive to NO_2: NO_x ratio and are also vulnerable to ammonia inhibition at low exhaust gas temperatures. A more complicated control strategy, could therefore be needed for Fe-based SCRs.

- Ammonia-slip at low temperatures is a major concern with SCR systems with either some form of closed-loop control is needed or an oxidation catalyst can be placed downstream of the SCR required.

- The investigation of the spatial conversion profiles of an experimental SCR can provide a greater insight into the influence of each SCR reaction along the catalyst, and also assist in the size optimisation of the SCR catalyst brick, which could help reduce packaging on the vehicle, as well as manufacturing costs.
- Mathematical models are a useful tool in predicting SCR performance under different engine and exhaust conditions, and can also help reduce development costs and time. One of these modelling techniques is the 'porous medium' approach, which will be applied in the CFD studies presented later in this thesis.

2.7 Current Gaps in Knowledge

The following gaps in knowledge were identified:

- The understanding of SCR behaviour for a Cu-based zeolite along a full-sized SCR catalyst, particularly just after the inlet, where the space velocities are very high; this could help reduce packaging requirements, manufacturing costs, and also provide a more rigorous method of assessing the ability of a mathematical model to successfully predict the experimental data.

- The amount of ammonia adsorbed along the length of the catalyst also provides a further insight into the performance of the mathematical model, and could also assist in devising an appropriate ammonia dosing strategy.

- The transient NO_x and ammonia concentration profiles, particularly just downstream of the entrance of the SCR, for different NH_3: NO_x injection ratios, and inlet NO_2: NO_x ratios.

- The validation of a 1D mathematical model using the 'porous medium approach' in CFD using kinetics obtained from open literature against experimental data obtained from an engine test exhaust system.

Chapter 3: Project Outline

3.1 Project Objectives

The overall aim of this research project is to study the behaviour of Cu-zeolite based SCR catalytic converters under steady-state and transient conditions at low exhaust gas temperatures in order to provide a unique data set for CFD nodel validation. The key objectives of this project are:

- To commission a diesel engine test cell.
- Undertake steady-state and transient experiments on an SCR exhaust system using ammonia gas.
- To correlate experimental data with a 1D SCR model with CFD using the 'porous medium' approach.

3.2 Steady-State Testing

The anticipated outcome to be achieved from the steady-state experiments is a greater understanding of the low-temperature SCR performance along the catalyst brick, with an emphasis on the conversion rates just after the inlet, where the space velocities are very high. Previous work by Coventry University has shown that, when urea-spray is used, not all of it decomposes downstream of the SCR, therefore ammonia gas in balance-nitrogen will be used.

Steady-state data will also act as a suitable form of initial validation of reaction schemes to be utilised in this project.

3.3 Transient Testing

The expected outcomes from the transient experiments will be a greater understanding of catalyst response time under 'warm-start' conditions for high space velocities at low exhaust gas temperatures and different inlet NO_2: NO_x ratios, the ammonia storage capacity for different inlet levels of ammonia will also be investigated. The transient data will also be used to validate the CFD model.

3.4 CFD Analysis

The objective is to simulate experimental observations in CFD using the 'porous medium' approach described in Section 2.5.4. The main outcome of this will be to help validate a 1D SCR model using kinetics described in open literature. It is anticipated that this technique will allow for a more thourough analysis into whether the model can accurately predict what is happening along the SCR catalyst brick and the transient response time. The model will also the identification of any differences between the two different types of Cu-zeolite catalysts.

Chapter 4: Engine Testing

This chapter presents details of the engine test cell, the engine and exhaust rig. The setup and calibration the ammonia gas injection devices, analyser specification, and the experimental test procedures are presented.

4.1 Engine Test Cell

A schematic of the engine test cell is displayed in Fig 4.1. The engine is connected to a Froude-Consine 150AC dynamometer that acts as a starter motor and as an absorber. Exhaust emissions were sampled using a Horiba EXSA 1500, a Horiba MEXA-1170 Nx, and ETAS-Meters. Analysers and the dynamometer were controlled using a Froude Texcel v12 control unit, whilst ECU data was obtained using GREDI.

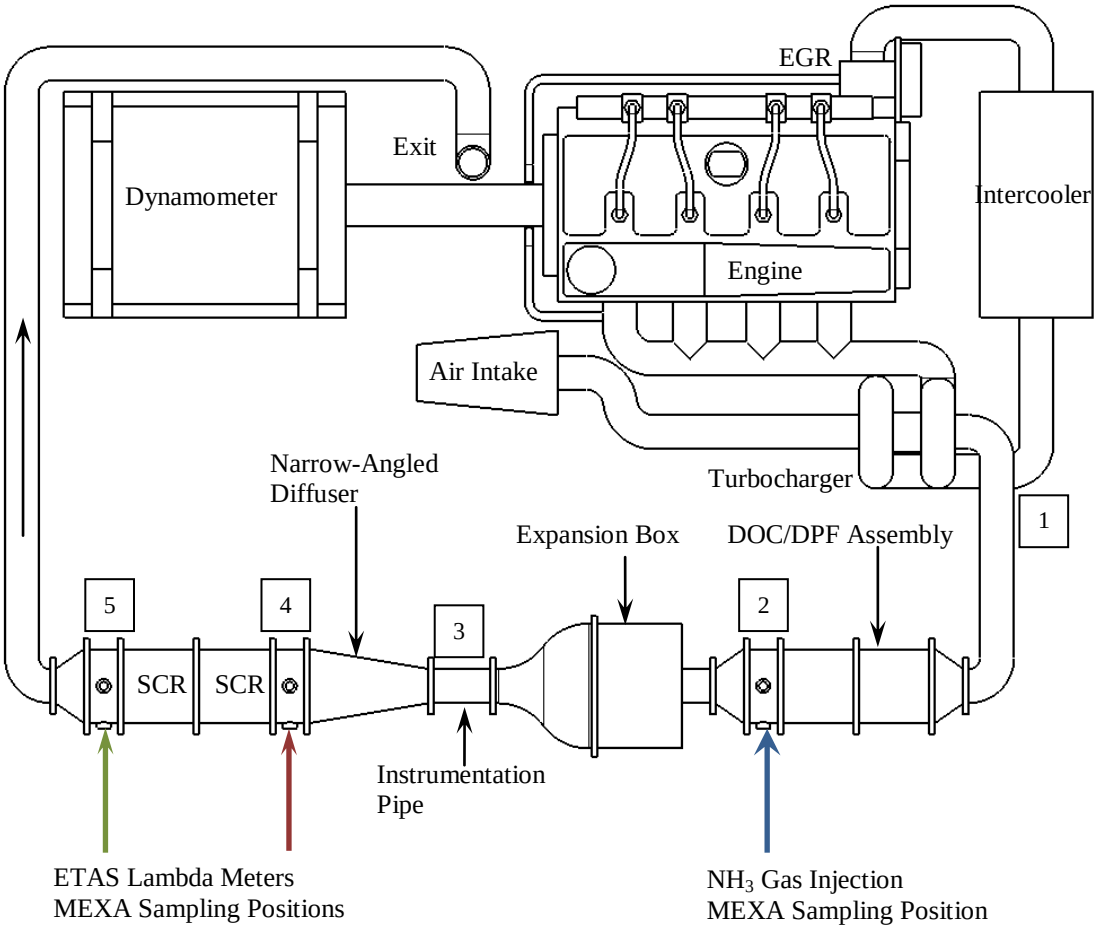

Fig 4.1: Test cell schematic. Temperatures were measured at points 1 – 5 using K-type thermocouples, whilst the exhaust back-pressure was measured at the exit of the exhaust.

The exhaust rig was manufactured by Coventry University, the catalysts were supplied by Johnson Matthey, and canned by Faurecia. The main purpose of the expansion box and the long diffuser was to provide a uniform flow distribution along the pipe and the SCR bicks respectively, which is necessary for the parametric studies undertaken in this thesis.

4.2 The Engine

The engine used in the experiments is a 2-litre Ford Puma 'common rail' diesel engine. It is also equipped with a variable geometry turbocharger, ECU, and EGR, which is the one of the emissions reduction devices featured on this engine. The EGR was deactivated by unplugging it from the engine to obtain high levels of NO_x that were required for these studies. Fig 4.2 shows the engine mounted to the test rig:

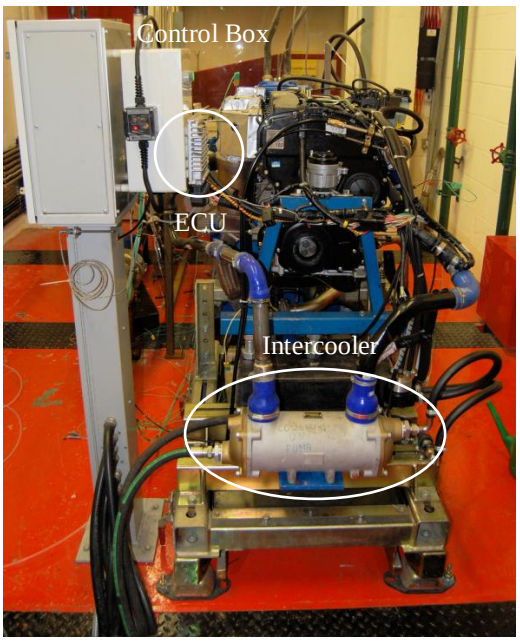

Fig 4.2: Engine mounted to the test bed. The ECU is circled on the left of the image. The pressure transducers and thermocouples are connected to the control box on the far left. Temperatures, pressures, and emissions levels were logged using a Froude Texcel v12, which is a system that allows the user to remotely control the engine conditions, pumps and the fans inside the test cell, the emissions analysers, and also acts as a monitoring and logging tool. The mass flow rate was obtained via GREDI, collects data from the ECU. The intercooler, which is circled at the bottom, is connected to the test cell water supply to cool the warm air as it exits the turbocharger.

Fig 4.3 and Fig 4.4 show the engine EGR and the plug used to deactivate it, whilst Tab 4.1 describes the specification of the engine used in the experiments.

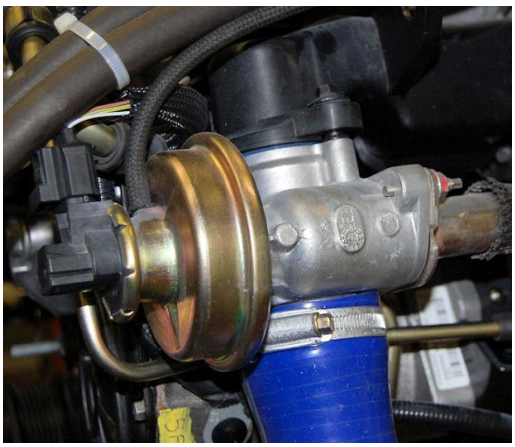

Fig 4.3: Engine EGR.

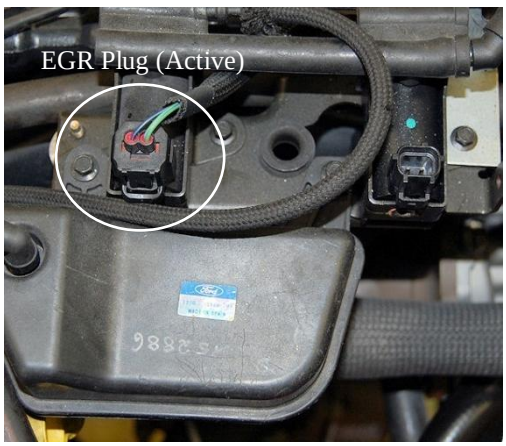

Fig 4.4: EGR plug (circled).

Items	Description
Capacity	1998cc
Number of Cylinders and Configuration	4 Inline
Max Power	96kW (129bhp) at 3800rpm
Max Torque at 1500rpm	280Nm
Max Torque at 1800rpm	330Nm
Aspiration Type	Turbo
Compression Ratio	18.2:1

Tab 4.1: Engine specifications.

The fuel injection system used in this particular engine is a common rail diesel injection system. Common rail systems work by a high pressure pump that is driven by the engine drive belt forcing the fuel into a reservoir known as the 'rail', which supplies fuel to the injectors. This system has numerous advantages over standard injection systems, one of which is the improved atomisation of the diesel inside the cylinder due to the high pressures involved; this leads to improved engine performance and improved fuel economy. A schematic of the fuel rig is presented in Fig 4.5:

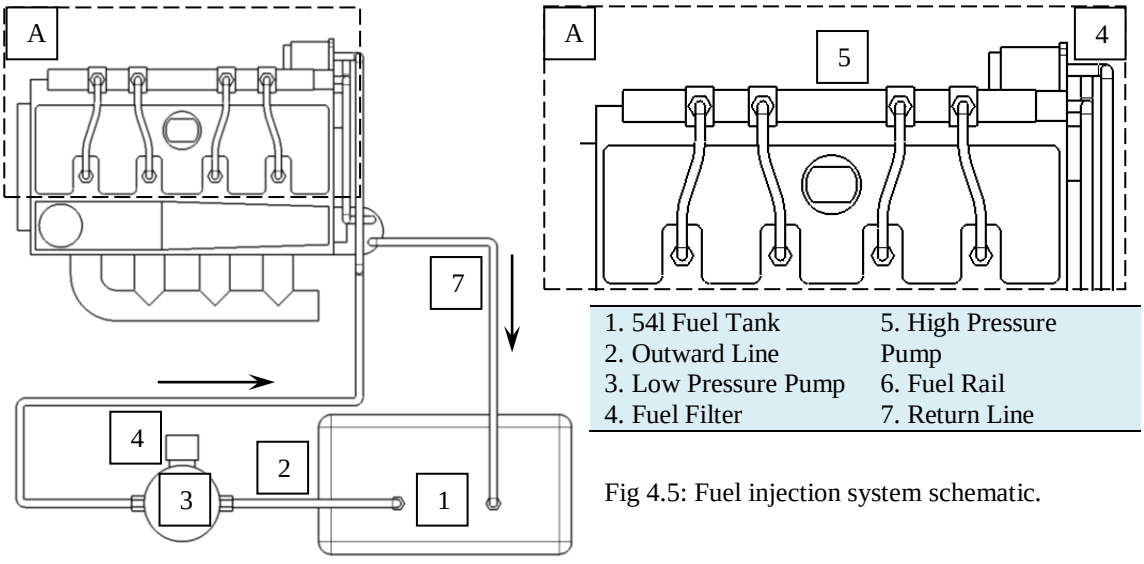

1. 54l Fuel Tank	5. High Pressure Pump
2. Outward Line	
3. Low Pressure Pump	6. Fuel Rail
4. Fuel Filter	7. Return Line

Fig 4.5: Fuel injection system schematic.

The fuel used in the engine tests is a low-sulfur diesel to minimse the effect of sulphur poisoning on the catalysts. [Shibata et al, 2007] A fuel cooling module was installed to cool down the diesel so that the fuel temperature did not exceed its flash-point. Any sediment in the fuel is filtered out using a filter, which is attached to the low pressure pump.

4.3 Catalyst Sizes and Quantities

The exhaust rig was manufactured in-house and was designed to allow for different catalyst sizes and configurations to be investigated. Gaskets were placed in between each component to prevent any exhaust gas escaping into the cell. The catalysts were supplied by Johnson Matthey and were canned by Faurecia. Tab 4.2 describes the SCR and oxidation catalysts supplied with respect to volume and quantity available:

Catalyst Type	Volume (litres)	Quantity
Single DOC	1	1
Double DOC	2	1
Single SCR	1	1
Double SCR	2	2
1/3 SCR in Full-Size Can	0.33	1
½ SCR in Full-Size Can	0.5	1
1/3 SCR in Half-Size Can	0.33	2
½ SCR in Half-Size Can	0.5	1

Tab 4.2: Catalyst quantities.

4.4 Ammonia Gas Injection

For the purpose of CFD model validation ammonia gas was injected into the exhaust rather than the urea; this allows for a simpler model as urea thermolysis and hydrolysis can be excluded. The gas mixture consists of 5% ammonia gas in balance N_2 at 150bar gauge pressure. Fig 4.6 displays the set-up used for the gas studies:

1. DOC/ DPF Assembly	5. Master Gauge
2. Expansion Box	6. Flowmeter
3. SCR Assembly	7. Exhaust Injection Line
4. Gas Bottle	8. Ventilation Line

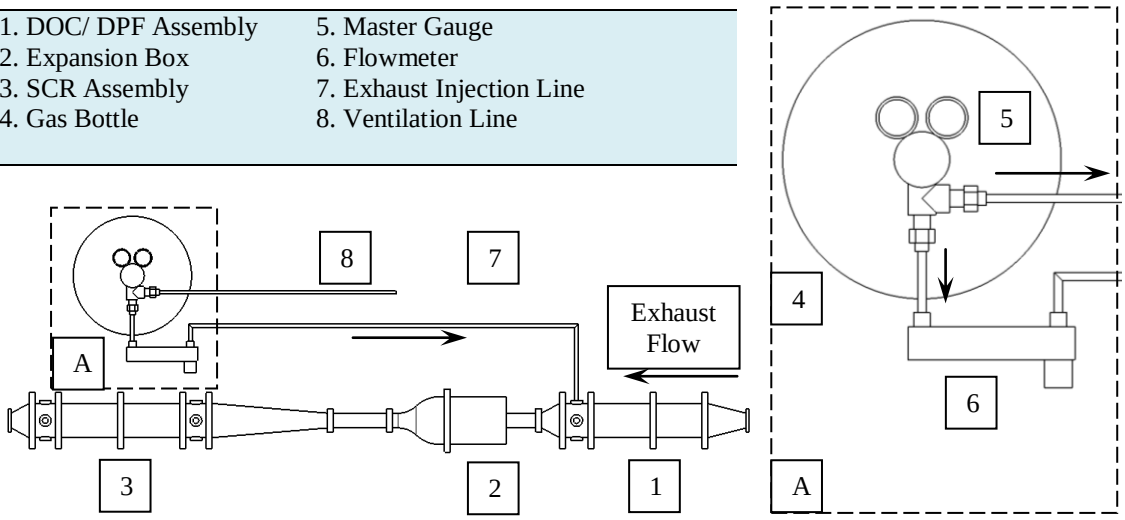

Fig 4.6: Gas injection schematic.

The amount of ammonia gas injected into the exhaust was controlled via the main value connected to the master gauge; this was done to avoid damaging the needle valve on the flowmeter. Fig 4.7 plots the steel and glass float calibration curves for the ammonia gas mixture used in the experiments in this thesis:

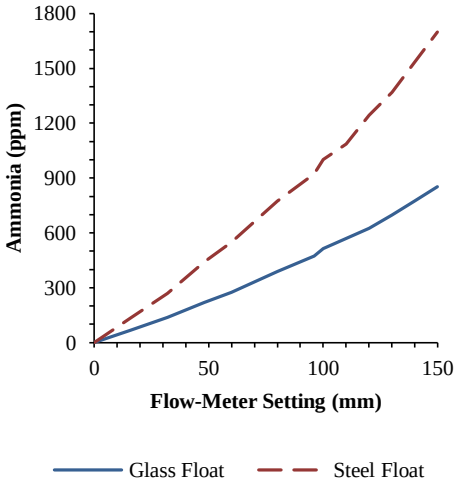

Fig 4.7: Flowmeter calibration curves for an exhaust gas mass flow rate of 31g.s^{-1}.

The height of the floats in the flowmeter were based on the upstream NO_x reading when no ammonia was injected. If the required ammonia concentration was less than 800ppm, the glass float was used, the steel float was used when the required concentration exceeded 800ppm.

4.5 EXSA 1500 Analyser

The Horiba EXSA 1500 is designed to measure different types of emissions from small engines. There are three analysers in the unit, these are: FID or 'flame ionisation detector' to measure hydrocarbons, a NDIR or 'non-dispersive infrared spectrometer' to analyser CO and CO_2, and a CLD or 'chemiluminescence detector' for NO_x emission detection. The EXSA can also analyse the oxygen concentration in the exhaust, lambda, and the air: fuel ratio. The EXSA was positioned just downstream of the turbocharger with the purpose of acting as a validation tool for the MEXA. Fig 4.8 describes the principle operation of the CLD on the EXSA.

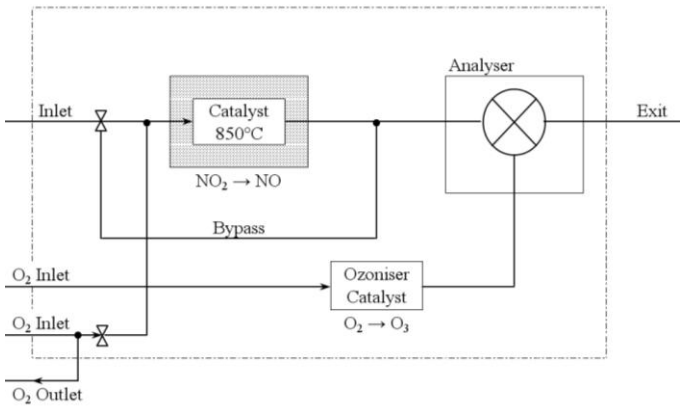

Fig 4.8: EXSA 1500 CLD schematic.

When the EXSA is put into 'NO_x' mode, the exhaust enters the NO_2 to NO converter catalyst, which is heated to a high temperature to convert NO_2 to NO, as described in equation (19), this converter is bypassed when the analyser is in 'NO' measurement mode. Equation (50) describes the conversion of oxygen to ozone via the ozoniser catalyst shown in Fig 4.8:

$$3O_2 \rightarrow 2O_3 \quad (50)$$

These two gases then enter the analyser in which the NO reacts with the O_3 to produce excited NO_2:

$$NO + O_3 \rightarrow NO_2^* + O_2 \quad (51)$$

The excited NO_2 molecules then produce light energy, as described in equation (52), which is then measured, and it is from this that the total NO_x or NO concentration can be derived. The MEXA-1170 Nx operates via exactly the same principle.

$$NO_2^* \rightarrow NO_2 + light \quad (52)$$

The main differences between the EXSA and the MEXA is that the EXSA can only measure in one of these modes at a time. Therefore in the case of engine NO_x maps, tests are undertaken twice, one in each mode. The concentration of NO_2 present can be calculated by subtracting the value of NO, from the total NO_x concentration.

A schematic showing the experimental configuration of the EXSA, and the gases required is located in Appendix 1.1. Tab 4.3 and Tab 4.4 describe the pre and post test procedures for the EXSA respectively:

Task Number	Procedure
1	Switch on gas bottles and EXSA, check regulators inside the test cell and in the bottle storage area.
2	Light the flame for the burner on the EXSA and switch on the ozone generator.
3	Once the heated line is up to temperature (approximately 190°C), the EXSA can be calibrated.
4	Purge the EXSA for 60 seconds.
5	Switch EXSA from local mode (EXSA) to host mode (Texcel).

Tab 4.3: Pre-test procedure for the EXSA.

Task Number	Procedure
1	Purge the EXSA for 60 seconds.
2	Calibrate the EXSA to ensure that the analysers are still working properly.
3	Check the gas bottles in the store room if required.
4	Check the front filters for dirt and water, and remove any excess water if necessary.
5	Switch off the ozone generator and shut down the EXSA computer.
6	Turn the analyser off at the mains.

Tab 4.4: Post-test procedure for the EXSA.

4.6 MEXA-1170 Nx Analyser

The Horiba MEXA-1170 Nx is specifically designed to measure NO_x and ammonia emissions from vehicle exhaust systems. Its ability to measure ammonia makes it ideal for SCR testing. Like the EXSA. The MEXA measures NO_x and ammonia via chemiluminescence, however it houses two CLD analysers instead one; this means that either NO + NO_2, or NH_3 + NO_x can be measured. The main limitation of this method of measurement is its inability to detect N_2O that could be present in the exhaust. Fig 4.9 shows a photograph of the MEXA:

Fig 4.9: MEXA-1170 Nx. [Tamaldin, 2010] The MEXA and the EXSA share some of the gases, therefore the gas lines exiting the regulators inside the test cell were teed off to fit both analysers. The control panel (circled) was used to operate the MEXA during the experiments as the MEXA could not be controlled via the Texcel v12.

The MEXA is connected to a 16A three-phase socket located inside the test cell. It is required that the humidity must be in stable range up to 80% with no condensation surrounding the system, whilst the operating temperature should be between 5°C and 40°C. It is also necessary that the analyser was not placed close to any heat sources or anything that provides an electromagnetic field.

The MEXA does not feature a gas dryer inside the analyser to remove any water that is present, therefore adequate drainage is needed to remove any water from the system. A water pipe was connected directly to the main water system inside the test cell.

One of the potential disadvantages in the measurement of NO_x and ammonia using the CLD is the potential for ammonia to interfere with NO_x measurements. Such problems that could arise are poisoning of the NO_x to NO converter catalyst [Shah et al, 2007], or ammonia oxidation taking place over this catalyst as described in equation (53):

$$4NH_3 + 5O_2 \rightarrow 4NO + 6H_2O \quad (53)$$

The basic function of the MEXA for both measurement modes is described in Tab 4.5:

Measurement Mode	NH_3 Oxidation Catalyst Status	Species Measured	Species Calculated
NH_3 Mode	On	Sum and NO_x	NH_3 = Sum - NO_x
NO_2 Mode	Off	NO_x and NO	NO_2 = NO_x - NO

Tab 4.5: MEXA function. When the MEXA is in 'NO_2' measurement mode, the ammonia oxidation catalyst can be switched off to reduce the effect of thermal aging on the catalyst efficiency as equation (53) is avoided.

The ammonia and NO_2 readings calculated via the formulae in Tab 4.5 are then corrected for the ammonia and NO_x converter catalyst efficiencies respectively. Equation (54) calculates the corrected concentrations for NO_2 and ammonia based on their respective catalyst efficiencies, where C_i is in ppm:

$$C_{i-Corrected} = \frac{C_{i-Detected} \times Eff}{100} \quad (54)$$

The ammonia converter calatyst efficiency was obtained via an analysis undertaken inside the MEXA using the span and calibration gases, however, the efficiency calculation for the NO_x converter catalyst requires a gas divider, which converts some of the NO from the gas bottle to NO_2, it was therefore necessary for the NO_x converter catalyst efficiency check to be carried out by an engineer from Horiba.

Previous investigations at Coventry University discovered that ammonia reacting with NO_2 over the $NO_2 \rightarrow$ NO converter catalyst was found to be the main problem with the measurements. Tab 4.6 shows how the presence of ammonia affects the readings:

Tab 4.6: Effects of ammonia on gas concentrations. [Tamaldin et al, 2010]

Research into this area by Ford had concluded that ammonia would have to be removed from the sampling gas. Removal of the ammonia was achieved via the use of 'scrubbers' comprising of Phosphoric Acid or H_3PO_4 mixed with deionised water and methanol was proposed to adsorb the ammonia. Results from this work showed that the effect of ammonia is minimised, as the scrubbers adsorb the ammonia. [Shah et al, 2007] The MEXA-1170 Nx required scrubbers based on these recommendations. A schematic of the MEXA with the ammonia scrubbers is displayed in Fig 4.10:

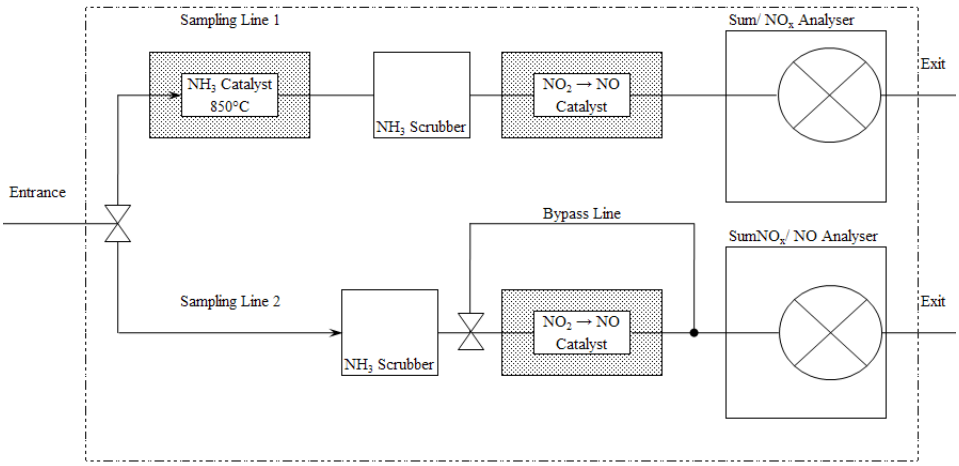

Fig 4.10: MEXA schematic with ammonia scrubbers.

Tab 4.7 and Tab 4.8 describe the pre and post test procedures for the MEXA respsectively:

Task Number	Procedure
1	Turn on the gas bottles (if not done already) and take the MEXA out of stand-by mode.
2	Check finger filter at the back for dirt.
3	Ensure that the operating mode of the MEXA is 'NH_3 + NO_x'. The NH_3 oxidation catalyst requires time to heat up.
4	Calibrate the MEXA.
5	Check the NH_3 converter efficiency. If the efficiency drops below 80%, the analyser will not function in 'NH_3 + NO_x' mode.*
6	Save the efficiency value and input it into the Texcel.

Tab 4.7: Pre-test procedure for the MEXA. *: The ammonia oxidation catalyst requires approximately 15 minutes to reach operating temperature.

Task Number	Procedure
1	Re-calibrate the MEXA.
2	Re-check the NH_3 oxidation catalyst efficiency. The test is void if the efficiency is less than 80%.
3	Check filters and water line.
4	Put MEXA into stand-by mode - do not turn off.

Tab 4.8: Post-test procedure for the MEXA.

4.7 Experimental test procedures

Fig 4.11 describes the test procedure used for the engine NO_x maps with no ammonia gas, for these tests, the MEXA was positioned at sampling point 2, as described in Fig 4.1. The objective of the NO_x maps was to determine which DOC/DPF combination provides an NO_2: NO_x ratio closest to 0.5.

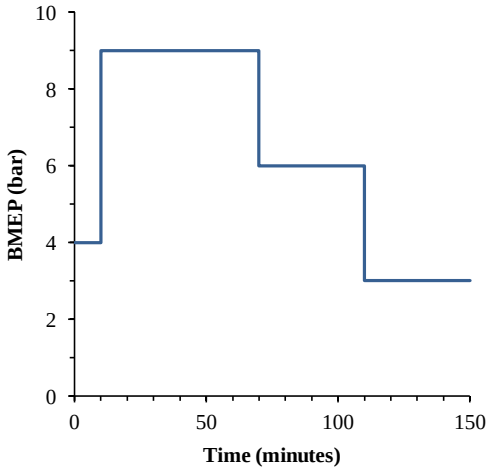

Fig 4.11: NO_x map test procedure. The engine speed was maintained at 1500rpm throughout NO_x maps, only the engine load was changed.

The test procedure described in Fig 4.11 was undertaken for three different engine loads to obtain a broader range of NO_2: NO_x ratios for different exhaust gas temperatures; this was input into the Texcel control system, which controlled the load applied to the engine.

The engine load was initially operated at 4bar BMEP for 10 minutes to allow the oil and water to warm up before the tests, this initial procedure was also conducted for the gas tests. Tab 4.9 describes the DOC/DPF combinations used in the engine NO_x mapping:

Upstream of DPF	Downstream of DPF
1 DOC	1 DOC
2 DOCs	2 DOCs

Tab 4.9: DOC/DPF combinations.

The DPF was cleaned before each test that involved placing the DOC downstream of the DPF to minimise the effect of NO_2 regeneration from the soot left over from previous tests; this maintained continuity throughout these tests. The engine logs for these tests are located in Appendix 3.1 of this thesis.

The tests for the steady-state and transient experiments are described in Fig 4.12 and Fig 4.13 respectively:

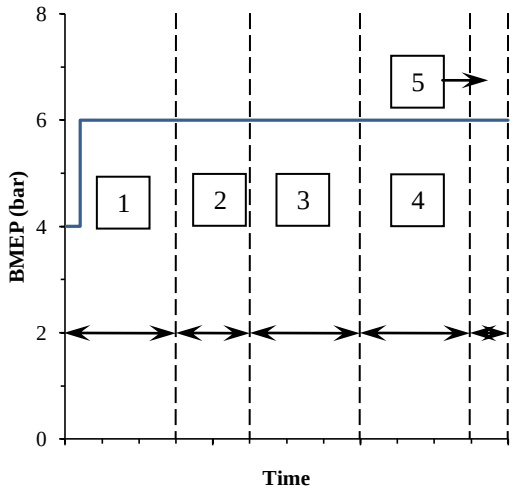

Fig 4.12: Steady-state test procedure.

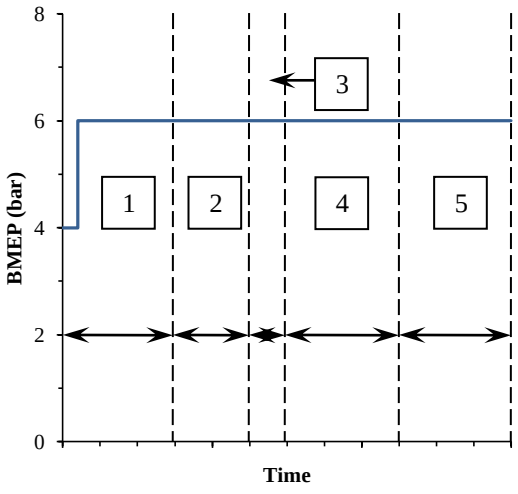

Fig 4.13: Transient test procedure.

Tab 4.10 describes the stage numbers, the actions undertaken during these, the locations, and the measurement modes of the MEXA for the steady-state tests described in Fig 4.12. It was anticpated that as the size of the bricks increase, the steady-state response time would also increase, therefore a time pre-determined allocation for each measurement stage was rejected for the gas tests.

Stage Number	MEXA Mode	MEXA Position	Gas Injection (α_1)	Description
1	NH_3 Mode	Upstream of SCR	-	Engine warm-up
2	NH_3 Mode	Upstream of SCR	0.5, 1.0, 1.5	Flowmeter setting check, and scrubber check
3	NH_3 Mode	Downstream of SCR	0.5, 1.0, 1.5	First sampling stage
4	NO_2 Mode	Downstream of SCR	1.5, 1.0, 0.5	Second sampling stage
5	NO_2 Mode	Upstream of SCR	-	NO_2: NO_x sampling stage

Tab 4.10: Stage numbers described in the steady-state test procedure.

It can be seen that in Tab 4.10 that stage 4 is not a replication of stage 3 with respect to the gas injection, this was due to the need to reduce the amount of ammonia gas used in the experiments , and also time constrictions that are often associated with off-site testing.

Tab 4.11 and Tab 4.12 describe the stage numbers for the transient tests described in Fig 4.13, when the MEXA is in 'NH_3' and 'NO_2' measurement modes respectively. The transient tests were broken up due to time constraints. Stage 3 is ignored for the tests in Tab 4.10.

The engine logs for the steady-state tests can be found in Appendix 3.2 and Appendix 3.3 of this thesis.

Stage Number	MEXA Mode	MEXA Position	Gas Injection (α_1)	Description
1	NH_3 Mode	Upstream of SCR	-	Engine warm-up
2	NH_3 Mode	Upstream of SCR	0.5, 1.0, 1.5, 2.0	Flowmeter setting check, and scrubber check
3*	NO_2 Mode	Upstream of SCR	-	NO_2: NO_x sampling stage
4	NH_3 Mode	Downstream of SCR	2.0, 1.5, 1.0, 0.5, 0.0	Sampling stage
5	NH_3 Mode	Upstream of SCR	0.5, 1.0, 1.5, 2.0	Scrubber check

Tab 4.11: Stage numbers described in the transient test procedure when the MEXA is in 'NH_3' mode.

Stage Number	MEXA Mode	MEXA Position	Gas Injection (α_1)	Description
1	NH_3 Mode	Upstream of SCR	-	Engine warm-up
2	NH_3 Mode	Upstream of SCR	0.5, 1.0, 1.5, 2.0	Flowmeter setting check, and scrubber check
3	NO_2 Mode	Upstream of SCR	-	NO_2: NO_x sampling stage
4	NO_2 Mode	Downstream of SCR	2.0, 1.5, 1.0, 0.5, 0.0	Sampling stage
5	NH_3 Mode	Upstream of SCR	0.5, 1.0, 1.5, 2.0	Scrubber check

Tab 4.12: Stage numbers described in the transient test procedure when the MEXA is in 'NO_2' mode.

Chapter 5: CFD Methodology

This chapter describes the procedure used in creating a 1D model of the SCR catalyst using the porous medium approach in STARCD version 4.1. It describes the modelling process, species transport, as well as enthalpy and pressure losses. The model was validated against tests described in the same literature as the reaction scheme, and can be found in Appendix 2.6.

5.1 Geometry and Mesh Creation

The model comprises of three segments: the gas inlet, the porous medium (solid and gas phases), and the gas outlet. Tab 5.1 describes the dimensions of each section and its respective mesh size, whilst Fig 5.1 displays the CFD model:

Section	Length (mm)	Width (mm)	Height (mm)	Number of Cells
Gas Inlet	30	10	10	5 x 5 x 6
Porous Medium	364	10	10	5 x 5 x 91
Gas Outlet	30	10	10	5 x 5 x 6

Tab 5.1: Geometry and mesh sizes. The length of the model is based upon that of four SCR bricks as used in previous studies. Each cell on the (x,y) axis represents a single channel on the experimental catalyst.

A 5 x 5 cell cross-section was used because STAR CD is unable to work for a single cell cross-section.

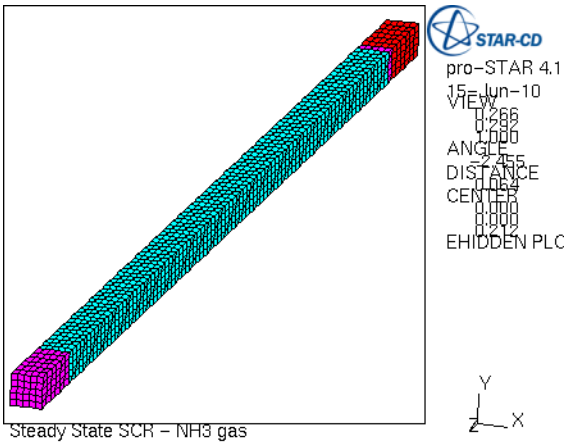

Fig 5.1: CFD Model. The red set of blocks are the gas inlet (top right), the turquoise set of blocks represent the porous medium, and the purple cells (bottom left) correspond to the gas outlet. The z-axis is the direction of travel along the monolith.

5.2 Summary of the Modelling Process

The model used in this investigation utilises several user subroutines written using Fortran 77. Each subroutine focuses on different areas of the model, the principles on which the subroutines are based are outlined in Appendix 2.2. A brief summary of each user subroutine used in the construction of the model is described:

- **Para.inc**: This is an 'include' file in which fixed parameters and constants are exported to the subroutines 'Sorsca.f', 'Sorent.f', 'Porht.1', and 'Porht.1'. The input parameters include channel properties, mass transfer coefficients, inlet species concentrations, diffusivity coefficients for the individual species in air and on the washcoat, and the molecular mass ratios. Values for these input parameters are located in Appendix 2.2.
- **Bcdefi.f**: This subroutine is used for the definition of boundary conditions. The parameters that are input into this subroutine are the inlet velocity, the upstream concentrations of oxygen, NO, NO_2, N_2O, and ammonia. Further information about this user-subroutine can be found in Appendix 2.3.1 of this thesis.
- **Initfi.f**: Allows the user to initialise dependent parameters to arbitrary constants as a function of the z co-ordinate.
- **Poros1.f**: Used in the calculation of pressure losses along the monolith, the formulae used to calculate this are described in equations (58) – (62) in Section 5.4.
- **Sorsca.f**: This subroutine calculates the mass transfer of each species between the monolith channel and the washcoat, as well as species production and consumption via the SCR reactions on the washcoat. Appendix 2.3.3 describes the steps that were undertaken to achieve this.
- ***Sorent.f**: Subroutine for calculating heat transfer from the washcoat to the gas in the channel, and primarily deals focuses on the heat generated and consumed via the SCR reactions that take place on the washcoat.
- **Porht.1**: Used in the calculation for heat transfer from the gas in the channel to the washcoat; this user subroutine also accounts for developing flow just after the inlet of the monolith.
- **Porht.2**: Used to determine the temperature of the surface of the washcoat based using the 'thin film approximation', which is the mean value of the channel and the washcoat.

*: It was observed during the initial investigations that the amount of heat generated by the SCR reactions was noticeably higher than expected; this was attributed to a bug in the programming of STAR-CD Version 4. It was therefore decided to not include this in the analyses, since the exotherm is considered to be quite small; it was anticipated that this would have only a minor influence on the SCR reactions. Other mathematical models also neglect these exotherms. [Chatterjee et al, 2007] and [Olsson et al, 2008].

Heat transfer between the washcoat and the channel, and between the channel and the washcoat was originally undertaken in the user-subroutine 'Sorent.f' in STAR CD version 3.26. In version 4, however, heat transfer from the channel to the washcoat is now calculatedusing the subroutines 'Porht.1' and 'Porht.2'. The analysis process is outlined in Fig 5.2:

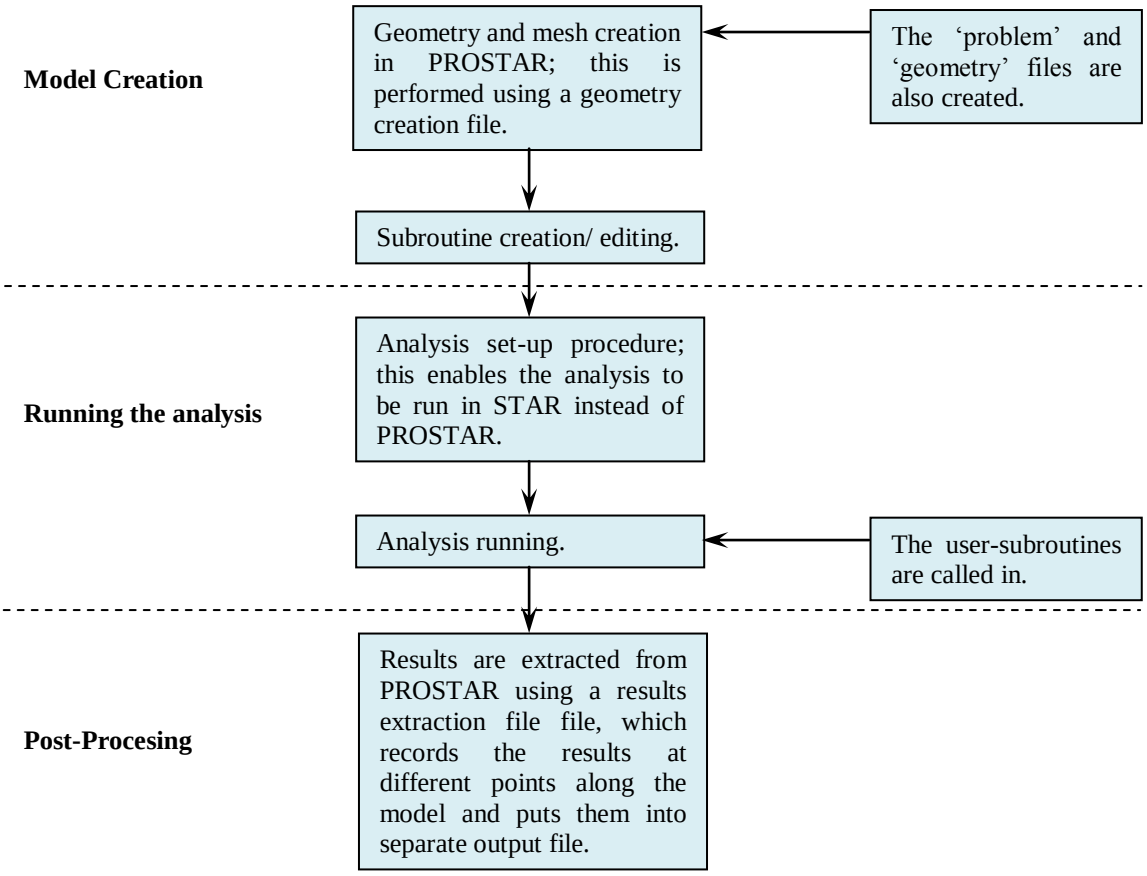

Fig 5.2: Analysis process. STAR CD has two programs: PROSTAR, which is used in the creation of the model geometry, and STAR, where the analysis is undertaken.

Equation (55) describes the process of converting particles per million ($C_{i\text{-}ppm}$) into mass fraction; this equation is used for NO, NO_2, and ammonia:

$$C_{i-MF} = \frac{C_{i-ppm}}{1\times10^{6}} \times \frac{MM_i}{MM_{Air}} \quad \text{(55)}$$

Equation (56) describes the process used to convert oxygen from a percentage ($C_{O2\text{-}\%}$) into a mass fraction:

$$C_{O2-MF} = \frac{C_{O2-\%}}{100} \times \frac{MM_{O2}}{MM_{Air}} \quad \text{(56)}$$

where $C_{i\text{-}MF}$ and $C_{O2\text{-}MF}$ are the species concentrations expressed as a mass fraction, which are put into the include file 'para.inc'.

It can be assumed that because of the high content of nitrogen and oxygen in a diesel exhaust, the molecular mass of the exhaust gas is similar to that of air, therefore the molecular mass of air, denoted by MM_{Air}, is used for equations (55) and (56).

5.3 Parameter Initialisation

The input parameters used in the model were primarily defined using the user subroutines 'Bcdefi.f', 'Initfi.f' and 'Poros1.f'. Inlet velocity and species input are calculated from information used in the engine tests. The mean value for each input parameter was used due to variation from test-to-test, for the case of NO and NO_2, these were calculated based on the NO_2: NO_x ratio upstream of the SCR.

It was assumed that the gas inlet velocity is assumed to be axial, the radial velocities (velocities in the x and y-directions) are set to $0 m.s^{-1}$. Velocity is calculated based on the mass flow rate and the exhaust gas temperature just before the SCR catalyst using data obtained from GREDI and Texcel respectively. The area of the catalyst used in the model is the area of the experimental catalyst, although the frontal area of the model is significantly smaller than the experimental SCR; the simulations focus on only a small section of an actual catalyst to reduce computational time. Input scalars are defined 'Para.inc', whilst the kinetic parameters and input scalars are input into 'Sorsca.f' and 'Sorent.f', and can be found in Appendix 2.1 and 2.2 respectively.

5.4 Channel Properties

The monolith porosity is the fraction of the total cross-sectional in a single channel (including the wall and the washcoat) area available for the exhaust gas to travel through. Fig 5.3 shows a cross-sectional diagram of one of the channels, the dimensions of which are constant across the catalyst:

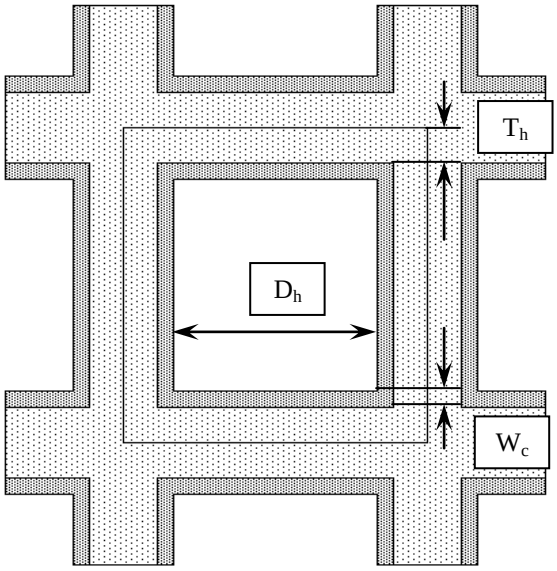

Fig 5.3:Cross-section of one of the channels on the experimental catalyst. The hydraulic diameter (D_h) is assumed to be the width of the inside of the channel, and T_h denotes the thickness of half of the channel wall. The washcoat thickness (W_c) is 10 microns.

The CFD model, however, does not assume that the porous medium section is constructed in the way described in Fig 5.3, therefore the equivalent porosity of the experimental catalyst is required for the model. Equation (57) calculates the porosity value of the porous medium, which is based on the dimensions of a single channel on the experimental catalyst:

$$\varepsilon = \frac{D_h^2}{(D_h + 2(W_C + T_h))^2} \quad \text{.....} \quad (57)$$

Pressure drop along the model is derived from the Darcy equation as shown in equation (58) [Day, 2001]; this assumes that flow along the substrate is laminar and fully developed. The pressure drop effects at the entrance and the exit of the monolith, however, are neglected because of the 1D geometry as well as the effects of developing flow, which are necessary due to the short length of the catalyst.

$$\frac{\partial P}{\partial x} = -f\,\mathrm{Re}_C \frac{\mu U_C}{D_h^2} \quad \text{(58)}$$

The relationship described in equation (59), derived from the Darcy equation calculates the pressure drop along the monolith by allowing the user to input permeability coefficients α and β [Disdale, 2007]:

$$\frac{\partial P}{\partial x} = -KU_s \quad \text{(59)}$$

where K is calculated via the following term [CD-adapco, 2010]:

$$K = \alpha_2 |\vec{v}| + \beta \quad \text{(60)}$$

Equation (60) assumes that K is a quasilinear function of the superficial, or inlet velocity $|\vec{v}|$ in the axial direction, [CD-adapco, 2010], however, because this model is only one-dimensional, the value for the inlet velocity, denoted by U, is used, as described in equation (61):

$$\frac{\partial P}{\partial x} = -\alpha_2 U - \beta_2 \tilde{U} \quad \text{(61)}$$

The permeability term α is inhibited as the model deals with relatively low flow rates, therefore only leaving the β term, which is calculated via equation (63), which is input into the user subroutine 'Poros1.f':

$$\beta_2 = \frac{2f\,\mathrm{Re}_C \nu\rho}{\varepsilon D_h^{\,2}} \quad \text{(62)}$$

where the kinematic viscosity of air denoted by ν, was derived as a function of temperature. The product of $f\,\mathrm{Re}_C$ is 14.227 for square channels, however, this varies for channels that have different shapes. [Shah, 1978]

5.5 Species Transport

The general conservation equation for a 3D model is described in equation (63); this is used for calculating species transport in the exhaust pipe [Benjamin et al, 2007]:

$$\frac{\delta}{\delta}\frac{(\rho C)}{t} + \nabla(\rho U C) - \nabla\left[\left[\frac{\mu_t}{\sigma_s} + \rho D\right]\nabla C\right] = Source(kgm^{-3}s^{-1}) \quad \text{(63)}$$

The terms from left-to-right are: the transient term; this is the change in species concentration with respect to time, the convective term, the diffusion flux term, and the 'Source' term. It is important to identify where these terms are applicable depending on where in the exhaust system one wishes to analyse. Tab 5.2 obtained from literature describes the various forms of the transport equation required for the inlet and exit pipes, the monolith channels, and the washcoat:

Section	Inlet and Exit Pipes	Monolith Channels	Washcoat
Source Term	Excluded	Included	Included
Transient Term	Included	Included	Included
Convective Term	Included	Included	Excluded
Diffusion Flux Term	Included	Suppressed	Suppressed

Tab 5.2: Summary of terms included/excluded from transport equation depending on location. [Benjamin et al, 2007]

Equation (64) describes species transport on the catalyst washcoat, the convective term is excluded from the solid phase as the gas pores on the washcoat are very small and that each species cannot travel from pore-to-pore whilst in the solid phase of the model. The change in gas pore concentrations, denoted by $C_{i\text{-}Sol}$, was modified on the right-hand side of the equation by including the relevant SCR reactions depending on the species; this is multiplied amount of reactor volume inside the monolith occupied by reaction sites is calculated from the expression: $\left[\frac{\varepsilon_2}{V_W}\right]$, which is about 5%.

$$\varepsilon\frac{\partial}{\partial t}[\rho_{air}C_{isol}] = \{K_{mi}\rho_{air}A_v[C_{i-gas} - C_{i-sol}] + Mr_{i-\Omega}\}\left[\frac{\varepsilon_2}{V_W}\right] \text{.....} \quad (64)$$

where $C_{i\text{-}gas}$ and $C_{i\text{-}sol}$ are expressed as a mol-fraction.

The gas phase transport equation used in the model is described in equation (65), it is assumed that the SCR reactions can only take place on the washcoat, therefore the reactions are excluded from the gas phase. It is observed that when equation (65) is compared with equation (63), convection is only accounted for along the model; this is because the cross-sectional flow distribution is uniform, and also allows for the inhibition of convection from channel-to-channel, creating a 1D expression.

$$\varepsilon\frac{\partial}{\partial t}[\rho_{air}C_{gas}] + \frac{\partial}{\partial z}\rho_{air}U_S C_{gas} = -K_{mi}\rho_{air}A_v[C_{ig} - C_{isol}] \text{.....} \quad (65)$$

where the source term $= -K_{mi}\rho_{air}A_v[C_{ig} - C_{isol}]$ kg.m^{-3}.s^{-1}.

Diffusion inside the gas-phase of the monolith is very small when compared with mass transfer, and therefore can be surpressed. Suppression of this in equation (65) is achieved by inputting very large and very small values need to be applied to the 'Turbulent Schmidt Number' (σ_s) and the 'Diffusion Flux' term (D) respectively, which are in the region of 1.0E+28 and 1.0E-28 respectively as these are the maximum values that STAR CD will permit. [Benjamin et al, 2007]

Each species concentration in the gas phase was calculated using Avogadro's gas law, as described in Appendix 2.33. The bulk mass transfer coefficient K_{mi} for each species, that is, the mass transfer coefficient for the gas phase plus the washcoat is calculated via equation (66):

$$K_{mi} = \frac{k.D}{D + k.H} \quad \text{.....} \quad (66)$$

where the diffusion coefficients for both phases in the model are corrected for temperature. A complete derivation of this formula is provided in Appendix 2.4.

Equation (67) describes the total reaction rates for each species are calculated by multiplying the rate with the number of available reaction sites and the stoichiometric coefficient denoted by O_i, which is the number of molecules for each species on the left-hand side of the chemical reaction equation [Olsson et al, 2008]:

$$r_{i-\Omega} = O_i \times r_i \times \Omega \quad \text{.....} \quad (67)$$

where Ω is the number of reaction sites input into the 'include' file 'para.inc'.

The reaction scheme used in the CFD model is the one produced by Chalmers University, and can be found in section 2.5.3.3 of this report, with the rate parameters provided in Appendix 2.1. This scheme was chosen because all of the basic ammonia-SCR reactions are included in their model for Cu-zeolite. Thermolysis and hydrolysis of urea is excluded as ammonia gas was used instead of urea.

5.6 Heat Transfer

The conduction equation for the catalyst substrate wall in a porous medium model is explained in equation (68) [Benjamin et al, 2003]:

$$\rho_{Sol}\left(1-\varepsilon_2\right)C_W \frac{\partial T_W}{\partial t} - \left(1-\varepsilon_2\right)k_W \frac{\partial^2 T_W}{\partial z^2} = -hA_V\left(T_W - T_{Gas}\right) \quad \text{.....} \quad (68)$$

where the source term $= -hA_V\left(T_W - T_{Gas}\right)$ W.m^{-3}. Equation (69) describes heat transfer in the gas phase [Benjamin et al, 2003]:

$$\rho_{Gas}\varepsilon_2 Cp_{Gas}\left[\frac{\partial T_{Gas}}{\partial t}+U_C\frac{\partial T_{Gas}}{\partial z}\right]-\varepsilon_2 k_{Gas}\frac{\partial^2 T_W}{\partial z^2}=-hA_V(T_{Gas}-T_W)\ldots. \quad (69)$$

where U ($m.s^{-1}$) is the axial velocity component.

The model focuses on a small section of channels in the middle of the SCR brick, therefore for simplicity, the model is adiabatic, where heat transfer to the atmosphere is neglected. Heat transfer is only accounted for along the monolith and between the solid and gas phases, the cross-sectional temperature distribution in the channels is also assumed to be uniform with the exception of the washcoat surface temperature.

The heat transfer coefficient, or h, was obtained via equation (70) for the gas phase only, and was coded into 'Porht1.f':

$$h=\frac{Nuk_{Gas}}{A_V} \quad \ldots\ldots\ldots\ldots\ldots\ldots\ldots\ldots\ldots\ldots\ldots\ldots\ldots\ldots\ldots\ldots\ldots\ldots\ldots\ldots\ldots\ldots \quad (70)$$

where the thermal conductivity, or k_{Gas} was temperature dependent; this was done by using the thin film approximation.

5.7 Develpoing Flow

The Nusselt number is defined as the ratio of convection to conduction, which equates to 3.608 for fully developed laminar flow in a square or rectangular channel. At the entrance to the monolith, however, the flow is not fully developed; therefore the Nusselt number for fully developed flow would not be applicable, experimental data has shown that the Nusselt number for under-developed flow is larger. [Shah, 1978] The coefficients for heat and mass transfer are multiplied by elevation ratios, which are taken for the centre of each cell in the porous medium, the values of which are located in Appendix 2.5. Fig 5.4 plots the elevation ratios with respect to catalyst length, or the z co-ordinate:

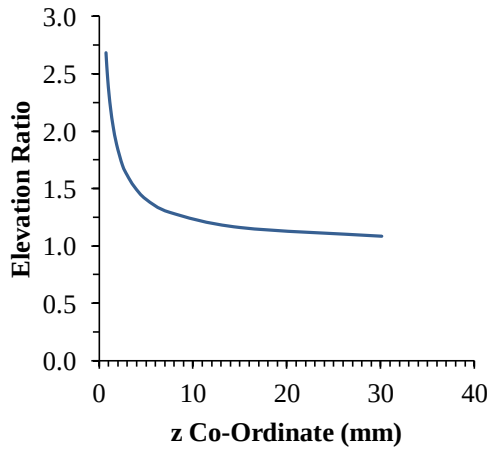

Fig 5.4: Elevation ratios at the brick inlet. After about 25mm from the entrance of the channel, the flow is assumed to be fully developed, therefore both heat and mass transfer coefficients are assumed to be correct.

5.8 Number of Available Reaction Sites

The model derived by Chalmers University requires the number of reaction sites, denoted by Ω, to be specified, in the literature this value is assumed to be an arbitrary constant of 200mol-sites.m^{-3}. [Olsson et al, 2008] Investigations into this area has, in fact, shown that the number of available reaction sites is temperature dependant. A term was therefore supplied to account for this sensivivty to temperature:

$$\Omega_{Corrected} = \Omega_{Input}\left[\frac{298}{T_W}\right]^2 \quad \text{.....} \quad (71)$$

where Ω_{Input} is the number of reaction sites input into the user-subroutine 'para.inc', and T_W is the wall temperature in K.

From the experiments that were undertaken in this thesis, it was very difficult to determine the number of available reaction sites on the catalyst washcoat, the number of reaction sites was varied between 200 and 500mol-sites.m^{-3} in increments of 100mol-sites.m^{-3} to obtain the best estimate.

5.9 Post-Processing

Data from STAR-CD was exported using a post processing file that allows the species and temperature profiles along the brick to be obtained. The coding works via the creation of vertices along the model, where numerical values are read and written into a separate file. This route allows further processing of the results in this file to be undertaken outside of STAR-CD.

Chapter 6: Engine Test Data

The experimental data for the engine NO_x maps, steady-state, and transient gas tests are presented in this chapter. The objective of these experiments is to plot the spatial conversion profiles for ammonia, NO, and NO_2. This will determine the influence of each SCR reaction on the NO_x conversion process, and also assist in providing a baseline for validating the CFD model.

6.1 NO_x Mapping

Tab 6.1 displays NO_2: NO_x ratios under steady-state conditions, whilst Fig 6.1 presents the ratios in graphical form. The objectives of these experiments were to determine the DOC/DPF combination which provided the most desirable NO_2: NO_x ratio of approximately 0.5, and also investigate the effect of different engine loads on this ratio. Steady-state species concentrations can be found in Appendix 3.1 of this report.

DOC/DPF Configuration	Engine Load (bar)		
	3	6	9
1 DOC + DPF	0.04	0.28	0.35
2 DOCs + DPF	0.46	0.74	0.64
DPF + 1 DOC	0.05	0.43	0.39
DPF + 2 DOCs	0.49	0.82	0.75

Tab 6.1: NO_2: NO_x ratios for different DOC/DPF combinations and engine loads.

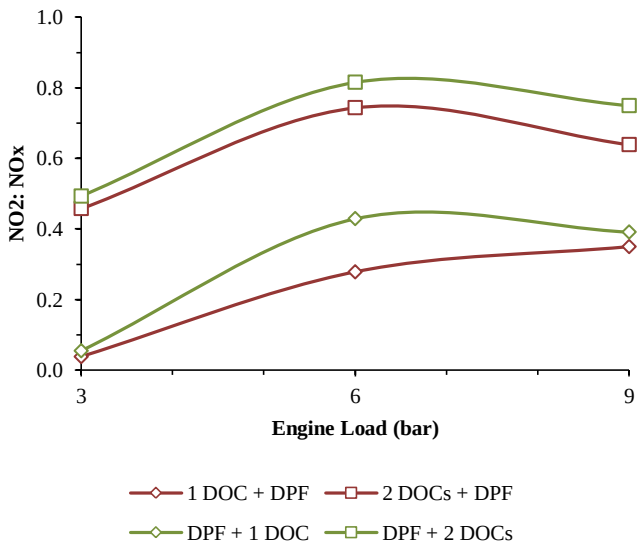

Fig 6.1: NO_2: NO_x ratios.

The data presented in Tab 6.1 and Fig 6.1 shows that the NO_2: NO_x ratio increases between the engine loads of 3 and 6 bar, and decreases slightly when the load reaches 9 bar. This trend is to be expected, because at lower engine loads, where the gas temperature is also lower, the activity of the oxidation

catalyst is reduced, whereas at 9 bar the NO_2: NO_x ratio begins to decrease due to thermodynamic equilibrium. Similar findings have been reported by Daimler-Chrysler in Section 2.3.4. [Chatterjee et al, 2008]

The NO_2: NO_x ratio also increases when the volume of the oxidation catalyst is doubled, this can be attributed to a lower space velocity, and hence higher residence times. When the DOC is placed upstream of the DPF, the results show a slight decrease in the NO_2: NO_x concentration, this suggests that some of the soot in the DPF is being regenerated by the NO_2.

6.2 Steady-State Spatial Conversion Profiles

The species conversion rates and the SCR bick lengths with their corresponding space velocities are presented in Tab 6.2 and Tab 6.3 respectively, whilst Fig 6.2 and Fig 6.3 plot the spatial species conversion profiles and the species concentrations respectively. An engine condition of 1500rpm and 6 bar BMEP were chosen in-line with previous work [Tamaldin et al, 2010]; this provided a mean exhaust gas temperature of about 213°C. Three NH_3: NO_x injection conditions were used, denoted by α_1, these were deficient ammonia (α_1 = 0.5), stoichiometric ammonia (α_1 = 1.0), and excess ammonia (α_1 = 1.5). The DOC/DPF configuration used was a single DOC downstream of the DPF, which provided an NO_2: NO_x ratio of 0.46. Oscillations on the graphs displayed in Fig 6.2 and Fig 6.3 are attributed to variations in exhaust conditions from test-to-test.

The steady-state species concentrations for these tests are located in Appendix 3.2 of this thesis.

Species	α_1	Brick Length (mm)								
		30	45.5	60	75.5	91	121	136.5	151	182
NO_x	0.5	39	46	42	47	46	45	45	48	47
	1.0	51	61	73	76	88	85	87	91	96
	1.5	50	61	72	76	87	87	89	94	97
NO	0.5	26	33	35	35	32	34	32	37	37
	1.0	35	43	57	60	76	74	78	83	86
	1.5	34	43	56	60	76	78	81	89	95
NO_2	0.5	53	61	50	62	59	60	63	60	57
	1.0	68	83	89	94	100	100	100	100	100
	1.5	69	84	90	95	99	100	100	100	100
NH_3	0.5	88	95	97	100	99	100	100	100	99
	1.0	52	59	79	78	93	94	95	99	100
	1.5	29	38	45	48	59	59	58	64	66

Tab 6.2: Species conversions (%) for different SCR brick lengths.

Brick Length (mm)	30	45.5	60	75.5	91	121	136.5	151	182
GHSV (hr^{-1})	531500	31800	265300	198800	159800	122100	106100	89000	80300

Tab 6.3: Catalyst lengths and gas hourly space velocities.

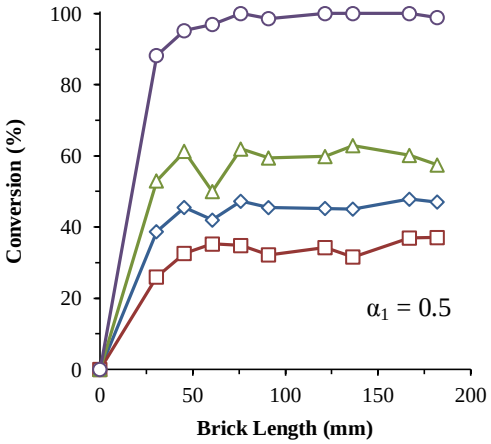

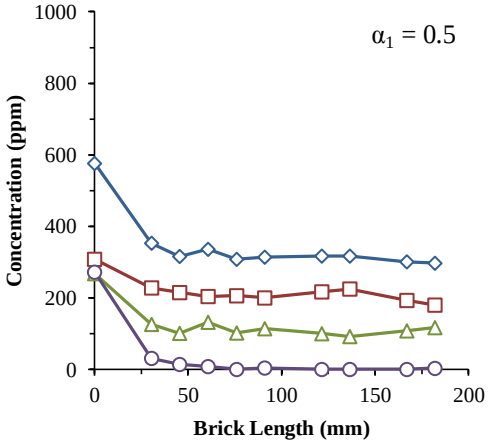

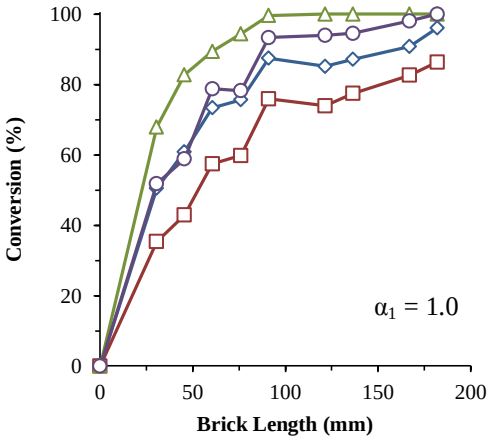

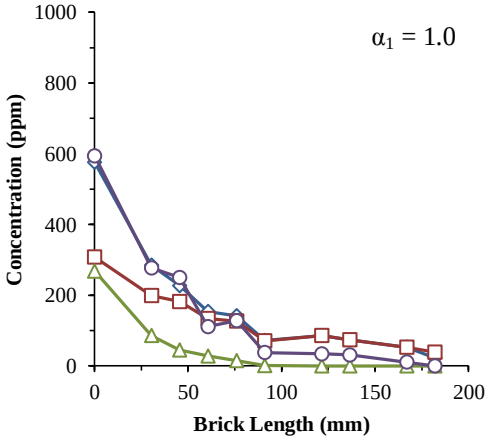

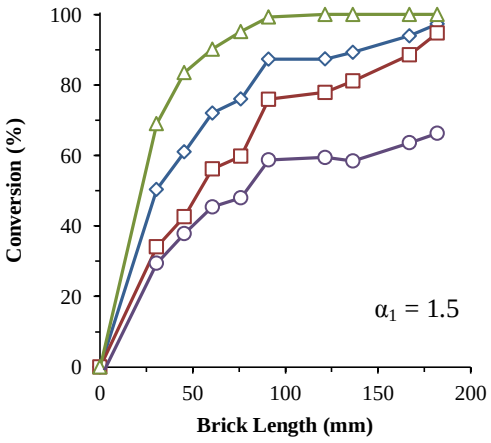

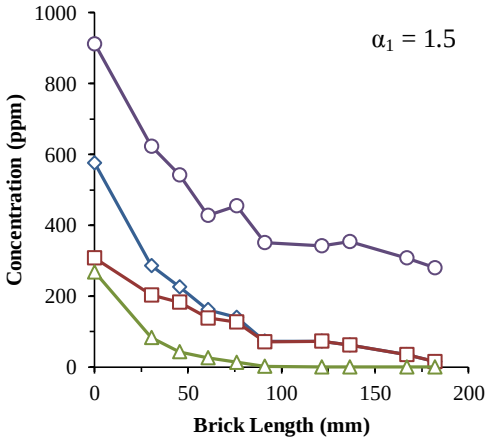

Fig 6.2: Spatial species conversion profiles for deficient, stoichiometric, and excess ammonia. NO_2: NO_x = 0.46, T = 213°C.

Fig 6.3: Spatial species concentration profiles for deficient, stoichiometric, and excess ammonia. NO_2: NO_x = 0.46, T = 213°C.

It is observed in Fig 6.2 and Fig 6.3 that the majority of the species conversion takes place just after the entrance of the brick, and the NO_2 decay is approximately double that of the NO. This was not to be

expected, and thus suggests that reactions involving NO_2 and ammonia appear to have an equal influence as well as the so called 'fast' SCR reaction, which was anticipated to be the dominant reaction at low temperatures. By about 90mm, it is observed that when α_1 = 1.0 and 1.5, nearly all of the NO_2 has disappeared. Such characteristics were also witnessed in previous work, where the exhaust gas temperature exceeded 300°C. [Tamaldin, 2010] Although the MEXA cannot detect N_2O, it was observed that equi-molar amounts of NO_2: NH_3 were consumed, thus suggesting that equation (46) acts simultaneously with the 'fast' SCR reaction just after the inlet.

When the case of α_1 = 1.0 is compared with the work undertaken by the University of Waterloo, a similar NO_x conversion profile is observed. [Hou et al, 2011] The rate of consumption and the amount of NO_x consumed at the end of the brick, however, is slightly less than that in Fig 6.2, despite an inlet gas temperature of 250°C, and the space velocity at the exit in the experiments in this thesis being higher by a magnitude of about 1.7. [Hou et al, 2011] One could attribute this difference to the catalysts analysed in the literature being aged before testing. [Hou et al, 2011] A comparison of the spatial NO and NO_2 concentration profiles also shows that in the literature, when the NO_2: NO_x ratio is about 0.5, the NO and NO_2 decay at approximately the same rate for temperatures between 180 and 300°C. [Hou et al, 2011] This was not observed in the experiments and could show the possible differences in the catalyst washcoat formulations.

6.3: Transient Tests

Ammonia storage tests were then undertaken for 30mm and 45.5mm long SCR bricks. These tests focussed on the injection of different amounts of ammonia under the engine condition of 1500rpm 6 bar BMEP for a certain period of time. Tab 6.4 describes the ammonia injection stages and their duration for each test, whilst Tab 6.4 shows the amount of ammonia stored on the catalyst surface. The transient plots are displayed in Figs 6.4 – 6.9. The objectives of these investigationswere to determine the adsorption capacity of the SCR catalyst, the steady-state response times, and to provide different inlet NO_2: NO_x ratios for the CFD model to be validated against.

Brick Length	NO_2: NO_x	α_1	Time	Inlet NH_3	Inlet NO	Inlet NO_2
mm			minutes	ppm	ppm	ppm
30	0.60	2.0	0 - 10	1134	220	336
		1.5	10 - 15	853		
		1.0	15 - 20	567		
		0.5	20 - 40	283		
		0.0	40 - 50	0		
45.5	0.64	2.0	0 - 10	1128	208	370
		1.5	10 - 15	845		
		1.0	15 - 25	563		
		0.5	25 - 40	282		
		0.0	40 - 50	0		
30	0.07	1.5	0 - 10	874	561	41
		1.0	10 - 15	602		
		0.5	15 - 25	291		
		0.0	25 - 40	0		

Tab 6.4: Inlet conditions and time intervals for transient experiments.

30mm Brick		45.5mm Brick	
NO_2: NO_x	Stored Ammonia (g)	NO_2: NO_x	Stored Ammonia (g)
0.60	0.681	0.64	0.791
0.07	0.632	-	-

Tab 6.5: Ammonia storage capacity for 30mm and 50mm SCR catalyst bricks. The amount of ammonia adsorbed by the SCR brick is calculated via the methodology described in Appendix 3.5 of this report.

It is observed in Tab 6.4 that when the two cases involving the 30mm bricks are compared, there is relatively only a small difference between the two levels of stored ammonia, ~0.05g. This suggests that the influence of the NO_2: NO_x ratio, and the amount of ammonia present in the exhaust has a minimal effect on the storage capacity of the catalyst.

The transient profiles for a single DOC located downstream of the DPF are plotted in Figs 6.4 – 6.7 and Figs 6.8 – 6.9 for 30mm and 45.5mm SCR bricks respectively. For these experiments, an NO_2: NO_x ratio of 0.6 was observed; this is an increase when compared with the ratio of 0.46 in Section 6.2, and could be attributed to the engine being run at full load, which possibly increased the NO oxidation efficency of the DOC due to the exhaust gas temperatures being at approximately 450°C. The amount of ammonia injected into the exhaust corresponds to $\alpha_1 = 2.0$ for 10 minutes, $\alpha_1 = 1.5$ for 5 minutes, $\alpha_1 = 1.0$ for 5 minutes, $\alpha_1 = 0.5$ for 20 minutes, and $\alpha_1 = 0.0$ for 15 minutes.

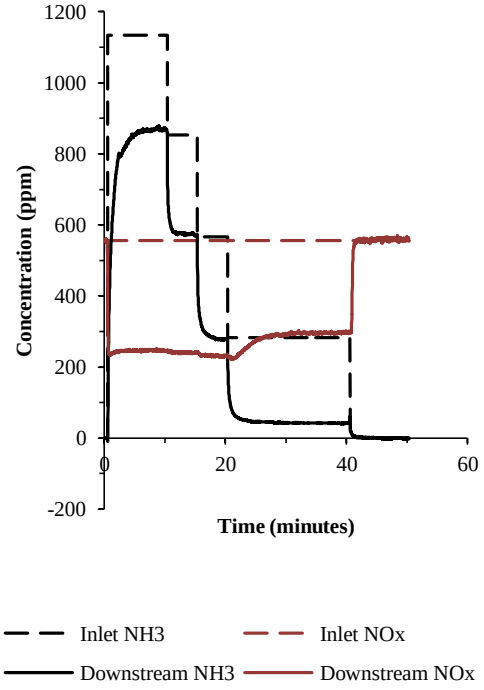

Fig 6.4: Transient experimental NO_x and ammonia concentration profiles for a brick length = 30mm and NO_2: NO_x = 0.60.

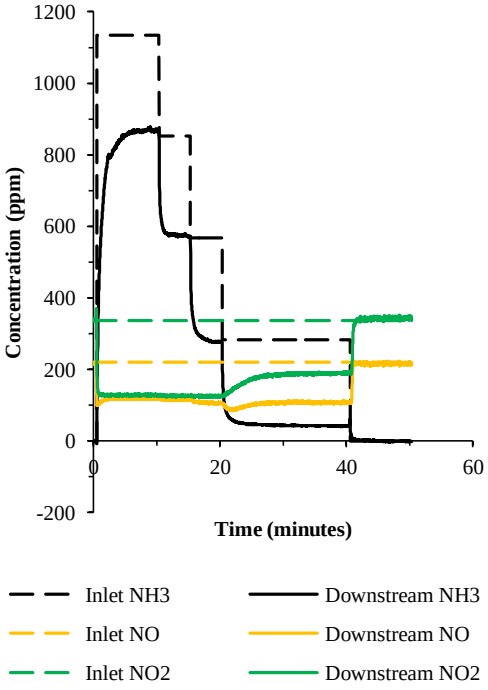

Fig 6.5: Transient experimental NO, NO_2, and ammonia concentration profiles for a brick length of 30mm, and NO_2: NO_x = 0.60.

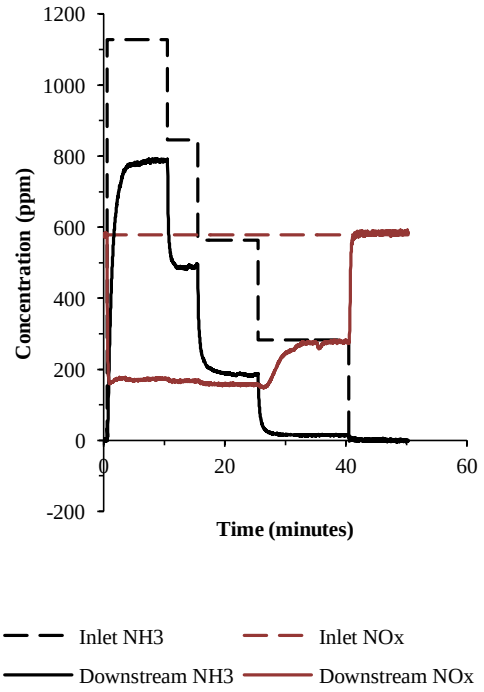

Fig 6.6: Transient experimental NO_x and ammonia concentration profiles for a brick length = 45.5mm and NO_2: NO_x = 0.64.

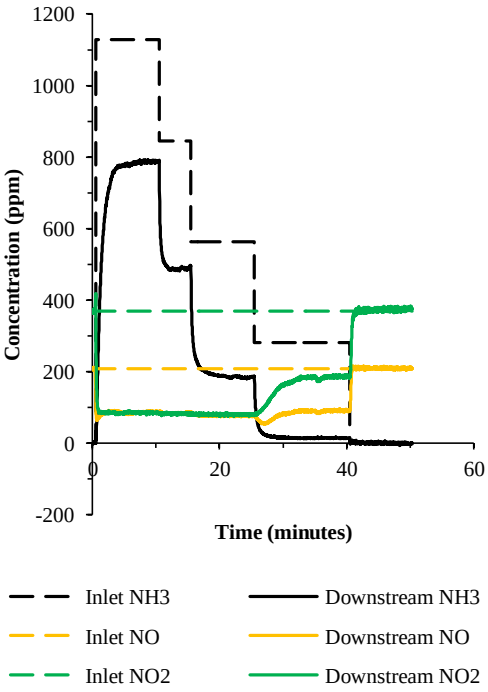

Fig 6.7: Transient experimental NO, NO_2, and ammonia concentration profiles for a brick length of 45.5mm, and NO_2: NO_x = 0.64.

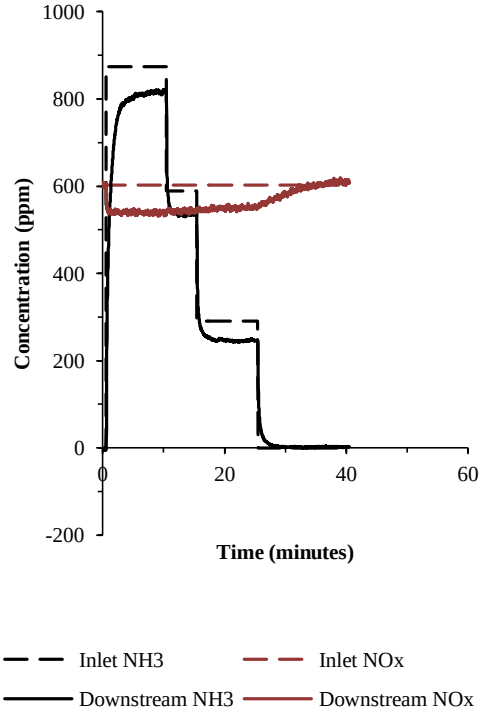

Fig 6.8: Transient experimental NO_x and ammonia concentration profiles for a brick length = 30mm and NO_2: NO_x = 0.07.

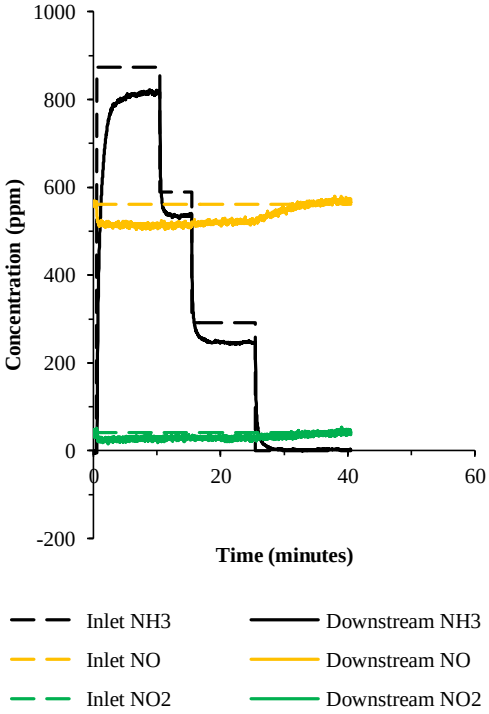

Fig 6.9: Transient experimental NO, NO_2, and ammonia concentration profiles for a brick length of 30mm, and NO_2: NO_x = 0.07.

The transient ammonia response as described in Fig 6.4 and Fig 6.5 is observed to be noticeably longer than that for the NO_x when α_1 = 2.0; this was to be expected due to ammonia was being adsorbed on the catalyst surface. When α is then changed to 1.5 after about 10 minutes, ammonia desorption is seen to take place for about 2 minutes. The ammonia desorption times when α_1 = 1.0 and 0.5 are approximately 3 and 8 minutes respectively. It is also observed that when α_1 is decreased from 1.0 to 0.5, the NO_x response time is considerably slower than that of the ammonia, which suggests that some the excess ammonia on the catalyst surface is reacting with the NO_x.

It can be seen that although more NO_2 is converted than NO, the response of both species is remarkably similar after about 30 seconds, 20 minutes, and 40 minutes. This could imply that both the 'fast' and 'NO_2 + NH_3' reactions have equal influence under transient conditions for varying levels of α as they do under steady-state. A slight dip in the NO concentration is also observed 20 minutes into the test.

Fig 6.6 and Fig 6.7 plot the transient logs for a 45.5mm long SCR bricks. The transient response time for ammonia for the case of α_1 = 2.0 is about 6 minutes, however when α_1 = 1.5 and 1.0, the response time is approximately 2 and 6 minutes respectively, when the α_1 = 0.5 were investigated the ammonia transient response for a brick length of 50mm was shown to be around 4 minutes. It is observed that the 30mm long brick, the ammonia transient response times are greater when compared with the 30mm

brick; this can be attributed to more ammonia being able to be stored on the 50mm brick than on the 30mm one.

It can be seen that when ammonia is first injected into the exhaust after about 30 seconds, the transient response for NO and NO_2 is quite similar; this was also observed for the 30mm brick. When α is changed from 1.0 to 0.5 the NO_2 is seen to take an extra 2 minutes to reach its steady-state value when compared with the NO. This could suggest a slight preference towards the 'NO_2 + NH_3' reactions, something that is not seen with the 30mm brick.

An interesting observation is seen in Fig 6.4 and Fig 6.6 in which the downstream NO_x increases as the amount of ammonia injected decreases up to when α_1 = 1.0. The cause of this is likely to be ammonia inhibition of the 'fast' SCR reaction, in which the ammonia already present on the catalyst washcoat can cause interference with one of the intermediate stages of the 'fast' SCR by forming NH_4NO_3 at low temperatures. [Grossale et al, 2010] The overall effect witnessed here, however, is quite small because of the exhaust gas temperatures being higher than the decomposition temperature of ammonium nitrate, more investigation would be required at exhaust gas temperatures below 200°C.

The transient logs for an exhaust system without an oxidation catalyst are plotted in Fig 6.8 and Fig 6.9 for the 30mm brick. The small amount of upstream NO_2 observed was likely to have been formed via the combustion processes inside the engine. One observes that the ammonia takes approximately 7 minutes to reach steady-state when α_1 = 1.5, which can be attributed to ammonia adsorption. The ammonia readings take about 1 minute to reach steady-state for the case of α_1 = 1.0. The transient response time is approximately 4 minutes when α_1 = 0.5. Ammonia slippage is observed for a further 3 minutes when the gas was turned off.

It can be seen that the amount of NO_x converted by the ammonia under all conditions is very small, this is to be expected as the vast majority of the NO_x is NO, and the 'standard' SCR reaction involving NO, ammonia, and oxygen has a poor activity at low exhaust gas temperatures. The NO and NO_2 then takes a further 10 minutes to recover back to their inlet values. An interesting observation is seen in that more NO has been converted than NO_2.

6.4 Test Repeatability

Fig 6.10 and Fig 6.12 plot the upstream and downstream NO_x and ammonia concentrations as well as the upstream SCR temperatures. Fig 6.12 plots the species conversion ratios with respect ammonia for NO_x, NO, and NO_2 for the experiments discussed in Section 6.2, the CFd analyses were included for reference purposes. It was assumed that as the exhaust gas temperatures are quite low, the effect of the 'slow' SCR reaction is negligible.

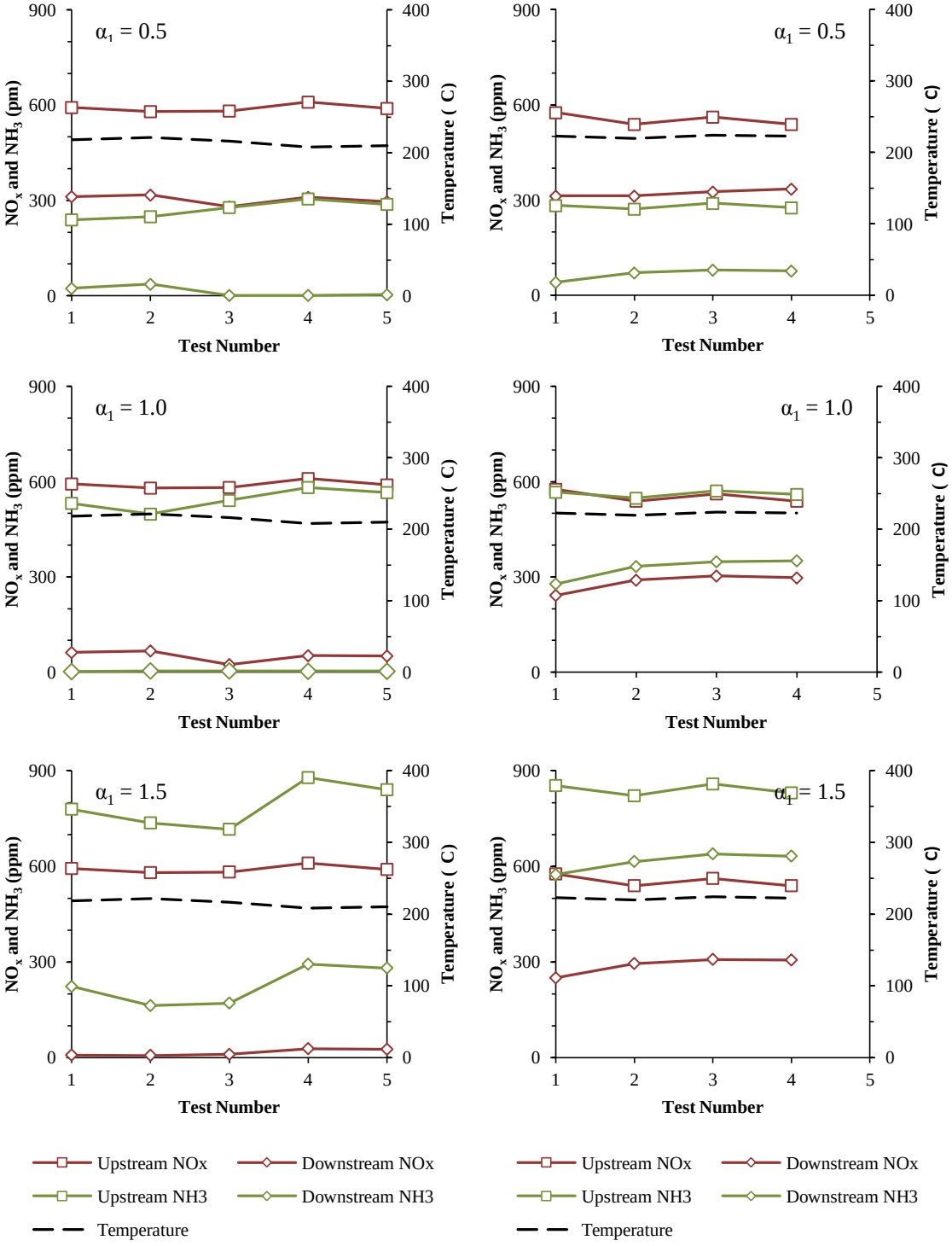

Fig 6.10: Steady-state upstream and downstream NO_x and NH_3 concentrations for five different tests using a 182mm SCR brick.

Fig 6.11: Steady-state upstream and downstream NO_x and NH_3 concentrations for four different tests using a 30mm SCR brick.

It is observed in Fig 6.10 and Fig 6.11 that adequate levels of repeatability for a 182mm long SCR brick are obtained with the maximum variation in the upstream NO_x equal to 36ppm. Consistency for the gas temperatures and the NO_x levels was attempted by controlling the amount of water entering the

intercooler via closed-loop control based on the engine inlet temperature, although reasonable levels of control were achieved via this method, it is recommended that an air-conditioning unit that controls the air engine intake pressure, temperature, and humidity be installed in the test cell.

The NO_x and ammonia conversion rates can also be compared in Fig 6.10 and Fig 6.11. It can be seen that approximately equi-molar amounts of NO_x and ammonia are consumed for the 182mm brick, for all values of α_1 and for each test, however, for the 30mm brick, it can be seen that more NO_x: NH_3 is consumed; this suggests that the ammonia scrubbers are unable to adsorb all of the ammonia, as there are no published kinetics that describe a reaction where more NO_x: NH_3 is concumed. The ratio of consumed NO_x: NH_3 is also observed to increase as more tests were undertaken on the 30mm brick, therefore for greater repeatability one would be required to replace the ammonia scrubbers at more regular intervals between tests, if short bricks or experiments involving high levels of ammonia are to be undertaken.

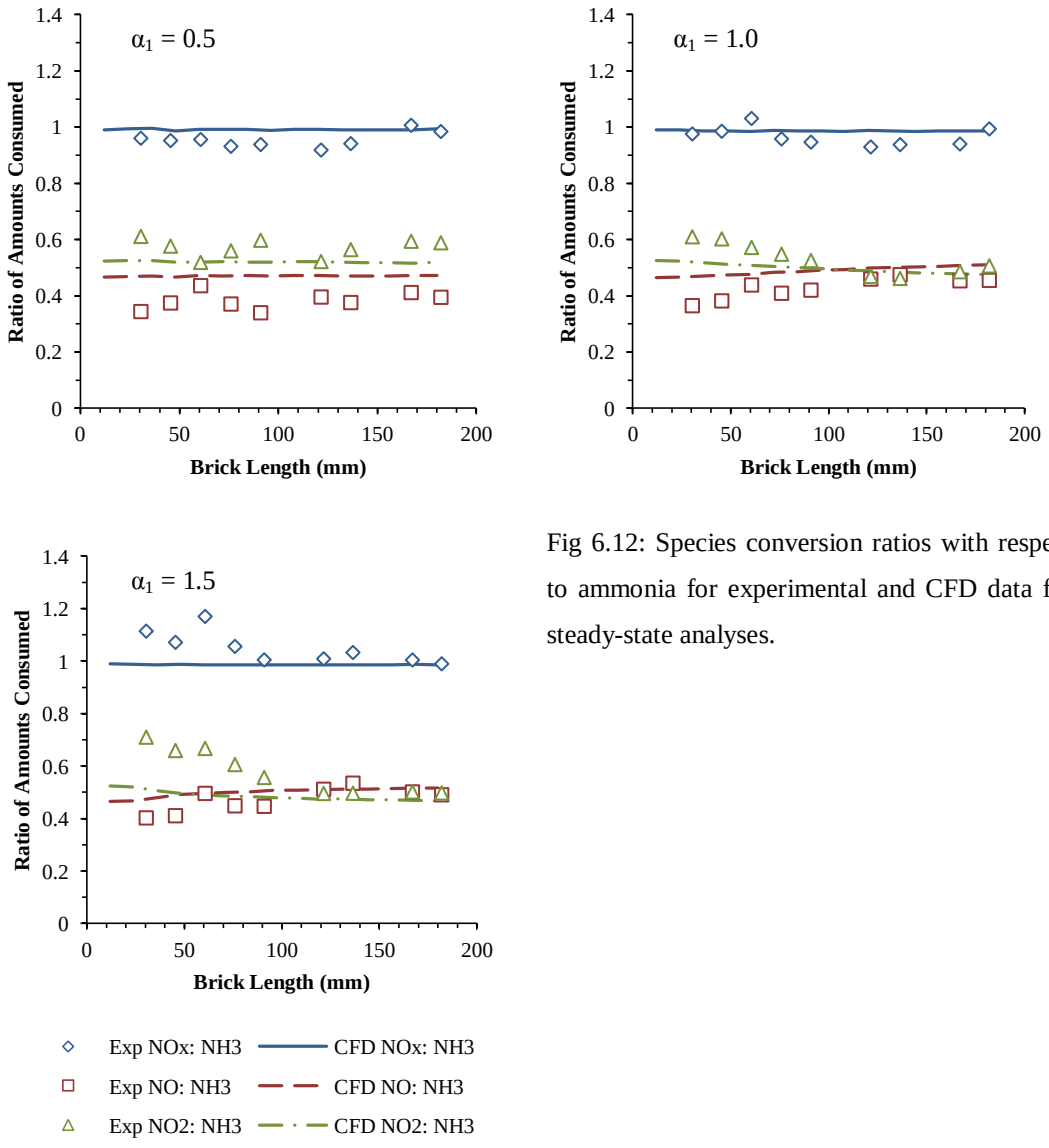

Fig 6.12: Species conversion ratios with respect to ammonia for experimental and CFD data for steady-state analyses.

It can be seen in Fig 6.12 that, when α_1 = 0.5 and 1.0, the NO_x: NH_3 consumption ratio is approximately 1.0. However, for the case of α_1 = 1.5, it is noticed that more NO_x than ammonia is consumed for the first 91mm; this could imply that for ammonia concentrations above approximately 500ppm, the ammonia scrubbers aren't able to completely absorb all of the ammonia. A longer catalyst brick would be required for more aggressive dosing strategies to convert all of the NO_x, which would help negotiate this problem.

It was also noticed in the periodic logs that when the MEXA was positioned upstream of the SCR and ammonia was injected, the NO_x level dropped slightly. The decrease in upstream NO_x increased with respect to the inlet ammonia; this is presented in Appendix 3.6 of this thesis. A similar effect has been reported in literature, where the decline in NO_x was attributed to the NO_2 reacting with ammonia and water in the exhaust to form NH_4NO_3 [Luo et al, 2010], however, an FTIR analyser was used [Luo et al, 2010], which due to is mechanism of analysis, does not have the same issues with large levels of ammonia as the MEXA.

Chapter 7: CFD Base Case Model Validation

7.1 Steady-State Analysis

The steady-state spatial conversion profiles undertaken using CFD for the conditions described in the engine tests are presented in this section. Data obtained from the CFD simulations are compared directly against the experimental data for NO_x, NO, NO_2, and ammonia. Input parameters used for the CFD simulations are described in Tab 7.1, the species and temperatures are based on the measurements obtained from the instrumentation module located upstream of the SCR on the exhaust rig:

NO_x: NO_2	Temperature	Mass Flow Rate	NO	NO_2	NH_3	NH_3: NO_x	O_2
	°C	$g.s^{-1}$	ppm	ppm	ppm		MF
0.46	211.0	31.1	323	275	294 603 906	0.49 1.01 1.52	0.1348

Tab 7.1: CFD input parameters.

The CFD and experimental spatial NO_x, NO, NO_2, and ammonia conversion profiles are plotted in Figs 7.1, 7.2, 7.3, and 7.4 respectively. The ammonia injection conditions are denoted on each graph by symbol α.

The value of Ω was varied as the number of available reaction sites on the experimental catalyst was unknown, as discussed in Section 5.8.

The NO_x conversion profiles in Fig 7.1 show that for all values of Ω investigated in this study, the model under-predicts the amount of NO_x converted just after the inlet when $\alpha_1 = 0.5$. It can be seen that a values of $\Omega = 300$mol-sites.m^{-3} provide the most adequate agreement for the entire length of the brick for the case of $\alpha_1 = 1.0$, and the best predictions by the model are provided when Ω is decreased to 200mol-sites.m^{-3} when $\alpha_1 = 1.5$.

It is observed that in Fig 7.2, the model over-predicts the amount of NO converted towards the end of the brick when $\alpha_1 = 0.5$, although agreement with the experimental data is more satisfactory just after the inlet. The model is observed to over-estimate the amount of NO consumed for values of $\Omega >$ 200mol-sites.m^{-3} when $\alpha_1 = 1.0$ and 1.5.

Fig 7.3 shows that the model underestimates the amount of NO_2 consumed up to the end of the brick for the case of $\alpha_1 = 0.5$. Values of $400 < \Omega < 500$mol-sites.m^{-3} provide the most adequate agreement with the experimental data for the whole SCR brick when $\alpha_1 = 1.0$, whilst the amount of NO_2 consumed for the case of $\alpha_1 = 1.5$ is under predicted when $\Omega = 200$mol-sites.m^{-3}, but over-estimated for the other values.

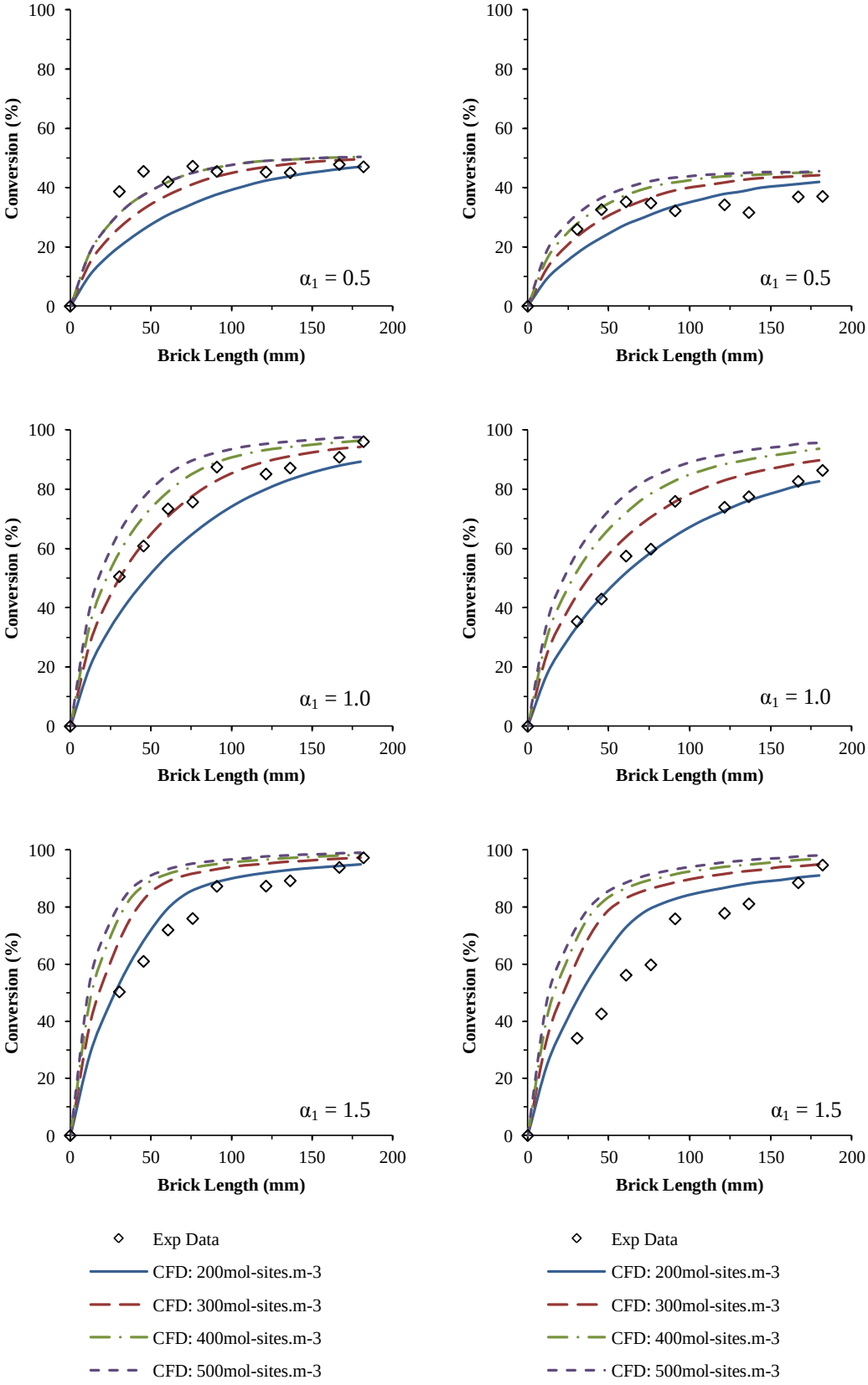

Fig 7.1: CFD and experimental spatial NO_x conversion profiles.

Fig 7.2: CFD and experimental spatial NO conversion profiles.

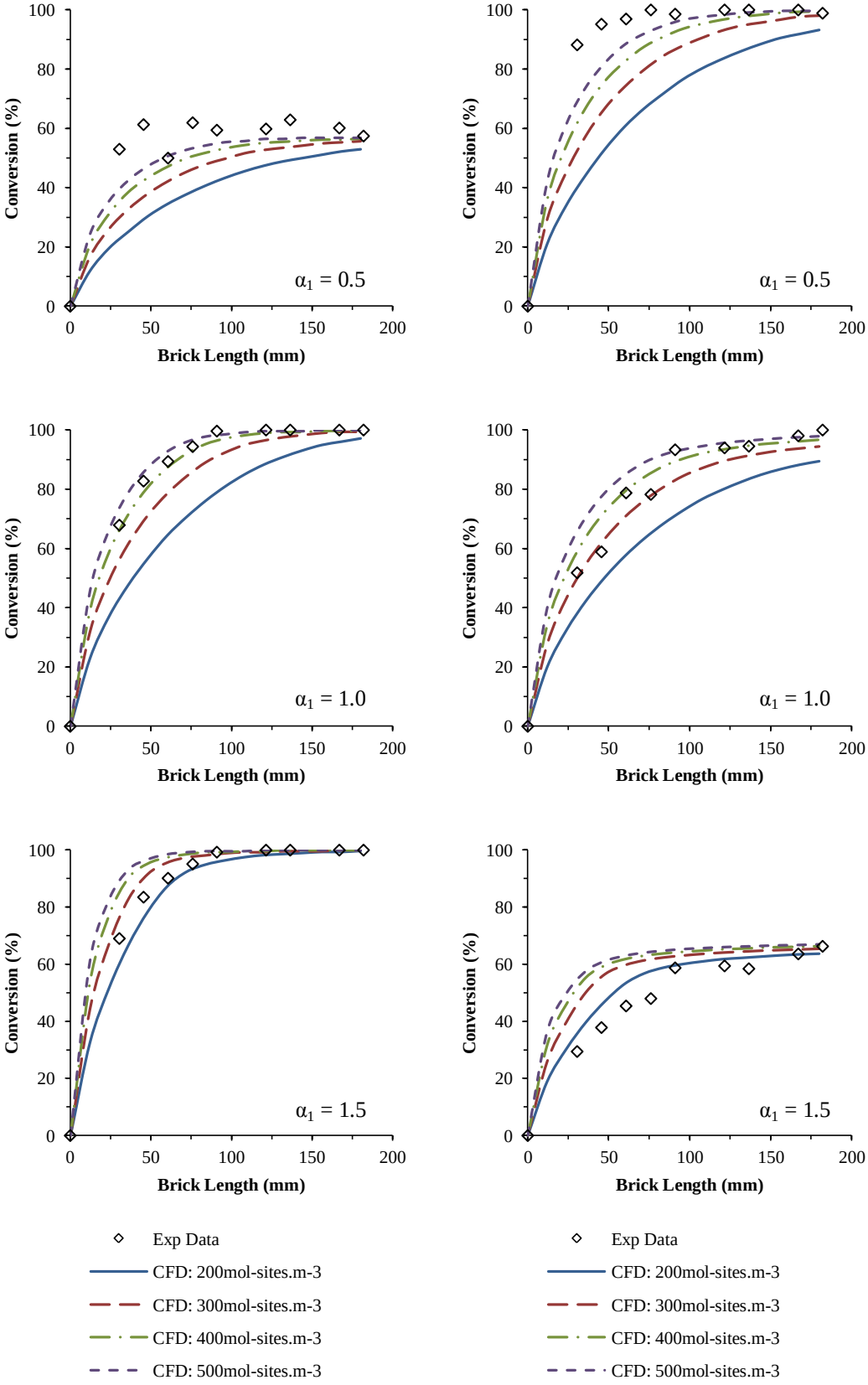

Fig 7.3: CFD and experimental spatial NO_2 conversion profiles.

Fig 7.4: CFD and experimental spatial NH_3 conversion profiles.

The spatial ammonia conversion profiles plotted in Fig 7.4 show that when $\alpha_1 = 0.5$, the model shows a significant under-prediction of ammonia consumption just after the SCR inlet for all CFD cases. It is observed when $\alpha_1 = 1.0$, however, that the most reasonable agreement is achieved when Ω lies between 300 and 400mol-sites.m^{-3}. The agreement between the simulations and the experiments for the first 91mm is quite poor for the case of $\alpha_1 = 1.5$.

7.2: Transient Analysis

7.2.1: Transient Profiles for 30mm Brick, NO_2: NO_x = 0.60

Figs 7.5, 7.6, 7.7, and 7.8 plot the transient downstream species concentrations for values of Ω = 200, 300, 400, and 500mol-sites.m^{-3} respectively. The NO_2: NO_x ratio used for these analyses was approximately 0.64; this provides a different condition for comparison of the model with the experimental data.

An input value of Ω = 200mol-sites.m^{-3} is observed to provide the closest steady-state agreement between the simulations and the experiments when $\alpha_1 = 2.0$. It is observed that as α_1 is decreased from 2.0 to 1.5, the model over-predicts and under-predicts the amount of NO_x measured for 200 and 300mol-sites.m^{-3} respectively; this suggests that for the model to adequately predict the engine test data, a value of Ω between 200 and 300mol-sites.m^{-3} is required. When α_1 is then reduced to 1.0, it can be seen that an input value of 500mol-sites.m^{-3} is seen to be necessary for accurate representation of the experimental data. The model is shown to overestimate the levels of NO_x present in the exhaust at 30mm for all values of Ω for the case of $\alpha_1 = 0.5$; this is consistent with the steady-state analyses discussed in Section 7.1.

It is noticed that the model over-predicts the NO consumption when $\alpha_1 = 2.0$ for all values of Ω investigated in this study. The simulations are shown to provide a good agreement with the experimental data for values of Ω equivalent to 200 and 300mol-sites.m^{-3} respectively for the cases of $\alpha_1 = 2.5$ and 1.0. It is then observed that when α_1 is decreased to 0.5, the model underestimates the NO consumption for the 30mm brick.

It is observed the best agreement between the CFD simulations and the experimental data for NO_2 is achieved for a value of Ω = 300mol-sites.m^{-3} when $\alpha_1 = 2.0$ and 1.5. When α_1 is decreased to 1.0 it can be seen that The model is seen to predict the steady-state NO_2 quite well, when Ω = 500mol-sites.m^{-3} when α is decreased to 1.0, and for the case of $\alpha_1 = 0.5$, it is noticed that the simulations overestimate the amount of NO_2 present at 30mm for all values of Ω. The transient NO_2 profile at $\alpha_1 = 0.5$ is also observed to be unrepresentative of the experimental data as the steady-state response time from the experiments is noticeably slower.

The transient ammonia concentration profiles are plotted on all graphs in this section. One can see that for the case of $\alpha_1 = 2.0$ and for all values of Ω, the model is unable to accurately predict both the

steady-state ammonia concentrations, and the transient profile. An input value of 200mol-sites.m^{-3}, provides a very good agreement for the steady-state predictions, and the transient profiles when α_1 = 1.5. It is noticed that when α_1 is decreased to 1.0 adequate agreement with the experiments is achieved for values of Ω equal to 300 and 400mol-sites.m^{-3} with the steady-state response time being slight under-predicted by the CFD model. The model over-predicts the ammonia levels for a 30mm brick for all values of Ω for the case of α_1 = 0.5.

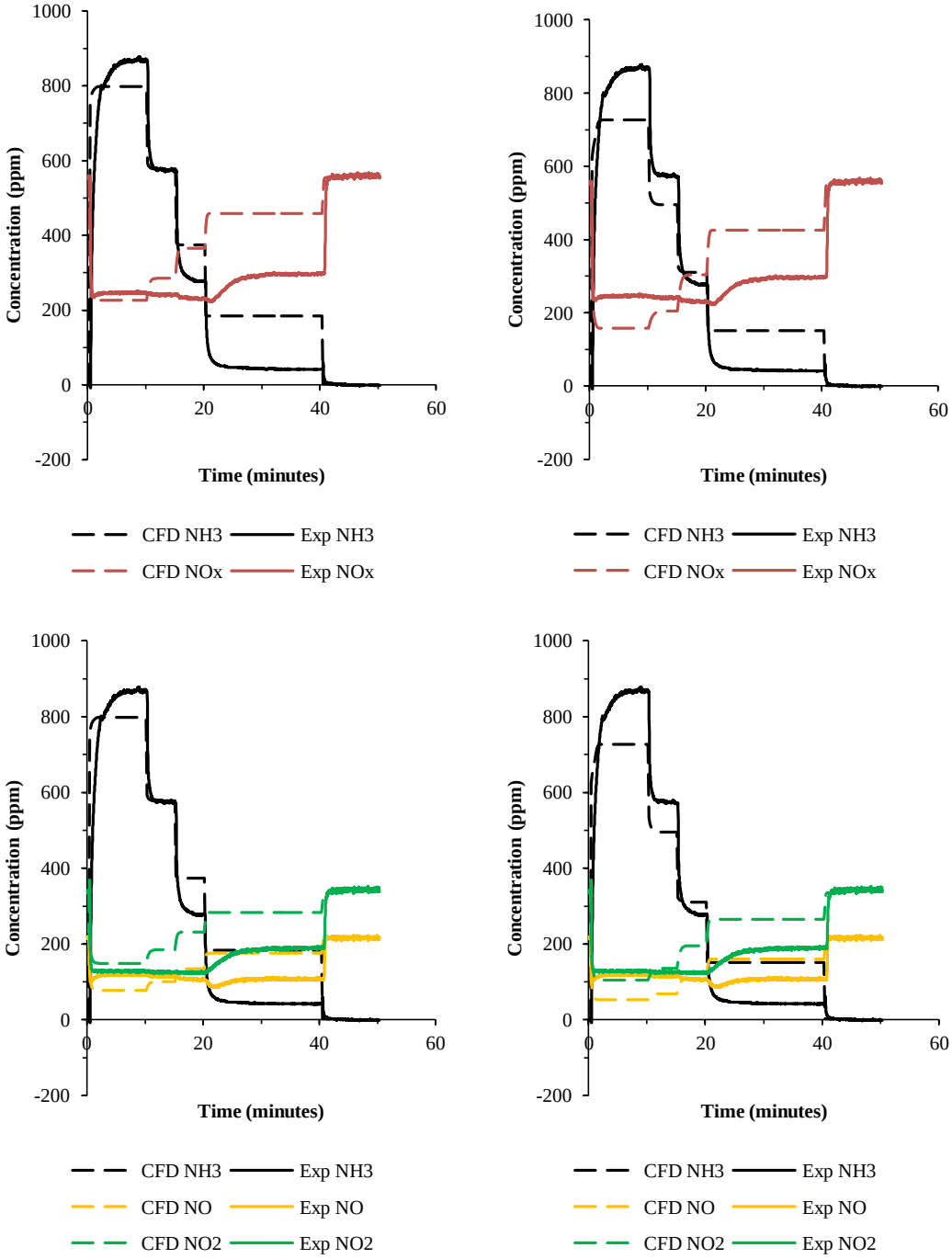

Fig 7.5: CFD and experimental transient concentration profiles for a value of Ω = 200mol-sites.m^{-3}. Brick length = 30mm, NO_2: NO_x = 0.60.

Fig 7.6: CFD and experimental transient concentration profiles for a value of Ω = 300mol-sites.m^{-3}. Brick length = 30mm, NO_2: NO_x = 0.60.

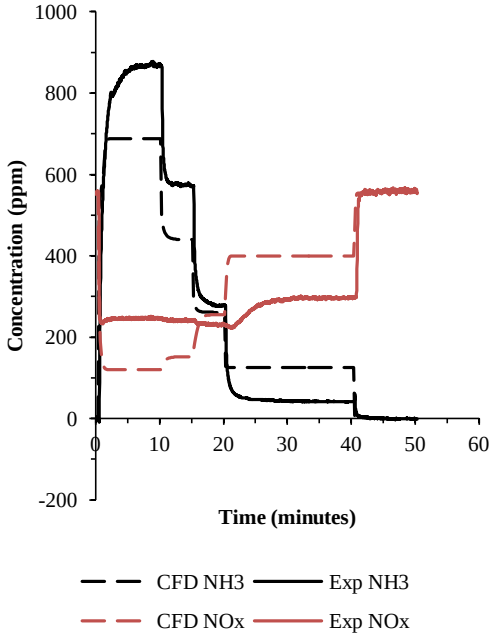

Fig 7.7: CFD and experimental transient concentration profiles for a value of Ω = 400mol-sites.m^{-3}. Brick length = 30mm, NO_2: NO_x = 0.60.

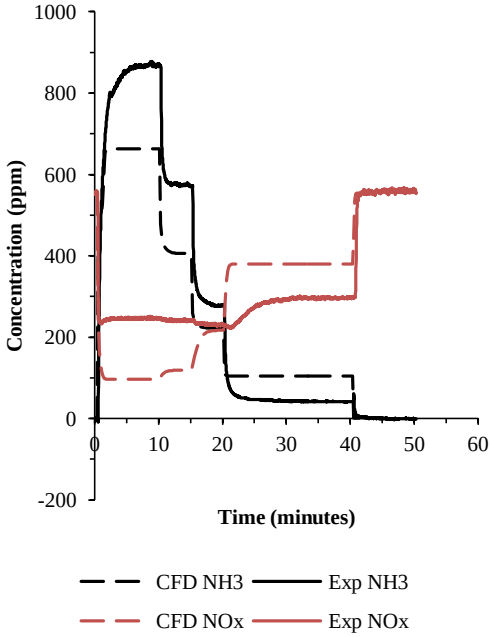

Fig 7.8: CFD and experimental transient concentration profiles for a value of Ω = 500mol-sites.m^{-3}. Brick length = 30mm, NO_2: NO_x = 0.60.

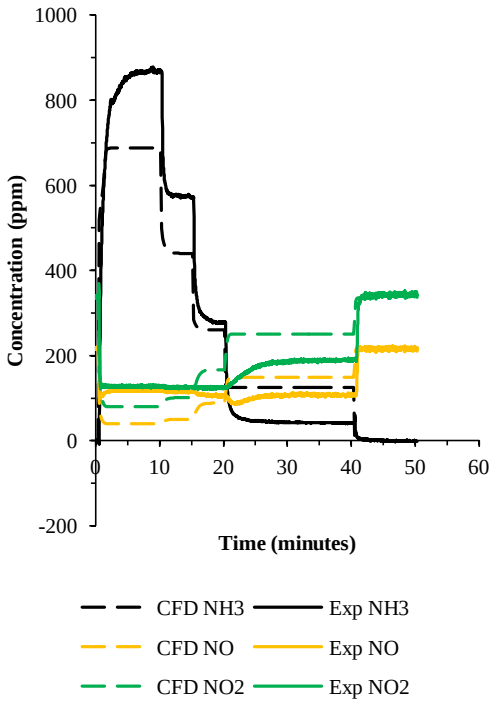

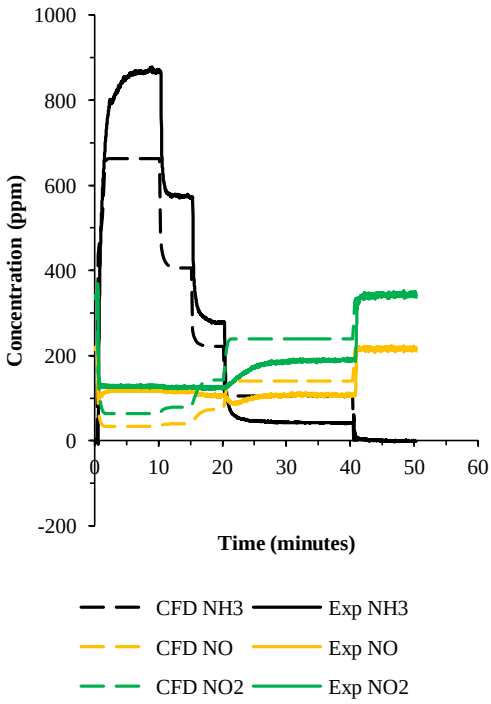

7.2.2: Transient Profiles for 45.5mm Brick, NO_2: NO_x = 0.64

Figs 7.9, 7.10, 7.11, and 7.12 plot the transient species concentration for values of Ω = 200, 300, 400, and 500mol-sites.m^{-3} respectively. The NO_2: NO_x ratio used for these analyses was approximately 0.60.

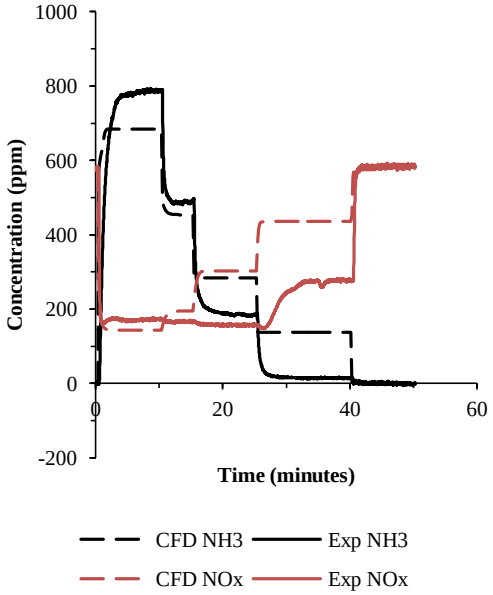

Fig 7.9: CFD and experimental transient concentration profiles for a value of Ω = 200mol-sites.m^{-3}. Brick length = 45.5mm, , NO_2: NO_x = 0.64.

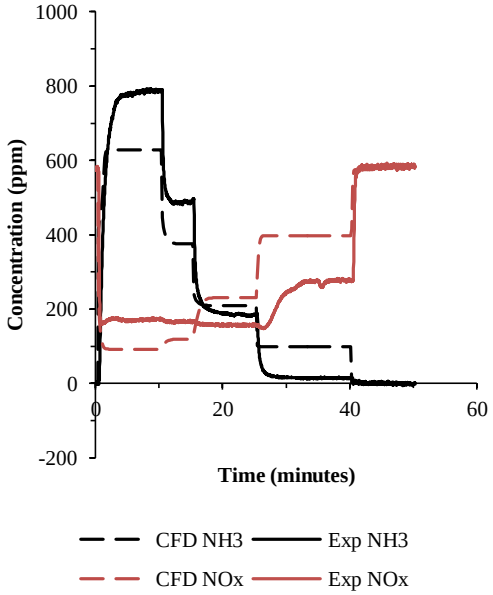

Fig 7.10: CFD and experimental transient concentration profiles for a value of Ω = 300mol-sites.m^{-3}. Brick length = 45.5mm, NO_2: NO_x = 0.64.

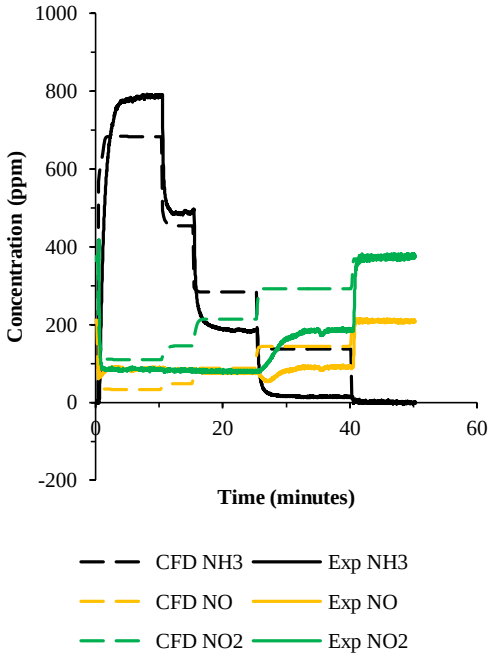

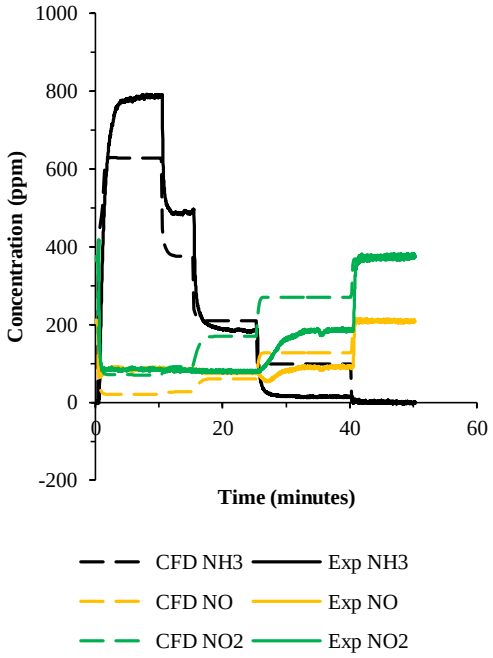

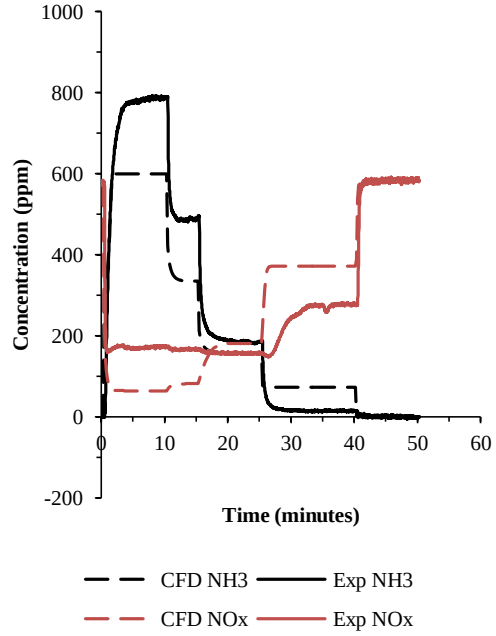

Fig 7.11: CFD and experimental transient concentration profiles for a value of Ω = 400mol-sites.m^{-3}. Brick length = 45.5mm, NO_2: NO_x = 0.64.

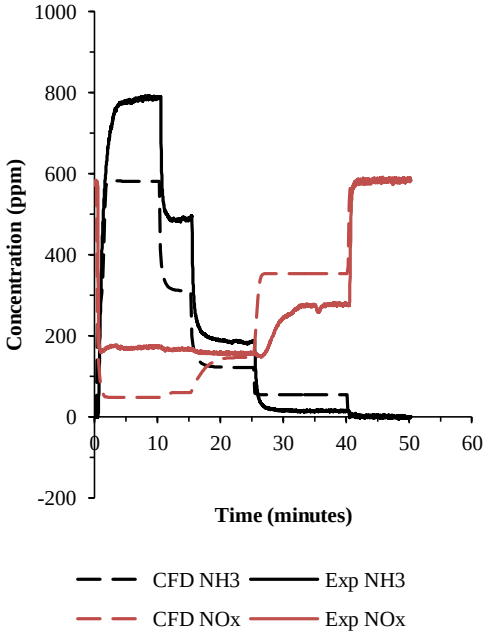

Fig 7.12: CFD and experimental transient concentration profiles for a value of Ω = 500mol-sites.m^{-3}. Brick length = 45.5mm, NO_2: NO_x = 0.64.

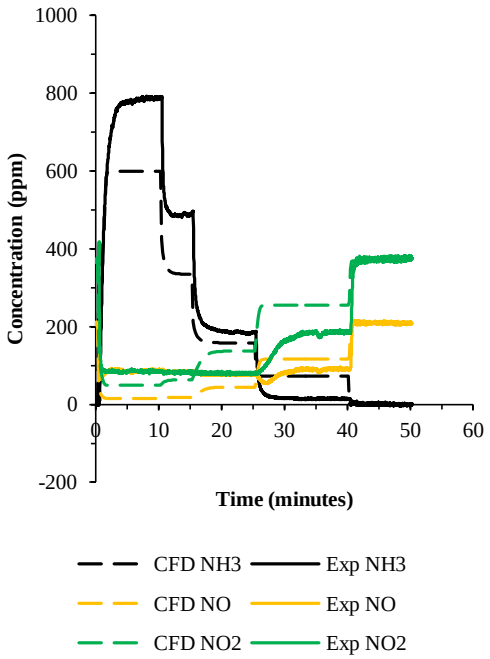

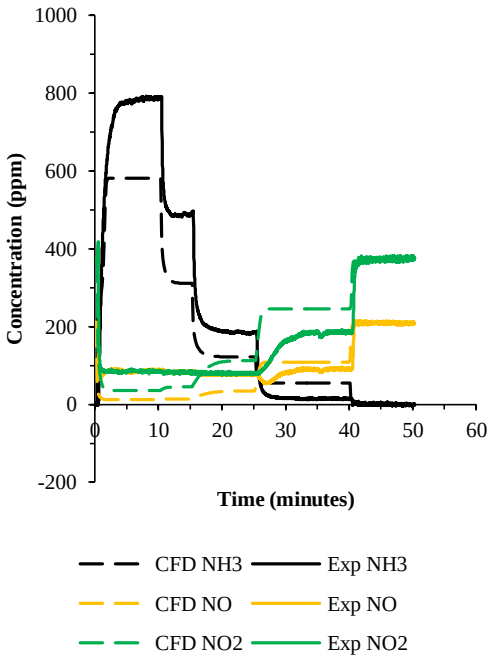

It is observed that for the cases of α_1 = 2.0 and 1.5, an input value of 200mol-sites.m^{-3} provides adequate agreement with the experimental data for the transient NO_x profile with an error of approximately 40ppm once the steady-state concentrations are reached. Optimal agreement can be seen for a value of Ω = 500mol-sites.m^{-3} when α_1 = 1.0. The CFD model over-predicts the amount of NO_x

in the exhaust for all values of Ω when α_1 is decreased to 0.5. The steady-state response time is also seen to be noticeably quicker in the model than in the experiments.

When α_1 = 2.0 and 1.5, it can be seen that the model underestimates the levels of NO in the exhaust for all values of Ω, however, when α_1 is decreased to 1.0 it can be seen that values of $200 \leq \Omega \leq 300$mol-sites.m^{-3} provide a strong correlation with the engine test data. As α_1 is further decreased to 0.5, it is noticed that a value of Ω = 500mol-sites.m^{-3} provides a good agreement with the experiments, although the desorption time is noticeably quicker in the CFD model.

The model is observed to predict the experimental NO_2 concentrations very well for a value of Ω equivalent to 300mol-sites.m^{-3} when α_1 = 2.0 and 1.5. It can then be seen that as α_1 is decreased from 1.5 to 1.0 the model begins to over-predict the downstream levels of NO_2 for all values of Ω investigated. The rate of increase of NO_2 from when the α_1 is decreased from 1.0 to 0.5 is also shown to be overestimated by the model.

The transient ammonia profiles are plotted on all figures. It is noticed that although the CFD simulations under-predict the steady state values of ammonia, the adsorption profiles, however, are seen to match considerably better than for the 30mm brick when ammonia is first injected. Adequate agreement is observed between the model and the experiments when α_1 is decreased from 2.0 to 1.5 for a value of Ω = 200mol-sites.m^{-3}, with the model predicting the transient decay profile quite well. As α_1 is decreased to 1.0. Reasonable agreement is witnessed for when $300 \leq \Omega \leq 400$mol-sites.m^{-3} for a value of α_1 equal to 1.0, however, when α_1 = 0.5, the model is unable to successfully replicate the downstream ammonia desorption profile.

7.2.3: Transient Profiles for 30mm Brick, NO_2: NO_x = 0.07

Figs 7.13, 7.14, 7.15, and 7.16 plot the transient species concentration for values of Ω = 200, 300, 400, and 500mol-sites.m^{-3} respectively. The NO_2: NO_x ratio used for these analyses was approximately 0.07.

It can be seen that when α_1 = 1.5 and 1.0, the agreement for the NO_x concentrations between the CFD model and the experimental data for all values of Ω and the experiments is very poor, however, there is a noticeable improvement in the predictions made by the CFD model for the case of α_1 = 0.5, when Ω = 200mol-sites.m^{-3}. One notices that the NO_x recovery time is considerably faster for the simulations than for the experiments when the ammonia gas is switched off.

A similar pattern in the transient profiles for the NO profiles is observed when compared with the NO_x profiles; this is to be expected as 93% of the total NO_x in the exhaust is made up of NO. It can be seen that the recovery time for the model is also less than in the experiments when the gas is turned off.

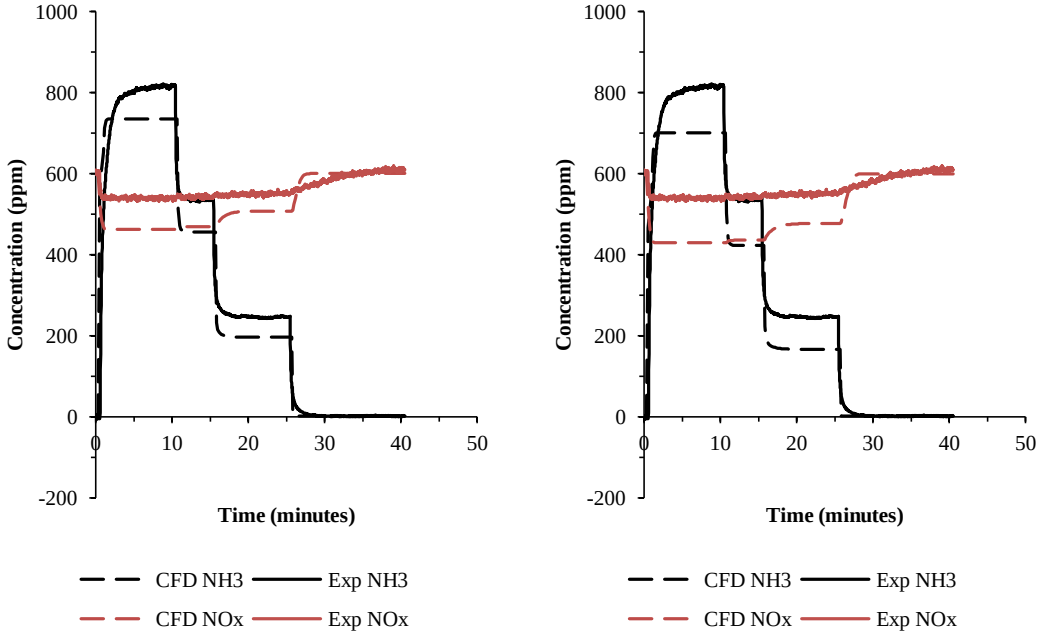

Fig 7.13: CFD and experimental transient concentration profiles for a value of Ω = 200mol-sites.m^{-3}. Brick length = 30mm, NO_2: NO_x = 0.07

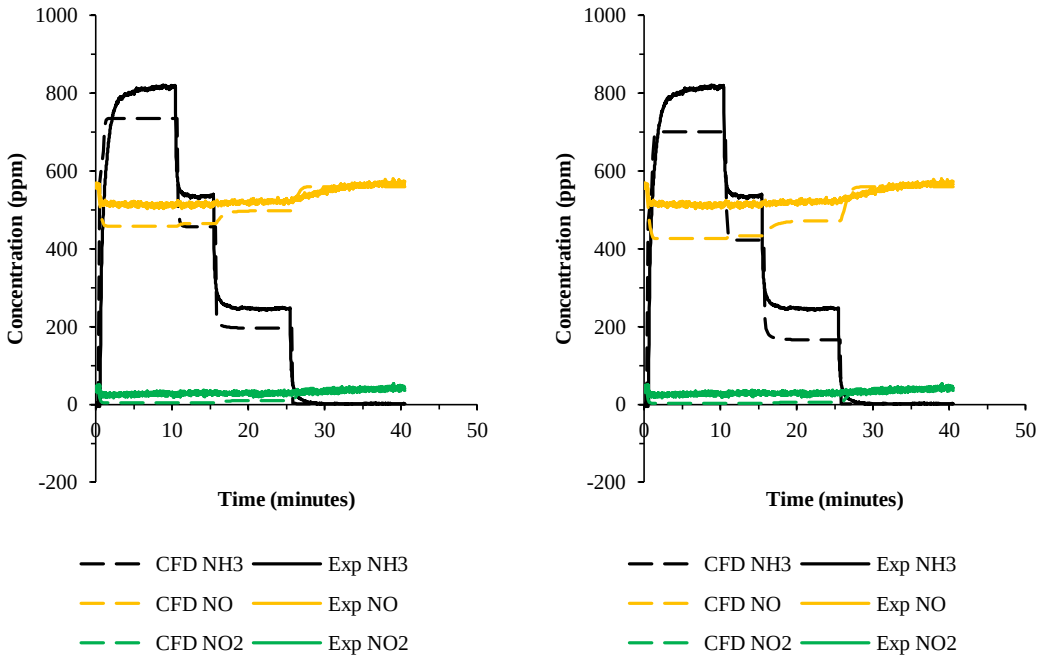

Fig 7.14: CFD and experimental transient concentration profiles for a value of Ω = 300mol-sites.m^{-3}. Brick length = 30mm, , NO_2: NO_x = 0.07.

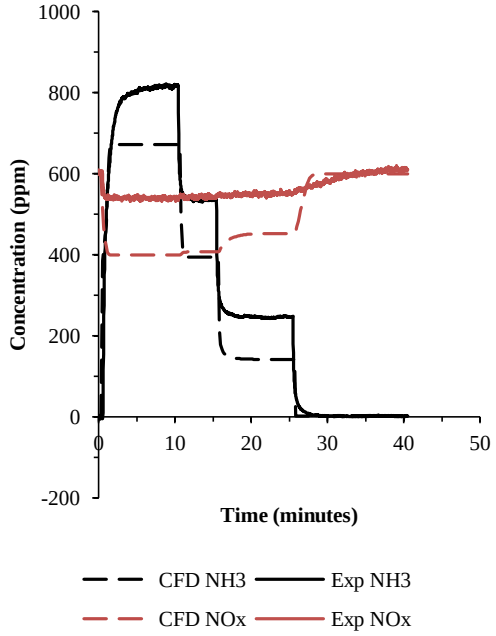

Fig 7.15: CFD and experimental transient concentration profiles for a value of Ω = 400mol-sites.m^{-3}. Brick length = 30mm, NO_2: NO_x = 0.07.

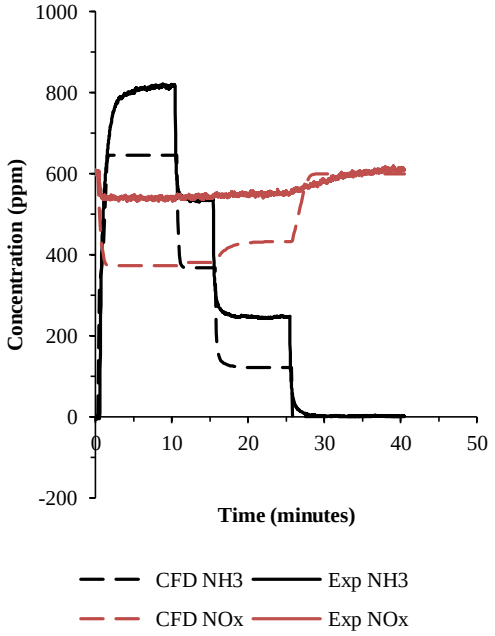

Fig 7.16: CFD and experimental transient concentration profiles for a value of Ω = 500mol-sites.m^{-3}. Brick length = 30mm, NO_2: NO_x = 0.07.

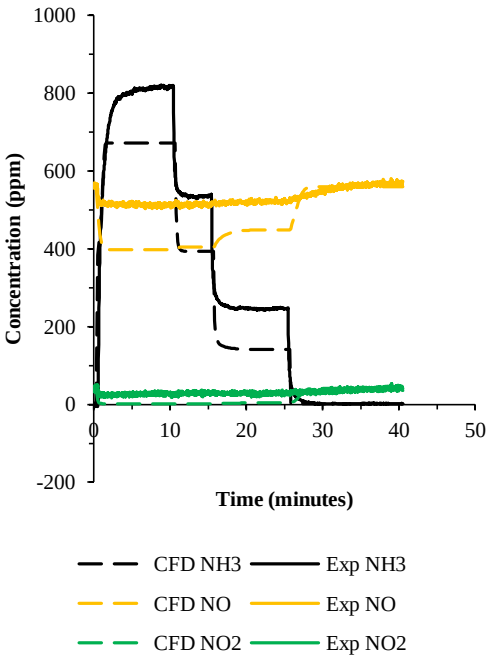

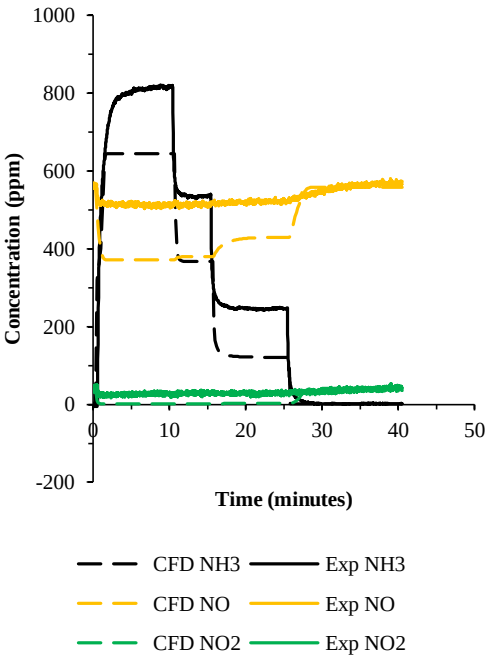

It can be reasoned that even though the model over-predicts the transient NO_2 consumption when α_1 = 1.5 and 1.0, the inlet NO_2 is very small when compared with the inlet NO, and could therefore be ignored for this condition.

It is noticed that for the cases of α_1 = 1.5 and 1.0, the steady-state agreement between the simulations, for all values of Ω investigated, and the experiments is quite poor for the species ammonia, however,

the transient response times are observed to be quite similar. It can be seen that when α_1 is decreased to 0.5 the CFD model best represents the experimental data when $200 < \Omega < 300$mol-sites.m^{-3}. The transient profile agreement between the model and the experiments is shown to be reasonable when the gas is turned off, however, the model over-predicts the rate of depletion for all values of Ω.

7.3 Discussion

A 1D CFD analysis was undertaken to examine the steady-state and transient performance of a mathematical model against data obtained from an experimental exhaust using ammonia gas for an engine condition of 1500rpm, and 6 bar BMEP without EGR.

It can be seen that in general, the CFD model provides adequate agreement with the experimental data, however, the model is unable to successfully predict the influence of the 'NO_2 + NH_3' SCR reactions just after the inlet of the brick. One notices that the 'fast' SCR reaction, involving equi-molar amounts of NO and NO_2, is more dominant in the model, although this might be expected at lower temperatures, due to the formation of ammonium nitrate. [Grossale et al, 2009] It is also witnessed at temperatures of around 300°C where the formation of ammonium nitrate is unlikely due to its decomposition temperature being at about 210°C. One could possibly attribute this to a difference in washcoat formulations.

The effect of the inlet ammonia on the rate of conversion for all species is also noticed to be greater in the model than in the experiments, as the value of Ω required to obtain a good agreement between the model and the experiments decreases, as α_1 increases. One could imply that there is a greater dependency on the amount of ammonia stored on the catalyst surface in the model than in the experiments, as all other input conditions remain the same.

It is observed that for the transient analyses, the overall ability of the CFD model to replicate the transient performance obtained from the experiments for any one value of Ω is quite poor. It is noticed that, when α_1 is decreased, the input value of Ω must be increased to improve agreement; this is also observed in the steady-state analyses. One possible reason for this could be the higher space velocities that are associated with shorter bricks length, as agreement improves as the space velocity is decreasing. It is also observed that the slight decrease in NO_x conversion when $\alpha_1 \geq 1.0$ is not predicted by the model, thus suggesting that an ammonia inhibition effect that would need to be included in the model [Grossale et al, 2009]. There are mathematical models that deal with ammonia and water inhibition, however, the kinetic parameters were not made available. [Winkler et al, 2003]

The experimental data shows that an ammonia transient response time of about 6 – 7 minutes when ammonia is first injected into the exhaust, however, one notices that the reponse time of the model is considerably faster, suggesting that more ammonia is absorbed onto the catalyst in the experiments than in the simulations. It can be seen that when the desorption term $(1 - \alpha_3\theta)$, used to describe the

strength of ammonia molecule bonding to the adsorption sites, is further analysed that the value of α_3 used in the model, is equal to 0.98 [Olsson et al, 2008], which is noticeably higher than other values of α_3 described in other models for zeolite SCRs, which quote values of 0.545 and 0.31. One could imply that the ammonia molecules are more strongly bonded to the adsorption sites when these schemes are compared with the current model. [Chatterjee et al, 2007] and [Chi et al, 2005].

Chapter 8: CFD Modified Kinetic Schemes

8.1 Initial Mofications

It was observed that from the findings obtained in Chapter 7, the CFD simulations were unable to successfully describe the influence of the 'fast' and 'NO_2 + NH_3' SCR reactions at low temperatures. Modifications were therefore made to the kinetic scheme, which enhanced/ inhibited the effect of certain reactions by multiplying each reaction rate by an arbitrary constant. The adjustments made are described in Tab 8.1; all analyses were undertaken for a value of Ω = 400mol-sites.m^{-3}, as this provided better overall agreement with the experimental data for all values of α_1.

The objective was to reduce the rate of the 'fast' SCR reaction in the model, thus reducing its influence on the NO_2 and NO conversion rates.

Scheme Number	'Standard' SCR	'Fast' SCR	'Slow' SCR	'N_2O' SCR
[1]	x 1	x 0.5	x 1	x 1
[2]	x 0.5	x 0.25	x 1	x 1
[3]	x 0.5	x 0.1	x 1	x 1
[4]*	x 0.5	x 0.1	x 1	x 1
* Reaction scheme [4] uses an ammonia adsorption inhibition term that is not used in reaction schemes [1] – [3].				

Tab 8.1: Modified reaction schemes.

It was also noticed in Fig 7.4 that the amount of ammonia adsorbed in the model has a stronger dependency on the ammonia inlet concentration in the model that it did in the experiments. Equation (72) describes the original ammonia adsorption/desorption kinetics used in the model [Olsson et al, 2008]:

$$r_{Net} = k_{1,f} C_{NH3} \theta_{S1-vacant} - k_{1,b} \theta_{NH3-S1} \quad \text{.....} \quad (72)$$

Net rate = (adsorption rate – desorption rate)

where the adsorption rate is governed by the left-hand side the equation. The adsorption rate was modified based on a comparison between steady-state engine and CFD data, where it was noticed that when α_1 = 0.5, approximately double the amounts of ammonia and NO_x were converted in the experiments for the first 30mm. It was also observed that less ammonia was converted in the experiments just after the SCR inlet than in the model for the case of α_1 = 1.5. Equation (73) describes the difference between the experimental and base case CFD data. A complete derivation is located in Appendix 2.7 of this thesis.

$$\Delta_{NH3-Conv} = 1.471 C_{NH3-Inlet}^{-0.81} \quad \text{.....} \quad (73)$$

Equation (73) was then input into equation (72), as shown in equation (74), which was input into the user subroutine for mass transfer:

$$r_{ads} = 1.471 C_{NH3-Inlet}^{-0.81} k_{1,f} C_{NH3} \theta_{S1-vacant} - k_{1,b} \theta_{NH3-S1} \quad \text{(74)}$$

The main function of this expression is to increase or decrease the dependency on the inlet ammonia by adjusting the rate constant of the ammonia adsorption rate equation, depending on how much ammonia is present upstream of the SCR.

8.2 Steady-State Analysis

Figs 8.1, 8.2, 8.3, and 8.4 plot the spatial species conversion profiles for NO_x, NO, NO_2, and ammonia for the same initial condtions described in Tab 7.1 respectively. The species concentrations along the brick for each CFD scheme can be found in Appendix 4.2 of this thesis.

It is observed in that in Fig 8.1, scheme [4] provides very good correlation with the experimental data for all values of α_1, particularly for the case of α_1 = 0.5, where the other schemes under-predict the NO_x conversion for the first 60mm. It can be seen that when α_1 = 1.0 all of the schemes provide either moderate or very good agreement with the engine tests, however, only schemes [3] and [4] are successfully able to simulate the engine tests.

Fig 8.2 plots the spatial NO conversion. One notices that schemes [3] and [4] are seen to offer the best representation of experimental data for the entire length of the brick when α_1 = 0.5 and 1.0. Schemes [3] and [4] also perform quite well when α_1 = 1.5; however, towards the end of the brick, the model slightly under-predicts the experimental data.

The spatial NO_2 conversion profiles that are plotted in Fig 8.3 show that for the first 50mm, when α_1 is equal to 0.5, scheme [4] is shown to replicate the engine test results very well, although beyond this, scheme [4] is shown to over-predict the NO_2 conversion. It can be seen that scheme [1] provides the best prediction towards the end of the brick. When stoichiometric levels of ammonia are injected, All schemes are noticed to provide excellent agreement of the experiments for the case of α_1 = 1.0, and schemes [3] and [4] provide the best representation along the entire brick, whilst the other schemes all over predict up to the end of the brick when α_1 = 1.5.

Fig 8.4 displays the ammonia conversion profiles, and shows that scheme [4] is able to successfully predict the ammonia conversion along the brick for when α_1 = 0.5. and scheme [1] offers the best representation of the data when α_1 = 1.0, with the other schemes all under-predicting ammonia conversion after about 70mm. It is noticed that all of the schemes over-predict the consumption rate just after the inlet, although correlation is improved for schemes [2] – [4] after about 90mm for the case of α_1 being equal to 1.5.

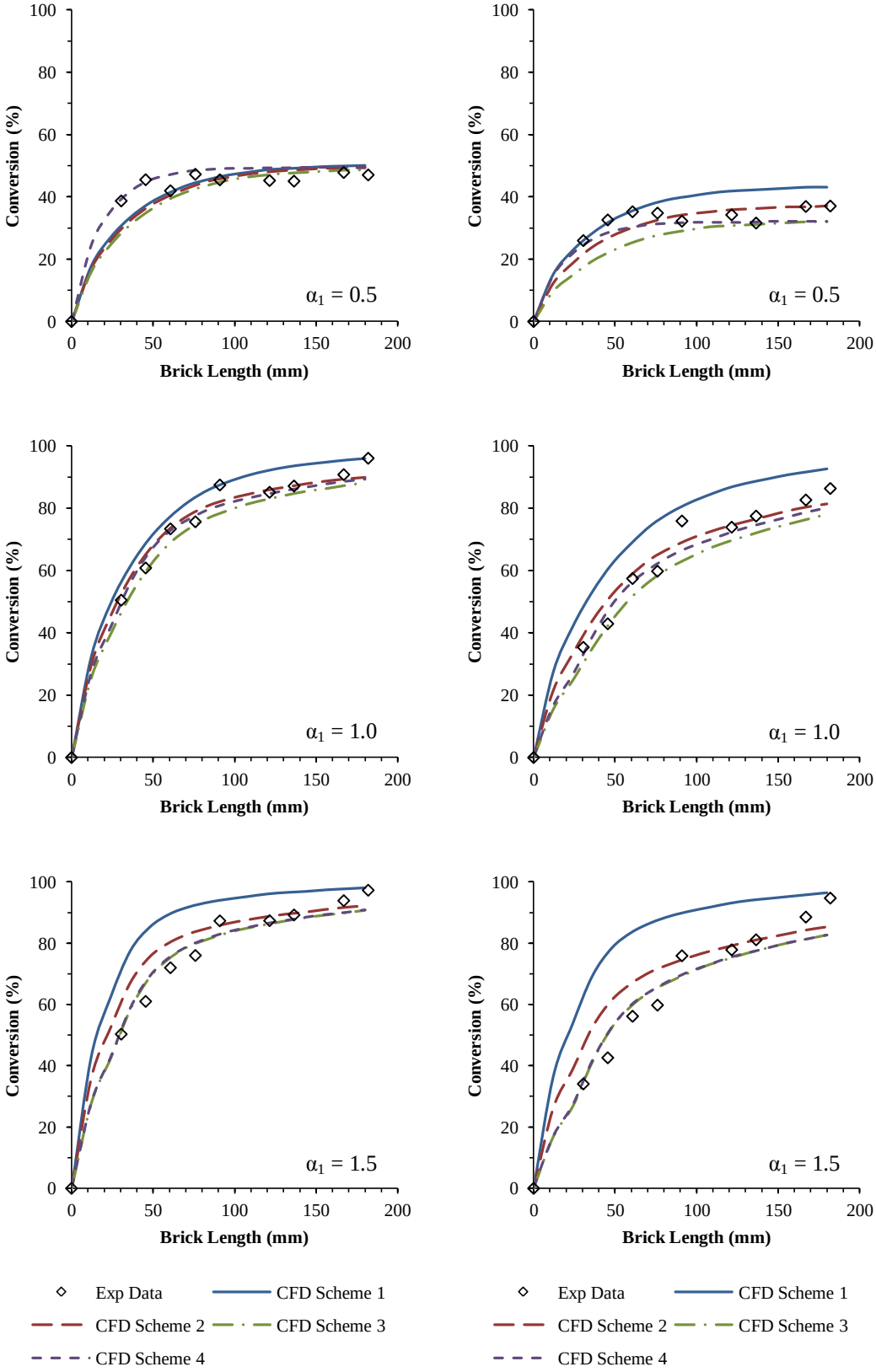

Fig 8.1: CFD and experimental spatial NO_x conversion profiles for modified schemes.

Fig 8.2: CFD and experimental spatial NO conversion profiles for modified schemes.

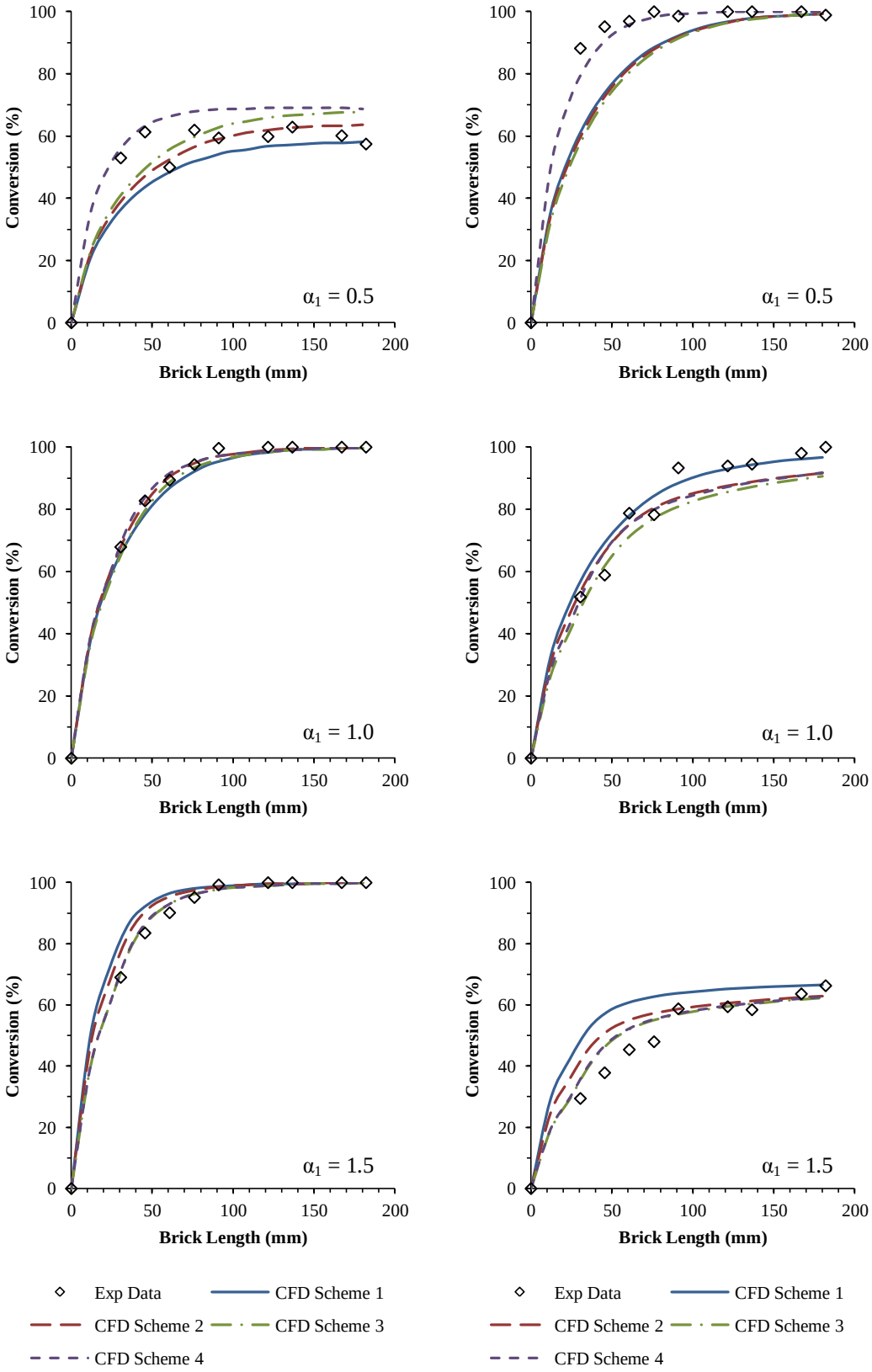

Fig 8.3: CFD and experimental spatial NO_2 conversion profiles for modified schemes.

Fig 8.4: CFD and experimental spatial NH_3 conversion profiles for modified schemes.

8.3 Transient Analysis

Two separate transient investigations were conducted in this section. Section 8.3.1, focuses on the transient performance of the different CFD schemes described in Tab 8.1, whilst Section 8.3.2 focuses on changing the ammonia desorption kinetics.

8.3.1 Modified Reaction Schemes – Initial Modifications

Figs 8.5 – 8.8 plot the transient profiles for a brick length of 30mm when the NO_2: NO_x ratio = 0.60, and Figs 8.9 – 8.12 display the transient profiles for a brick length of 45.5mm when the NO_2: NO_x ratio = 0.64. Figs 8.13 – 8.16 plot the transient profiles for a brick length of 30mm with an NO_2: NO_x ratio of 0.07.

It is is observed that when α_1 = 2.0 and 1.5, scheme [3] and scheme [4] provide a good agreement with experimental data for the transient NO_x profiles. It can be seen that when α_1 = 1.0 and 1.5, the model is able to predict the engine test data quite well for scheme [4], although the transient NO_x increase from 1.0 to 0.5, however, is poorly predicted.

Schemes [2] – [4] are shown to provide an adequate agreement with the experimental data with regards to the transient a steady-state NO concentration when α_1 = 2.0 and 1.5, whilst scheme [1] is observed to provide a very good steady-state agreement with the experiments when α_1 = 1.0.One notices that the model over-predicts the steady-state NO concentration for the case of α_1 = 0.5, although the predictions are slightly better for schemes [1] and [4]. The transisent response profiles are adequately predicted for all schemes.

It can be seen that for NO_2, scheme [4] provides a very good agreement with the experimental data for the cases of α_1 = 2.0 – 1.0, when α_1 = 0.5, [1] – [3] are observed to over-predict the NO_2 concentration, whilst scheme [4] under-predicts the NO_2 concentration. The schemes that provide closest agreement with the experimental data are schemes [3] and [4].

It can be seen that when the transient ammonia concentrations are analysed, schemes [3] and [4] provide reasonable agreement with the experimental data for the steady-state values when α_1 = 2.0 and 1.5, however, the adsorption time is over-predicted. The best representation of the experimental data is achieved for scheme [2] when α_1 is decreased to 1.0, although scheme [3] and scheme [4] provide adequate agreement with the experiments. It can be seen that scheme [4] slightly under-predicts the engine test data when α_1 = 0.5, whilst schemes [1] – [3] all noticeably over-predict the steady-state ammonia concentration, the ammonia desorption time is also slightly under-estimated by all schemes.

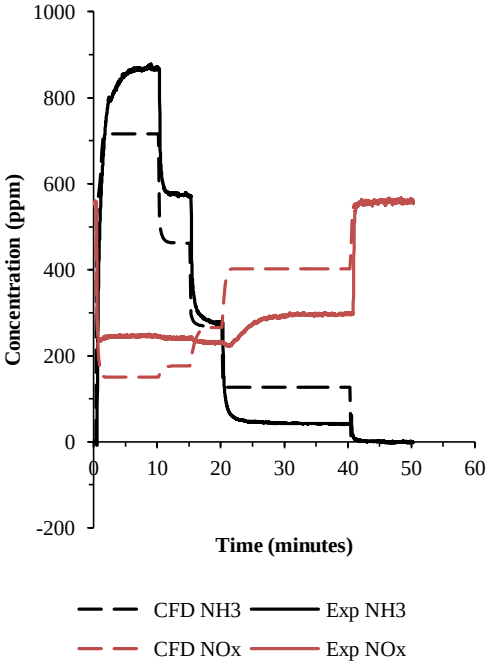

Fig 8.5: CFD and experimental transient concentration profiles for CFD scheme [1]. NO_2: NO_x = 0.60, brick length = 30mm.

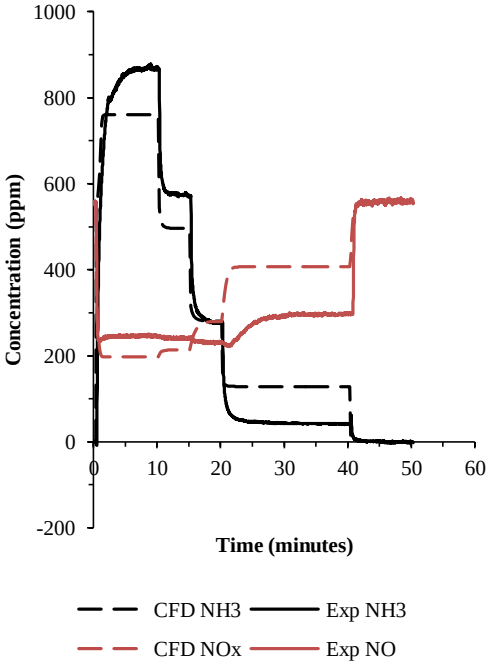

Fig 8.6: CFD and experimental transient concentration profiles for CFD scheme [2]. NO_2: NO_x = 0.60, brick length = 30mm.

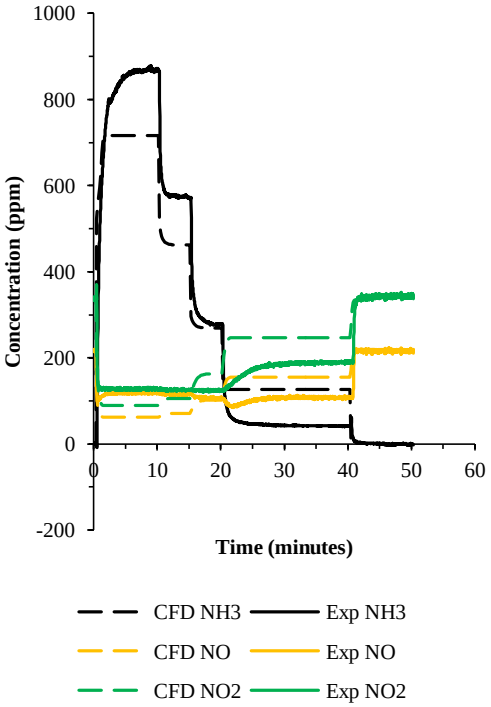

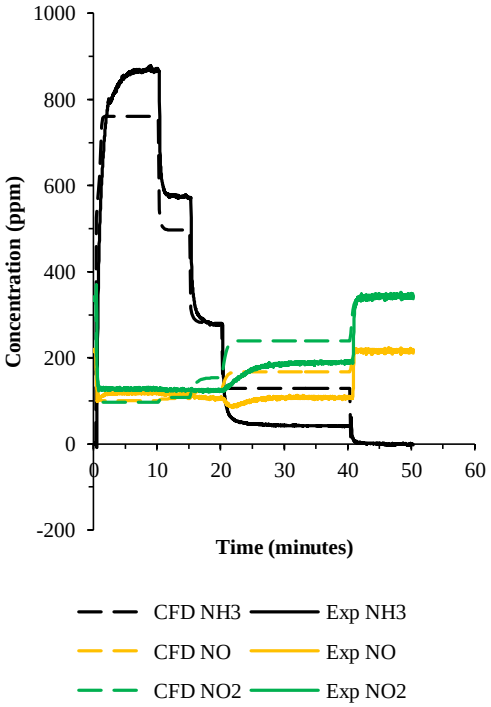

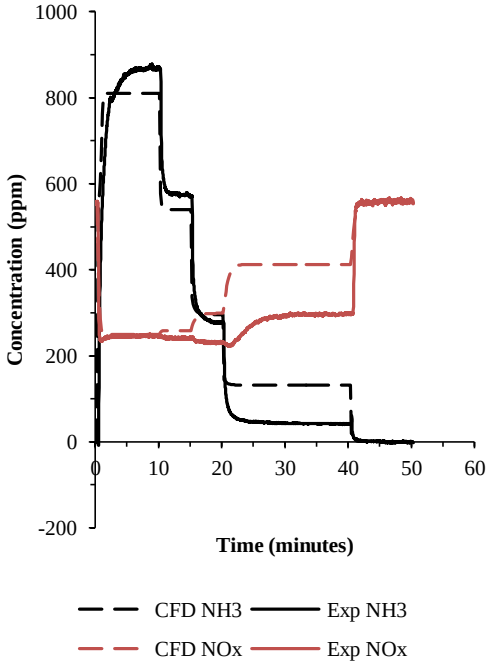

Fig 8.7: CFD and experimental transient concentration profiles for CFD scheme [3]. NO_2: NO_x = 0.60, brick length = 30mm.

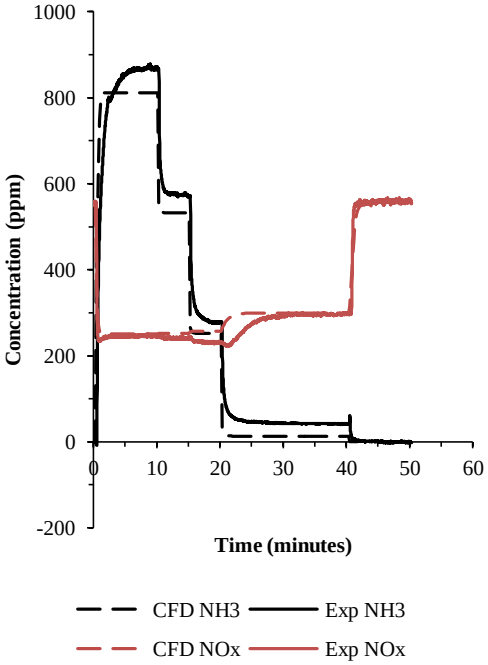

Fig 8.8: CFD and experimental transient concentration profiles for CFD scheme [4]. NO_2: NO_x = 0.60, brick length = 30mm.

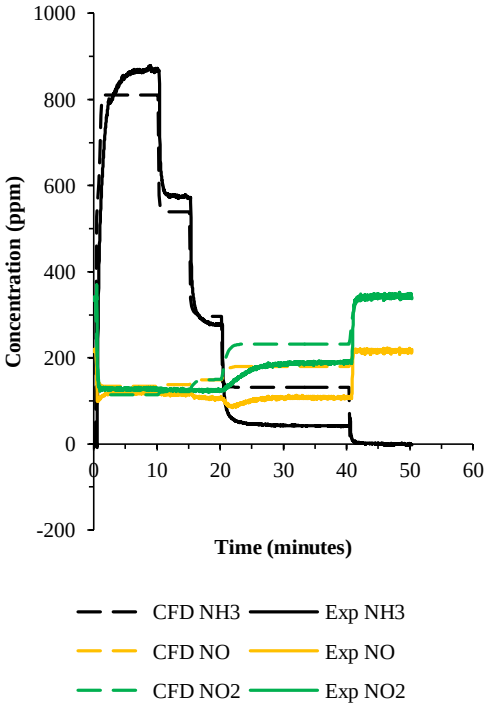

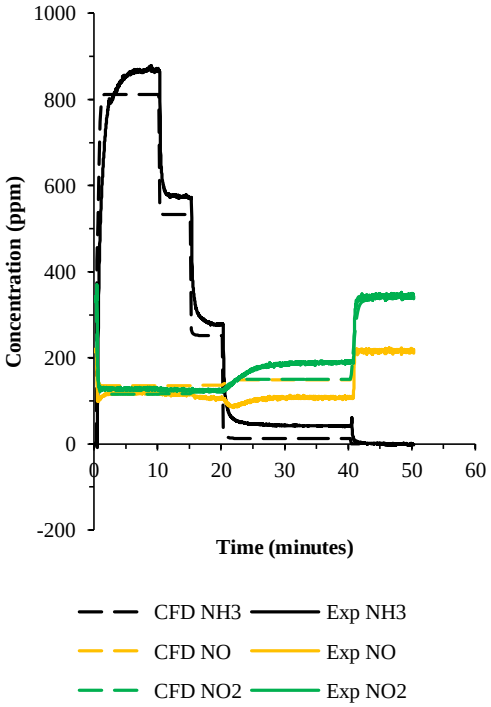

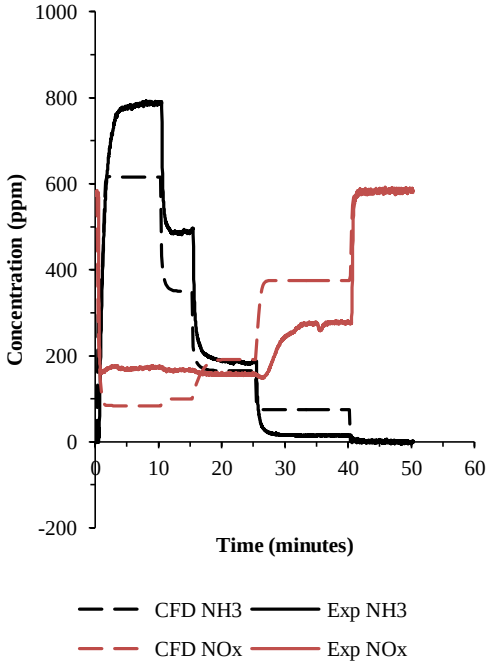

Fig 8.9: CFD and experimental transient concentration profiles for CFD scheme [1]. NO_2: NO_x = 0.64, brick length = 45.5mm.

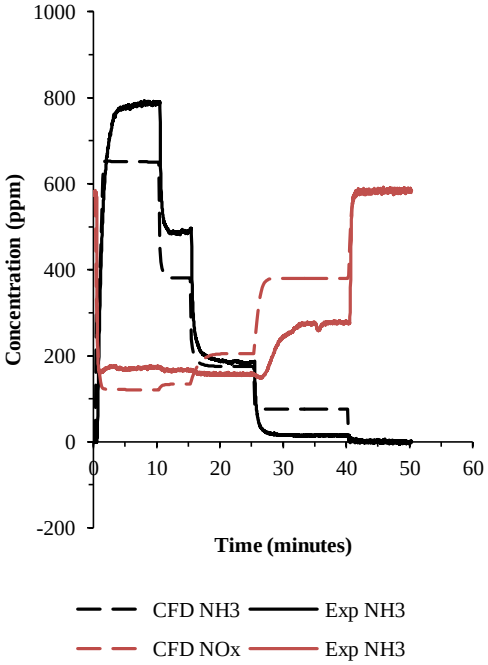

Fig 8.10: CFD and experimental transient concentration profiles for CFD scheme [2]. NO_2: NO_x = 0.64, brick length = 45.5mm.

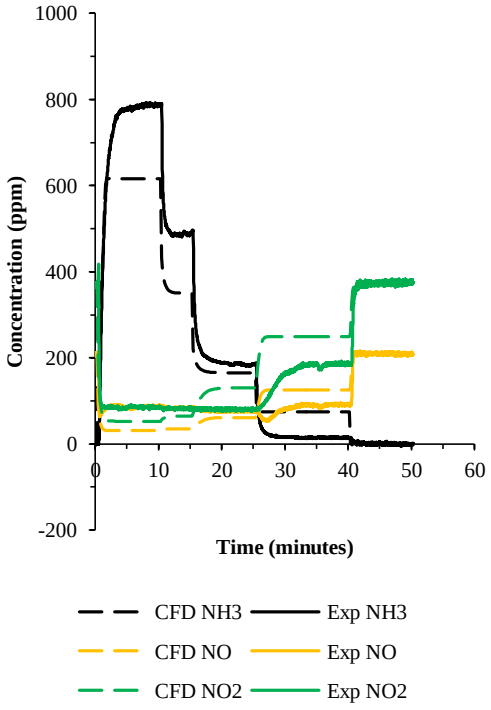

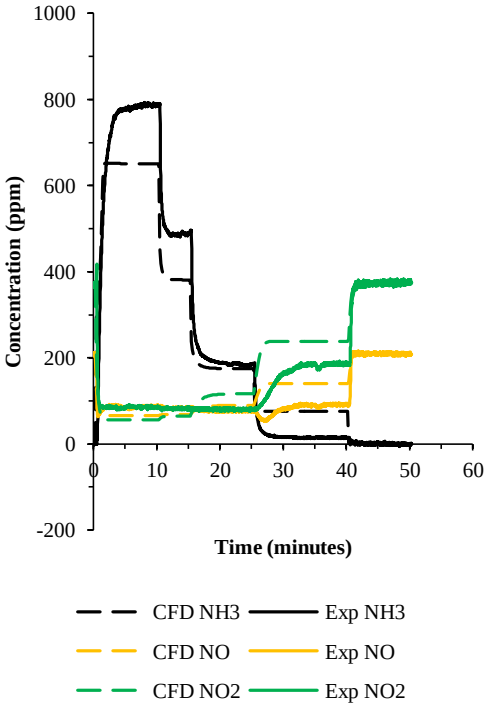

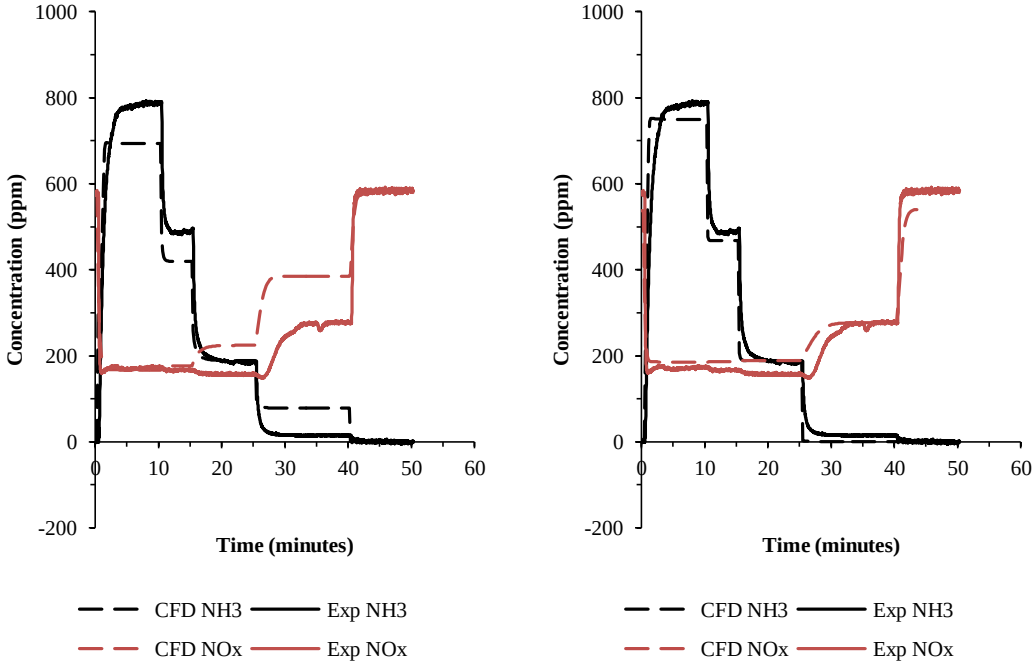

Fig 8.11: CFD and experimental transient concentration profiles for CFD scheme [3]. NO_2: NO_x = 0.64, brick length = 45.5mm.

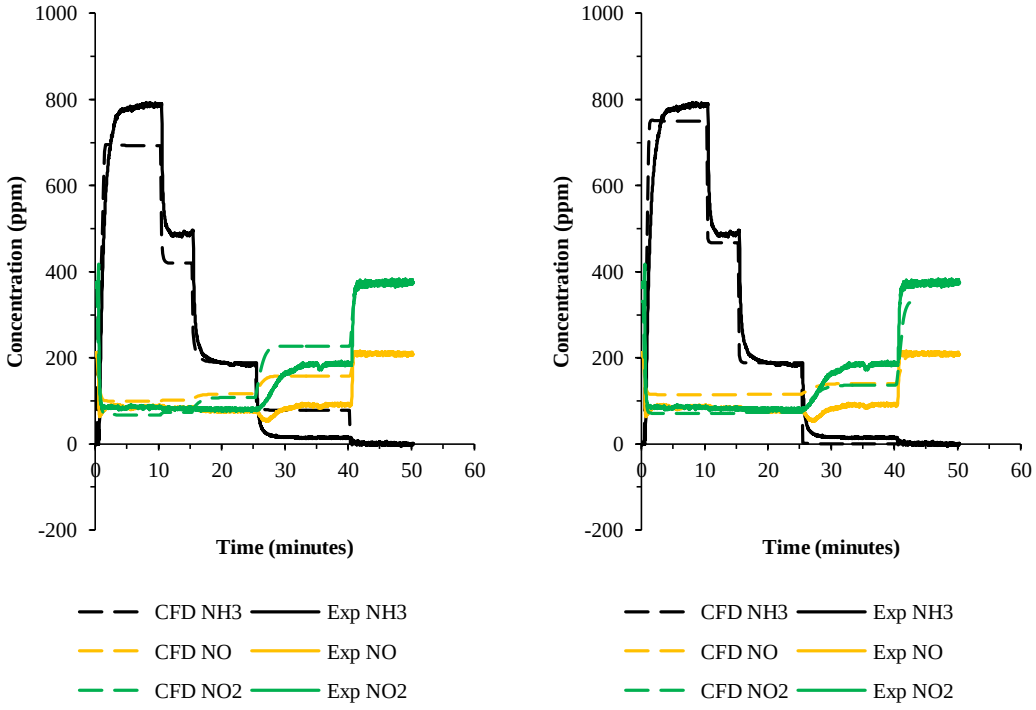

Fig 8.12: CFD and experimental transient concentration profiles for CFD scheme [4]. NO_2: NO_x = 0.64, brick length = 45.5mm.

It can be seen that when α_1 = 2.0 - 1.0, scheme [3] and scheme [4] both provide the best representation of the experimental NO_x profile, however, scheme [4] is noticed to accurately predict the steady-state NO_x value for the case of α_1 = 0.5.

When the transient NO profiles are analysed, for the cases of α_1 = 2.0 – 1.0, CFD scheme [2] provides the best agreement with the experimental data. When α_1 is then decreased to 0.5 it is observed that schemes [1] and [4] offer the best representation of the experimental data.

It is observed that for the transient NO_2 profiles, scheme [4] provides a very good agreement with the experiments for the ccases of α_1 = 2.0 – 1.0, and when α_1 = 0.5, it is observed that schemes [1] – [3] over-predict the NO_2 concentration, while scheme [4] under-predicts the amount of NO_2 present. The transient NO_2 profile for α = 0.5 is best represented when scheme [4] is used.

It can be seen that when α_1 = 2.0 and 1.5, scheme [4] provides a reasonable agreement with the experimental steady-state ammonia concentration, however, the transient response time when ammonia is first injected into the exhaust is slightly under-predicted. One notices that schemes [2] – [4] all provide a very good agreement with the experimental data when α_1 = 1.0, and for the case of α_1 = 0.5, the best predictions are observed with CFD scheme [4].

One observes that for all values of α_1 investigated, the model under-predicts the amount of NO_x, NO, and ammonia present in the exhaust downstream of the brick for all CFD schemes investigated, with the closest agreement being provided by CFD schemes [3] and [4]. Although the model also under-predicts the NO_2 concentration when ammonia is injected, this could possibly be ignored as only a very small amount of NO_2 is actually detected at the inlet.

It can be seen that although the model with the modifications described at the beginning of this chapter provides a better agreement with the experimental data for steady-state concentrations, the model still under-predicts the ammonia transient ammonia response time when ammonia is first injected into the exhaust, and also when α_1 = 0.5. The modifications made to the ammonia adsorption scheme therefore do not completely describe the adsorption and desorption processes.

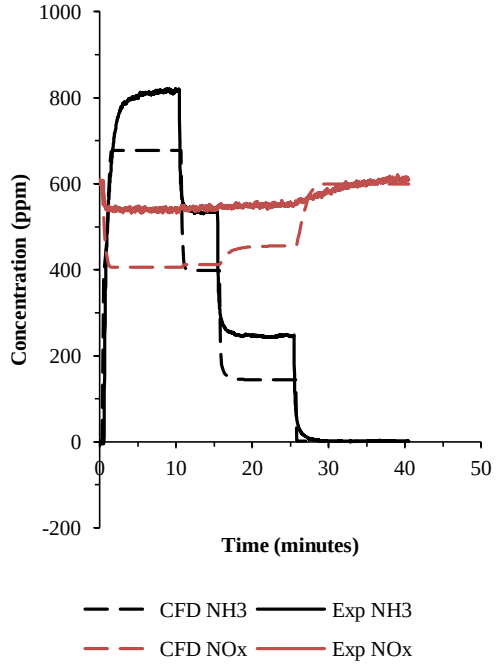

Fig 8.13: CFD and experimental transient concentration profiles for CFD scheme [1]. NO_2: NO_x = 0.07, brick length = 30mm.

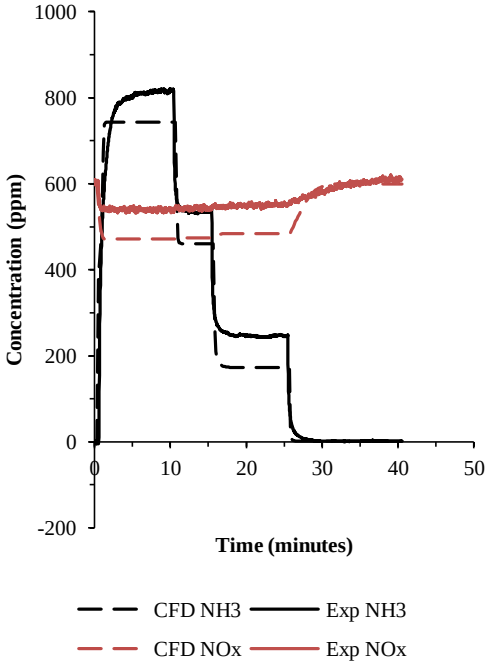

Fig 8.14: CFD and experimental transient concentration profiles for CFD scheme [2]. NO_2: NO_x = 0.07, brick length = 30mm.

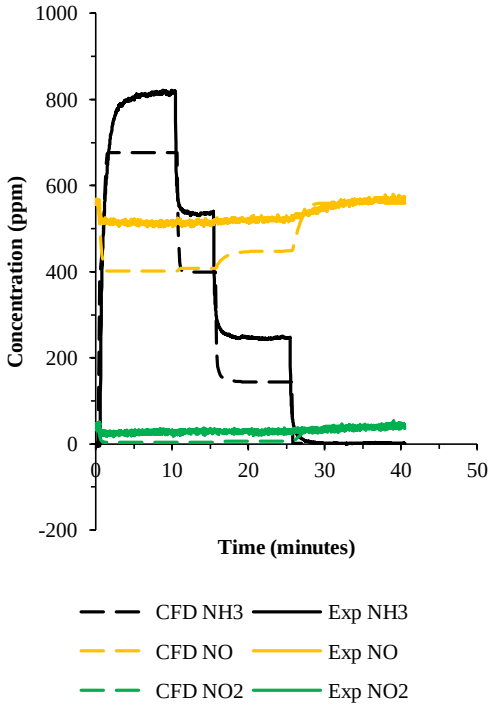

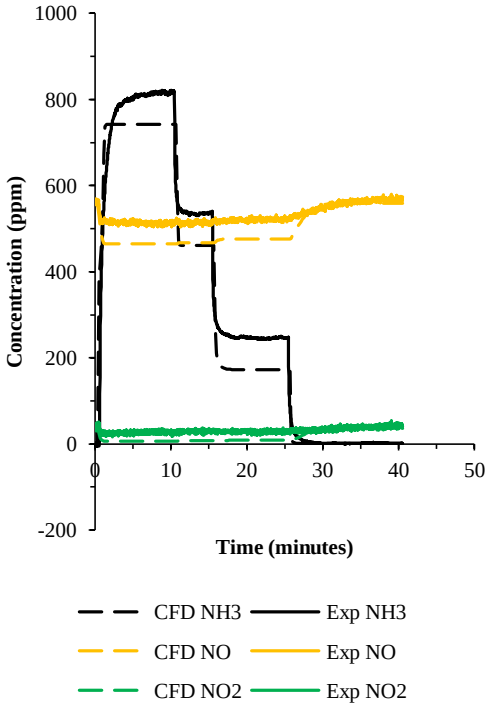

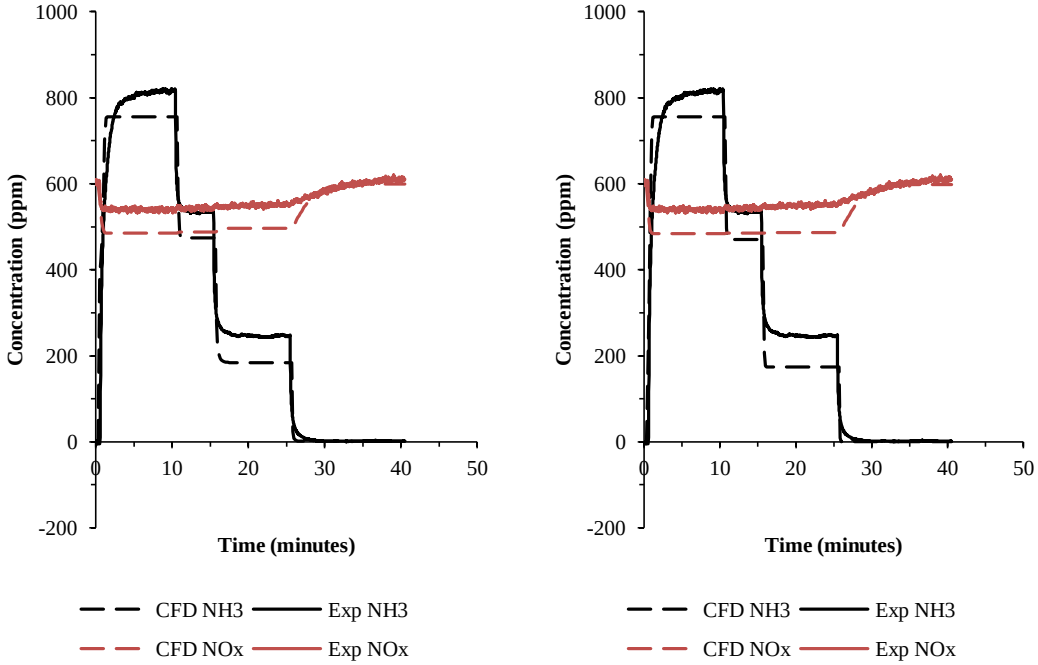

Fig 8.15: CFD and experimental transient concentration profiles for CFD scheme [3]. NO_2: NO_x = 0.07, brick length = 30mm.

Fig 8.16: CFD and experimental transient concentration profiles for CFD scheme [4]. NO_2: NO_x = 0.07, brick length = 30mm.

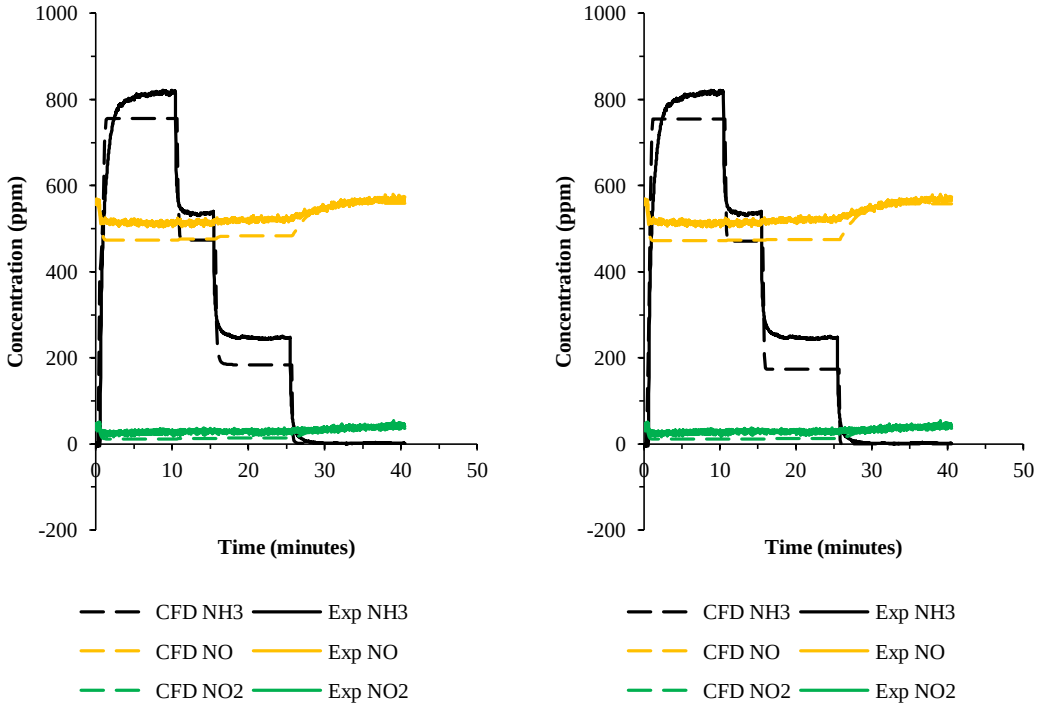

8.3.2 Modified Ammonia Desorption Schemes

As discussed in Section 7.3.2 of this thesis, the multiplier of θ in term $(1 - \alpha_3\theta)$ is quite high in the scheme used in this investigation, when compared with other schemes that focus on Cu-zeolite based catalysts.

Figs 8.17 and 8.18 plot the transient profiles for a 30mm brick when the NO_2: NO_x = 0.60, and Figs 8.19 and 8.20 display the transient profiles for a 45.5mm brick with an NO_2: NO_x ratio of 0.64. These are compared with Fig 8.8 and Fig 8.12 respectively. CFD scheme [4] has been selected, as this was observed to provide agreement with the experimental data for all of the ammonia injection conditions investigated.

The transient NO_x and ammonia concentration profiles when the desorption expression is equal to (1 - 0.545θ), as described by Daimler-Chrylser, for the 30mm and 45.5mm bricks are plotted in Fig 8.17 and 8.18 respectively. [Chatterjee et al, 2007] Fig 8.19 and Fig 8.20 plot the transient NO_x and ammonia profiles for the 30mm and 45.5mm bricks respectively, for the desorption expression: (1 - 0.31θ), used by Cummins. [Chi et al, 2005]

It is observed that in Fig 8.17, when ammonia is first injected into the exhaust, the inital rise in ammonia correlates better with the experiments than in Fig 8.8. The transient response time is also more representative of that of the experimental data when α_1 = 1.5 and 1.0.

It is noticed in Fig 8.18 that although the model is able to adequately predict the transient ammonia profile when the gas is first injected, the steady-state value is noticeably under-predicted. A similar trend is witnessed when α_1 is decreased to 1.5 and 1.0.

One observes that in Fig 8.19, a slight improvement in the transient ammonia profile, plotted in Fig 8.19, is seen when the model is compared with the engine test data for α_1 = 2.0, although the model under-predicts the steady-state concentrations by an even greater amount than the scheme used in Fig 8.17. A similar observation is made when α_1 = 1.5 – 0.5.

It can be seen that a similar behaviour occurs in Fig 8.20 to that in Fig 8.19 when CFD scheme [4] is used, and the desorption characteristics of the catalyst are altered, although the steady-state response time is increased, the steady-state concentrations for both ammonia and NO_x are decreased.

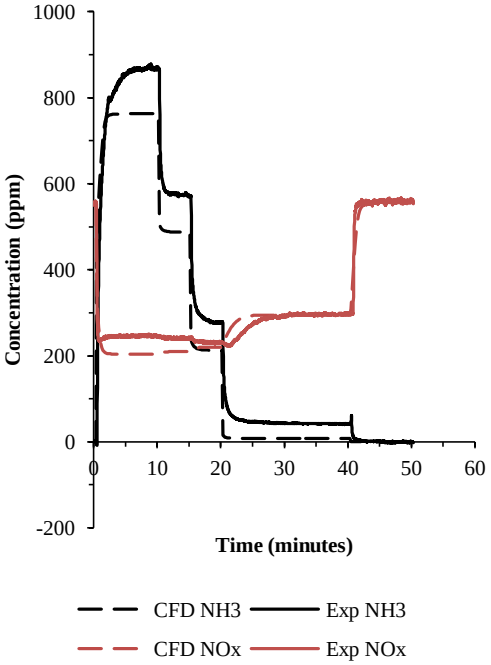

Fig 8.17: CFD and experimental NO_x, and ammonia transient concentration profiles for CFD scheme [4]. Brick length = 30mm, NO_2: NO_x = 0.60, and (1 – 0.545θ).

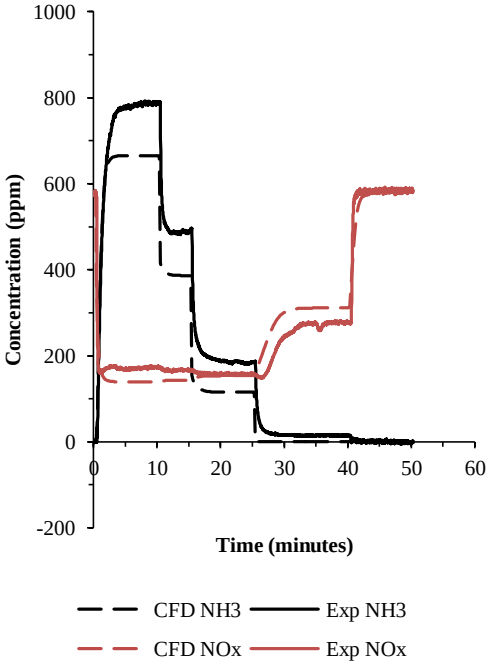

Fig 8.18: CFD and experimental NO_x, and ammonia transient concentration profiles for CFD scheme [4]. Brick length = 45.5mm, NO_2: NO_x = 0.64, and (1 – 0.545θ).

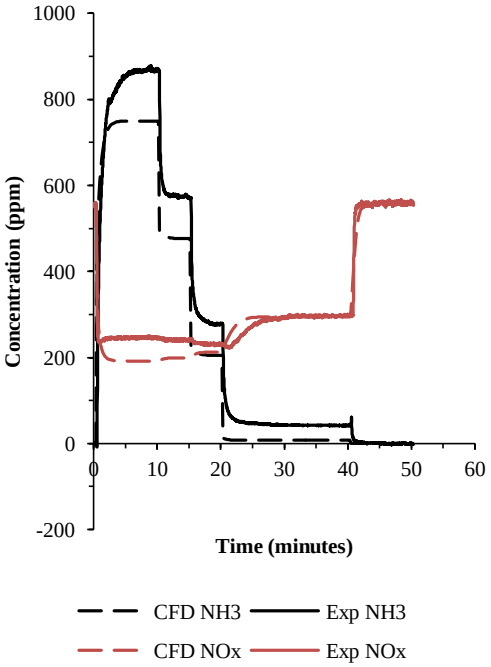

Fig 8.19: CFD and experimental NO_x, and ammonia transient concentration profiles for CFD scheme [4]. Brick length = 30mm, NO_2: NO_x = 0.60 and (1 – 0.31θ).

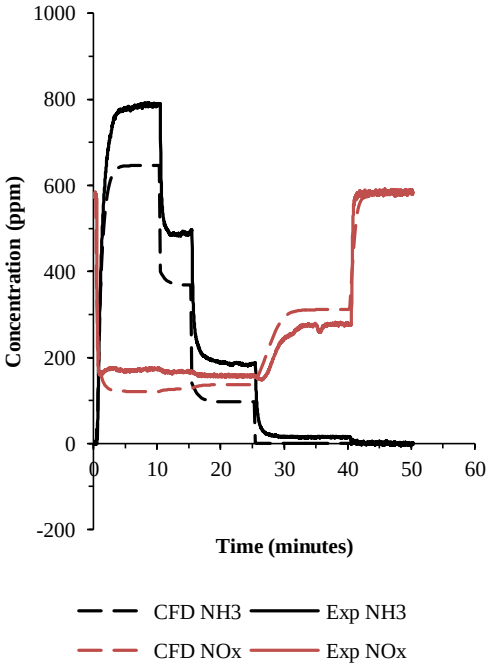

Fig 8.20: CFD and experimental NO_x, and ammonia transient concentration profiles for CFD scheme [4]. Brick length = 45.5mm, NO_2: NO_x = 0.64, and (1 – 0.31θ).

8.4 Discussion

Further analyses were undertaken to examine the steady-state and transient performance of the modifications to the CFD model described in Sections 8.1 – 8.3 of this thesis; this section discusses the findings from these investigations.

It is observed that for the steady-state and transient analyses, plotted in Figs 8.1 – 8.4 and Figs 8.5 – 8.16 respectively, that the when $\alpha_1 \geq 1.0$, the inhibition of the 'standard' and 'fast' SCR reactions provide a noticeably better agreement with the experimental data than the base cases described in Section 7.2 of this report. The introduction of a simple empirical term further improves the models ability to predict simple transient analyses as well as steady-state analyses, particularly when $\alpha_1 < 1.0$ and when a substantial quantity of NO_2 is present in the exhaust. However, when the NO_2: NO_x ratio is very low, the influence of the empirical term is reduced; this could be attributed to the low-temperature activity of the 'standard' SCR reaction being higher in the simulations than in the experiments. Further refinement of the model in this area would therefore be required, and that further investigation would need to be conducted for a broader range of NO_2: NO_x ratios and exhaust gas temperatures.

The addition of an empirical term is observed to have a positive effect on the performance of the CFD model under steady-state conditions, however, the model is still not able to accurately predict transient ammonia profile, particularly when ammonia is first injected into the exhaust. It could also be stated that this term may not adequately describe what is physically happening on the catalyst washcoat, as factors such as ammonia, water, and hydrocarbon inhibition might also have an effect on the performance of the SCR. [Winkler et al, 2003] and [Tennison et al, 2004]. The usefulness of this term should therefore be decided on the basis of whether it is more desireable to only achieve a good prediction of experimental data, or to further investigate what is happening on the SCR.

An investigation into altering the rate of ammonia desorption was also investigated, which was undertaken with the primary objective of obtaining a better agreement between the model and the experiments with regards to the transient ammonia profile, particularly when ammonia is first injected into the exhaust. It was observed that by decreasing the multiplier of θ in the expression $(1 - \alpha_3\theta)$, increases the steady-state response time, but decreases the steady-state value. This suggests that the catalyst in the model is able to absorb more ammonia, and therefore increase the activity of the SCR reactions when this multiplier is decreased.

Chapter 9: Concluding Remarks and Recommendations for Future Work

The general conclusions from the results obtained in this thesis, and also recommendations for further research on the behaviour of SCR catalysts under different conditions are presented in this chapter. Previous studies undertaken have focussed on a comparison between ammonia gas and urea-spray for 1, 2, 3, and 4 litre SCR bricks for an engine condition of 1500rpm and 6bar BMEP [Tamaldin, 2010]. The focus of this study has been on the spatial species conversion profiles along the SCR brick for different NO_2: NO_x ratios, as well as transient performance for the short catalyst bricks, where the space velocities are very high. A CFD model using the 'porous medium' approach with a kinetic scheme available in open literature [Olsson et al, 2008] was then evaluated against the experimental data. Most of the published work focuses on what is happening at the end of the catalyst brick, however, this work focuses on what is happening along the SCR; this provides a more rigorous method of evaluating the model. [Sturgess et al, 2010]

The conclusions in this chapter are presented in the following sections:

9.1 Engine Tests

Engine tests were conducted on a test rig used in previous work. A new engine and new SCR catalyst bricks were supplied for this work. To provide continuity with previous work, the engine condition of 1500rpm, 6bar BMEP was used, this provided an SCR inlet temperature of about 210°C, which is noticeably lower than that obtained previously. [Tamaldin, 2010] The engine mass flow rate was obtained directly from the ECU via GREDI.

The Horiba MEXA-1170 Nx gas analyser was fitted with ammonia scrubbers with the intention of adsorbing any excess ammonia, preventing a reaction between NO_2 and ammonia on the NO_x converter catalyst. The performance of these scrubbers was also observed during this work, and they were found to be not completely satisfactory.

9.1.1 Steady-State Tests

The steady-state tests discussed in Chapter 7 of this report were undertaken for a DOC/DPF combination of a single DOC located downstream of the DPF, which provided an NO_2: NO_x ratio close to 0.5.

It was observed that just after the inlet of the brick, approximately double the amount of NO_2 with respect to NO was consumed; this suggests that the 'NO_2 + NH_3' SCR reactions occur at the same rate as the 'fast' SCR reaction. Further analysis of the data suggests that the dominant 'NO_2 + NH_3' reaction was the 'N_2O formation' reaction as approximately equi-molar amounts of NH_3: NO_x were consumed just after the inlet.

The majority of the NO_x conversion was observed to take place within the first 91mm of the brick for all values of α investigated in this study,however, NO_x conversion ceses at about 45.5mm due to complete consumption of ammonia when $\alpha_1 = 0.5$. A conversion rate of just under 100% was observed after 182mm, when $\alpha_1 = 1.0$, and 1.5; this suggests a good low-temperature activity of the SCR.

9.1.2 Transient Tests

The transient tests described in Chapter 7 were undertaken for the same engine conditions described in Section 9.1.1. The NO_2: NO_x ratios investigated were ~ 0.60 for 30mm and 45.5mm bricks and 0.07 for the 30mm brick only. The short bricks were investigated because most of the NO_x conversion was observed to take place just after the inlet.

For the case of the 30mm brick, when ammonia is first injected into the exhaust. The steady-state response time is about 4 minutes at 30mm when ammonia is first injected into the exhaust, however, this is increased to about 6 minutes for the 45.5mm brick. As the length of the brick is increased from 30mm to 45.5mm, the number of available adsorption sites are not all saturated with ammonia, suggesting that as the length of the brick increases, the decrease in gas-phase ammonia could have an effect on the rate of adsorption. It is also observed that when the DOC is removed from the exhaust, the quantity of ammonia adsorbed onto the catalyst washcoat is similar with the experiments when a DOC was present.

The downstream NO_x concentration increases when α is decreased from 2.0 to 1.0 as shown in Fig 6.4 and Fig 6.6; this could suggest ammonia inhibition of the 'fast' SCR reaction, although this is very small, the possibility of this inhibition effect being greater at lower temperatures ~ 150°C would require investigation.

9.2 CFD Analyses

9.2.1 Base Case

The objective of the CFD analyses was to obtain a more complete picture of what was happening in the CFD simulations. Different values of Ω were investigated due to the uncertainty of the number of reaction sites on the experimental catalysts. The CFD analyses were also undertaken for different NO_2: NO_x ratios as described in Chapter 6 of this thesis.

The following observations about the base case CFD model were made:

- The amounts of NO_2 and NO consumed at the inlet in the CFD simulations are observed to be lower and higher respectively when compared with the experiments; this shows a noticeable influence of the 'NO_2 + NH_3' reactions at low temperatures, which is not observed in the model. The possibility of nitrate formation is also not included in the model.

- Agreement just after the inlet between the simulations and the experiments, when NO_2 is present in the exhaust, is observed to be quite poor when $\alpha_1 = 0.5$. The model is able to adequately predict the experimental data just after the inlet when $\Omega = 300$mol-sites.m^{-3} for the case of $\alpha_1 = 1.0$; this suggests the influence of inlet ammonia on the adsorption rate in the model is greater than witnessed in the engine tests.

- The transient response time observed in the CFD model, when ammonia is first injected into the exhaust is almost instantaneous when compared with the experimental data; this could imply that the ammonia adsorption capacity of the catalyst in the model might not be as high as the experimental catalyst. This is also observed when the gas is turned off, as the NO_x levels in the experiments require more time than those in the model to recover.

9.2.2 Modified Kinetic Schemes

The modifications to the CFD model, described in Chapter 9 of this thesis, are based on the differences between the model and the experimental data for the base case.

The following observations about the modifications made to the kinetic schemes were made:

- The reduction of the influence of the 'fast' SCR reaction by a factor of 10 enables the model to better predict the experimental data just after the inlet for both steady-state and transient analyses when a noticeable amount of NO_2 is present in the exhaust.

- By applying an empirical term based on experimental data to the ammonia adsorption kinetics as described in equation (74), the model is successfully able to predict the experimental data along the brick when $\Omega = 400$mol-sites.m^{-3} for all values of α investigated. It is observed that although the use of an empirical term in the model is very successful, the link between the mathematical experession and the underlying physical process on the catalyst is less clear.

- The reduction of the value of α in the term $(1 - \alpha_3\theta)$, which is used to determine the amount of ammonia that can be desorbed from the catalyst based on the amount of ammonia present on the adsorption sites, increases the amount of ammonia that can be adsorbed onto the catalyst washcoat thus improving the transient agreement between the model and the test data. The steady-state ammonia concentration decreases, however, as the value of α in the term described is reduced.

- The model over-predicts the NO_x consumption for all values of α when the NO_2: NO_x ratio; this suggests that the modifications made to the model may not take into the account the effect of the NO_2: NO_x ratio.

9.3 Contributions to Knowledge

The contributions to knowledge that have been achieved at the end of this study are as follows:

- Engine test data was obtained at low exhaust gas temperatures as a function of distance and space velocity for a Cu-based zeolite SCR catalyst using ammonia gas, providing more realistic conditions when compared with laboratory based studies. The analysis of the spatial species conversion profiles allows for a more rigorous assessment of mathematical models, and can also assist in determining the size of the catalyst; thus minimising packaging requirements and manufacturing costs.

- The effect of the 'NO_2 + NH_3' reactions at the inlet of the brick is observed to be higher than expected. Further analysis of the experimental data reveals that approximately equi-molar amounts of ammonia and NO_2 are consumed, therefore suggesting that equation (47) on page 46 is the dominant 'NO_2 + NH_3' reaction.

- Possible ammonia inhibition of the 'fast' SCR reaction was also observed during the transient tests. Although this effect was small at these temperatures, more investigation into this effect at temperatures < 200°C is required, where the inhibition effect is likely to be higher [Grossale et al, 2009].

9.4 Recommendations for future work

A number of recommendations for future work can be made as a result of the work undertaken in this study.

9.4.1 Engine Tests

Further investigation into the spatial conversion profiles of an SCR system are required for gas temperatures below 200°C, and for different NO_2: NO_x ratios, which could allow the likely effect of ammonia inhibition of SCR reactions to be analysed further, particularly the formation of NH_4NO_3, which acts as an inhibitor to the 'fast' SCR reaction. The experiments described in this thesis would also need to be repeated for urea spray.

The transient experiments discussed in this report were all undertaken for short SCR bricks, under warm-start conditions, and for a fixed engine condtion. To obtain a much broader scope of how the SCR performs; the catalyst would need to be analysed under 'cold-start' condtions, and also for when the engine is ramped from a low load to high load, as shown on the ECE drive cycle and vice versa. It is also recommended that the transient analyses described in the main body of the report be undertaken for different brick lengths and engine conditions. The objectives of this would be to investigate how an increase in catalyst length would affect the transient response time, and also how the amount of ammonia stored on the washcoat changes with respect to brick length.

Following the recommendations in the literature and in previous work, the analyser used in these experiments was fitted with ammonia scrubbers to adsorb any ammonia present in the sampling gas. It was discovered, however, that the ammonia scrubbers upstream of the analyser chamber began to lose their adsorption efficiency when the concentration of ammonia exceeded a certain level. It is therefore recommended that an FTIR analyser be used instead. If one was continue along the route of using the CLD technique, however, further investigation into this area is strongly recommended. Caution must also be taken when urea spray is used.

9.4.2 CFD Analyses

It can be seen that the modifications made to the reaction kinetics in the CFD model have improved the models' ability to predict the experimental data for the conditions investigated in this study. Further investigation is required via the recommendations described in Chapter 8. The model would also need to be validated for the thermolysis and hydrolysis of urea spray.

The CFD model used in this study was a simple 1D model, which was used to validate the kinetics against the experimental data, although the development of a three-dimensional urea-SCR model would be more desireable for commercial purposes. A full three-dimensional model could be easily achieved using the 'porous medium approach' and the modified kinetics developed in this work and discussed in this thesis.

The work undertaken in this thesis is useful as further understanding into the behaviour of a Cu-zeolite SCR along the brick at low temperatures under engine condtions has been achieved. Modifications to the kinetic scheme used in this study also has potential for future development.

References

The table below shows all of the key references used in this document; these are labelled via numbers in the main report. All references are in alphabetical order from the author, for websites it is the name of the site.

Reference Number	Reference
1	Alimin, A.J. (2006) 'A NO_x Trap Study Using Fast Response Emission Analysers' PhD Thesis, Coventry University.
2	Asik, J.R. Meyer, G.M. Dobson, D. (2000) 'Lean NO_x Trap Desulfation Through Rapid Air Fuel Modulation' SAE 2000-01-1200.
3	Autoblog (2008) 'Volkswagen Finishes up Jetta Blue TDI Development, on Sale this Summer' [Online] Available from <www.autoblog.com> (27th July 2011).
4	Benjamin, S.F. Gall, M. Sturgess, M.P. Roberts, C.A. (2011) 'Experiments on a Light Duty SCR Test Exhaust System using Ammonia Gas to Provide Data for Validation of a CFD Model' Awaiting Publication.
5	Benjamin, S.F Roberts, C.A. (2003) 'Automotive Catalyst Warm-Up to Light-Off by pulsating Engine Exhaust' International Journal of Engine Research (v.5) 125-147
6	Benjamin, S.F. Roberts, C.A. (2007) 'The Porous Medium Approach to CFD Modelling of SCR with Injection of Urea Droplets' Pro IMechE Conference (C66/047) 143-159.
7	Benjamin, S.F. Roberts, C.A. (2007) 'Three-Dimensional Modelling of NO_x and Particulate Traps Using CFD: A Porous Medium Approach' Applied Mathematical Modelling (v.31) 2446-2460.
8	Blakeman, P.G. Chandler, G.R. John, G.R Wilkins, A.J.J. (2001) 'Investigations into NO_x Aftertreatment with Urea SCR for Light-Duty Diesel Vehicles' SAE 2001-01-3624.
9	Blue Motion (2008) 'Blue Motion II and Blue TDI' [Online] Available from <www.bluemotion.me> [18th November 2008]
10	Cataler (n.d.) 'Automotive Catalysts' [Online] Available from <www.cataler.co.jp> [27th July 2011]
11	Chatterjee, D. Burkhardt, T. Bandl-Konrad, B. Braun, T. Tronconi, E. Nova, I. Ciardelli, C. (2005) 'Numerical Simulation of Ammonia SCR Catalytic Converters: Model Development and Application' SAE 2005-10-0965.
12	Chatterjee, D. Burkhardt, T. Weibel, M. Nova, I. Grossale, A. Tronconi, E. (2007) 'Numerical Simulation of Zeolite and V-Based SCR Catalytic Converters' SAE 2007-01-1136.
13	Chatterjee, D. Burkhardt, T. Rappe, T. Guthenke, A. Weibel, M. (2008) 'Numerical Simulation of DOC+DPF+SCR Systems: DOC Influence on SCR Performance' SAE 2008-01-0867.

Reference Number	Reference
14	Chen, J.P. Hausladen, M.C. Yang, R.T. (1995) 'Delaminated Fe_2O_3–Pillared Clay: Its Preparation, Characterisation, and Activities for Selective Catalytic Reduction of NO by NH_3' Journal of Catalysis (v.151) 135-146.
15	Chi, J.N. Dacosta, H.F.M. (2005) 'Modelling and Control of a Urea-SCR Aftertreatment System' SAE 2005-01-0966.
16	Ciardelli, C. Nova, I. Tronconi, E. Konrad, B. Chatterjee, D. Ecke, K. Weibel, M. (2004) 'SCR-De NO_x for Diesel Engine Exhaust Aftertreatment: Unsteady-State Kinetic Study and Monolith Reactor Modelling' Chemical Engineering Science (v.59) 5301-5309
17	Ciardelli, C. Nova, I. Tronconi, E. Chatterjee, D. Bandl-Konrad, B. (2004) 'A "Nitrate Route" for the Low Temperature "Fast SCR" Reaction Over a V_2O_5-WO_3/TiO_2 Commercial Catalyst' ChemComm 2718-2719.
18	Ciardelli, C. Nova, I. Tronconi, E. Chatterjee, D. Bandl-Konrad, B. Weibel, M. Krutzsch, B. (2007) 'Reactivity of NO/NO_2-NH_3 SCR System for Diesel Exhaust Aftertreatment: Identification of the Reaction Network as a Function of Temperature and NO_2 Feed Content' Applied Catalysis (v.70) 80-90.
19	Colombo, M. Nova, I. Tronconi, E. (2010) 'A Comparative Study of the NH_3-SCR Reactions over a Cu-Zeolite and a Fe-Zeolite Catalyst' Catalysis Today (v.151) 223-230
20	Day, E.G.W. (2001) 'An Experimental and Theoretical Investigation of Heat Transfer in Automotive Exhaust Catalysts' PhD Thesis, Coventry University.
21	Dennis, A.J. Garner, C.P. Taylor, D.H.C. (1999) 'The Effect of EGR on Diesel Engine Wear' SAE 1999-010839
22	Diesel Net (2007) 'Cars and Light-Duty Trucks – Tier 1' [Online] Available from <www.dieselnet.com> [April 2007].
23	Diesel Net (2007) 'Cars and Light-Duty Trucks – Tier 2' [Online] Available from <www.dieselnet.com> [April 2007].
24	Diesel Net (2007) 'Cars and Light-Duty Trucks – California' [Online] Available from <www.dieselnet.com> [December 2006].
25	Diesel Net (2007) 'Cars and Light Trucks' [Online] Available from <www.dieselnet.com> [July 2007].
26	Diesel Net (2007) 'On-Road Vehicles and Engines' [Online] Available from <www.dieselnet.com> [May 2007].
27	Diesel Net (2011) 'China: On-Road Vehicles and Engines' [Online] Available from <www.dieselnet.com> [10th August 2011].
28	Diesel Net (2009) 'India: On-Road Vehicles and Engines' [Online] Available from <www.dieselnet.com> [10th August 2011].
29	Diesel Net (2002) 'Diesel Particulate Matter' [Online] Available from <www.dieselnet.com> [November 2002].

Reference Number	Reference
30	Disdale, W. (2007) 'An Experimental and Computational Investigation of the Time Dependency of Automotive Ctalyst Deactivation' PhD Thesis, Coventry University.
31	Electropaedia (2005) 'Battery and Energy Technologies' [Online} Available from <www.mpoweruk.com> [d.c.]
32	Forzatti, P. Nova, I. Tronconi, E. (2010) 'Removal of NO_x from Diesel Exhausts: The New "Enhanced NH_3 -SCR" Reaction' SAE 2010-01-1181.
33	Gieshoff, J. Pfeifer, M. Schafer-Sindlinger, A. Spurk, P.C. Garr, G. Leprince, T. Crocker, M. (2001) 'Advanced Urea SCR Catalysts for Automotive Applications' SAE 2001-01-0514.
34	Girard, J. Snow, R. Cavataio, G. Lambert, C. (2007) 'The Influence of Ammonia to NO_x Ratio on SCR Performance' SAE 2007-01-1581.
35	Green Car Congress (2007) 'Prius Certified to Japanese 2015 Fuel Economy Standards with JC08 Test Cycle' [Online] Available from <www.grrencarcongress.com> [11th August 2007]
36	Grossale, A. Nova, I. Tronconi, E. (2009) 'Ammonia Blocking of the Fast SCR Reactivity over a Commercial Fe-Zeolite Catalyst for Diesel Exhaust After-Treatment' Journal of Catalysis (v.265) 141-147
37	Hamada, I. Kato, Y. Imada, N. Kikkawa, K. Yamada, A. (2005) 'A Unique Titania-Based SCR NO_x Catalyst for Diesel Exhaust Emission Control' SAE 2005-01-1859.
38	Hawley, J.G. Wallace, F.J. Cox, A. Horrocks, R.W. Bird, G.L. (1999) 'Reduction of Steady-State NO_x Levels from an Automotive Diesel Engine Using Optimised VGT/EGR Schedules' SAE 1999-01-0835
39	Health & Safety Executive (1999) 'Control of Diesel Engine Exhaust Emissions in the Workplace' HSE Books.
40	Hou, X. Epling, W.S. Schmieg, S.J. Li, W. (2011) 'Cu-Zeolite SCR Catalyst Thermal Deactivation Studied with FTIR Spatial Resolution' SAE 2011-01-1138.
41	Kaneko, Y. Kobayashi, H. Komagome, R. (1975) 'The Effects of Exhaust Gas Recirculation and Residual Gas on Engine Emissions and Fuel Economy' SAE 750414.
42	Khair, M. Lemaire, J. Fischer, S. (2000) 'Integration of Exhaust Gas Recirculation, Selective Catalytic Reduction, Diesel Particulate Filters, and Fuel-Borne Catalyst for NO_x/PM Reduction' SAE 2000-01-1933
43	Kim, J. Y. Cavataio, G. Patterson, J.E. Laing, P.M. Lambert, C.K. (2007) 'Laboratory Studies and Mathematical Modelling of Urea SCR Catalyst Performance' SAE 2007-01-1573.
44	Koebel, M. Elsener, M. Kleemann, M. (2000) Urea-SCR a Promising Technique to Reduce NO_x Emissions from Diesel Engines' Catalysis Today (v.59) 335-345.
45	Koebel, M. Madia, G. Raimondi, F. Wokaun, A. (2002) 'Enhanced Reoxidation of Vanadia by NO_2 in the Fast SCR Reaction' Journal of Catalysis (v.209) 159-165.

Reference Number	Reference
46	Kowatari, T. Hamada, Y. Amou, K. Hamada, I. Funabashi, H. Takakura, T. Nakagome, K. (2006) 'A Study of a New Aftertreatment System (1): A New Dosing Device for Enhancing Low Temperature Performance of Urea-SCR' SAE 2006-01-0642.
47	Kustov, A.L. Hansen, T.W. Kustova, M. Christensen, C.H. (2007) 'Selective Catalytic Reduction of NO by Ammonia Using Mesoporous Fe-Containing HZSM-5 and HZSM-12 Zeolite Catalysts: An Option for Automotive Applications' Applied Catalysis B: Environmental (v.76) 311-319.
48	Lenz, H.P. Cozzarini, C. (1999) 'Emissions and Air Quality' Society of Automotive Engineers Inc., Warrendale Pennsylvania.
49	Luo, J.-Y. Hou, X.-X. Wijayakoon, P. Schmieg, S.J. Epling, W.S. (2010) 'Spatially Resolving SCR Reactions over a Fe/Zeolite Catalyst' (v.102) Applied Catalyssi B: Environmental 110-119.
50	Maunula, T. Matilainen, P. Louhelainen, M. Juvonen, P. Kinnuen, T. (2007) 'Catalysed Particulate Filters for mobile Diesel Applications' SAE 2007-01-0041.
51	McGrath, J.J. Barnes, C.D. (1982) 'Air Pollution – Physiological Effects' Academic Press (A Subsidiary of Harcourt Brace Jovanovich, Publishers).
52	Miller, L. (1995) 'Nitric Oxide Therapy for Persistent Pulmonary Hypertension of the Newborn' Neonatal Network (v.14) 9-15.
53	Nakayama, R. Watanabe, T. Takada, K. Odaka, M. Kusaka, J. Daisho, Y. (2006) 'Control Strategy for Urea-SCR System in Single Step Load Transition' SAE 2006-01-3308.
54	Narayanaswamy, K. He, Y. (2008) 'Modelling of Copper-Zeolite and Iron Zeolite Selective Catalytic Reduction (SCR) Catalysts at Steady State and Transient Conditions' SAE 2008-01-0615.
55	Nishioka, A. Sukegawa, Y. Katogi, K. Hamada, H. Kowatari, T. Mukai, T. Yokota, H. (2006) 'A Study of a New After Treatment System (2): Control of Urea Solution Spray for Urea-SCR' SAE 2006-01-0644.
56	Nishioka, A. Amou, K. Yokota, H. Murakami, T. (2008) 'A Urea-Dosing Device for Enhancing Low-Temperature Performance by Active-Ammonia Production in an SCR System' SAE 2008-01-1026.
57	Olsson, L. Sjovall, H. Blint, R. (2008) 'A Kinetic Model for Ammonia Selective Catalytic Reduction Over CuZSM-5' Applied Catalysis B: Environmental (v.81) 203-217.
58	Oesterle, J.J. Calvo, S. Damson, B. Feyl, G. Neumann, F. Rudelt, J. (2008) 'Urea Systems in Focus – New Challenges and Solutions in the Development of Car and Commercial Vehicle Exhaust Systems. SAE 2008-01-1186.
59	Pundir, B.P. (2007) 'Engine Emissions' Alpha Science International Ltd, Oxford, UK.
60	Road Transport (2008) 'Big Lorry Blog' [Online] Available from <www.roadtransport.com> [15th February 2008].

Reference Number	Reference
61	Saito, S. Shinozaki, R. Suzuki, A. Jyoutaki, H. Takeda, Y. (2003) 'Development of Urea-SCR System for Commercial Vehicle – Basic Characteristics and Improvement of NO_x Conversion at Low Load Operation' SAE 2003-01-3248.
62	Saito, S. Shinozaki, R. Suzuki, A. Jyoutaki, H. Takeda, Y. (2003) 'Development of Urea-SCR System for Commercial Vehicle – Basic Characteristics and Improvement of NO_x Conversion at Low Load Operation' SAE 2003-01-3248.
63	Servati, H. Petreanu, S. Marshall, S. Su, H. Marshall, R. Attarsyedi, S. Wu, C-H. Hughes, K. Simons, L. Berrimann, L. Zabsky, J. Gomulka, T. Rinaldi, F. Tynan, M. Salem, J. Joyner, J. (2005) 'A NO_x Reduction Solution for Retrofit Applications: A Simple Urea SCR Technology' SAE 2005-01-1857.
64	Shah, R.K. London, A.L. (1978) 'Laminar Flow Forced Convection in Ducts' Academic Press
65	Shah, S.D. Mauti, A. Richert, J.F.O. Loos, M.J. Chase, R.E. (2007) 'Measuring NO_x in the Presence of Ammonia' SAE 2007-01-0331
66	Shibata, M. Nagata, H. Takeshima, S. Hoshino, K. (2007) 'A Study of Engine Oil Composition Effects on Zeolite-Type SCR Catalyst Durability' SAE 2007-01-1924.
67	Sjövall, H. Blint, R.J. Olsson, L. (2009) 'Deatiled Kinetic Modelling of NH_3 SCR over Cu-ZSM-5 Applied Catalysis B: Environmental (v.92) 138-153
68	CD-adapco (2010) 'STAR-CD Version 4.14.026' [Online] Available online to licence holders only.
69	Sturgess, M.P. Benjamin, S.F. Roberts, C.A. (2010) 'Spatial Conversion Profiles within an SCR in a Test Exhaust System with Injection of Ammonia Gas Modelled in CFD using the Porous Medium Approach' SAE 2010-01-2089
70	Tabata, M. Tsuchida, H. Miyamoto, K. Yoshinari, T. Yamazaki, H. Hamada, H. Kintaichi, Y. Sasaki, M. Ito, T. (1994) 'NO_x Emission Control in Diesel Exhaust over Alumina Catalyst' SAE1994-25-0197.
71	Tamaldin, N. (2010) 'Experimental Investigation of Emissions from a Light-Duty Diesel Engine Utilising Urea Spray SCR System' PhD Thesis, Coventry University.
72	Tamaldin, N. Roberts, C.A. Benjamin, S.F. (2010) 'Experimental Study of SCR in a Light-Duty Diesel Exhaust to Provide Data for Validation of a CFD Model using the Porous Medium Approach' 2010-01-1177.
73	Tennison, P. Lambert, C. Levin, M. (2004) 'NO_x Control Development on a Diesel Passenger Car' SAE 2004-01-1291.
74	The Auto Industrie Blog (2008) '2009 BMW 3-Series Facelift' [Online] Available from <www.theautoindustrieblog.com> (27^{th} july 2011).
75	Theis, J. Gulari, E. (2006) 'A LNT+SCR System for Treating the NO_x Emissions from a Diesel Engine' SAE 2006-01-0210.
76	Tronconi, E. (1997) 'Interaction Between Chemical Kinetics and Transport Phenomena in Monolithic Catalysts' Catalysis Today (v.34) 421-427.

Reference Number	Reference
77	Tronconi, E. Nova, I. Ciardelli, C. Chatterjee, D. Bandl-Konrad, B. (2005) 'Modelling of an SCR Catalytic Converter for Diesel Exhaust After-Treatment: Dynamic Effects at Low Temperature' Catalysis Today (v.105) 529-536.
78	Tronconi, E. Nova, I. Ciardelli, C. Chatterjee, D. Weibel, M. (2007) 'Redox Features in the Catalytic Mechanism of the "Standard" and "Fast" NH_3–SCR of NO_x Over a V-Based Catalyst Investigated by Dynamic Methods' Journal of Catalysis (v.245) 1-10.
79	Volkswagen (N.D.) 'NO_x Exhaust Treatment System' [Online] Available from <www.volkswagen.co.uk> [N.D.].
80	Winkler, C. Florchinger, P. Ratil, M.D. Gieshoff, J. Spurk, P. Pfeifer, M. (2003) 'Modelling of SCR DeNO_x Catalyst – Looking at the Impact of Substrate Attributes' SAE 2003-01-0845.
81	What Car? (N.D.) 'Volkswagen CC Saloon 2.0 TDI 140 Blue Motion Tech 4dr Photos' [Online] Available from <www.whatcar.com> [N.D.].
82	Wurzenberger, J.C. Wanker, R. (2005) 'Multi-Scale SCR Modelling, 1D Kinetic Analysis and 3D System Simulation' SAE 2005-01-0948.
83	Wurzenberger, J.C. Wanker, R. SchuBler, M. (2008) 'Simulation of Exhaust Gas Aftertreatment Systems ~Thermal Behaviour During Different Operating Conditions' SAE 2008-01-0865.
84	York, A.P.E. Watling, T.C. Cox, J.P. Jones, I.Z. Walker, A.P. Blakeman, P.G. Ilkenhans, T. Allansson, R. Lavenius, M. (2004) 'Modelling an Ammonia SCR De NO_x Catalyst: Model Development and Validation' SAE 2004-01-0155.

Appendix 1: Experimental Set-up

Appendix 1.1 EXSA Experimental Set-up

A schematic of the experimental set-up for the Horiba EXSA 1500 is presented in A1.1, and the required gas concentrations are displayed in A1.2.

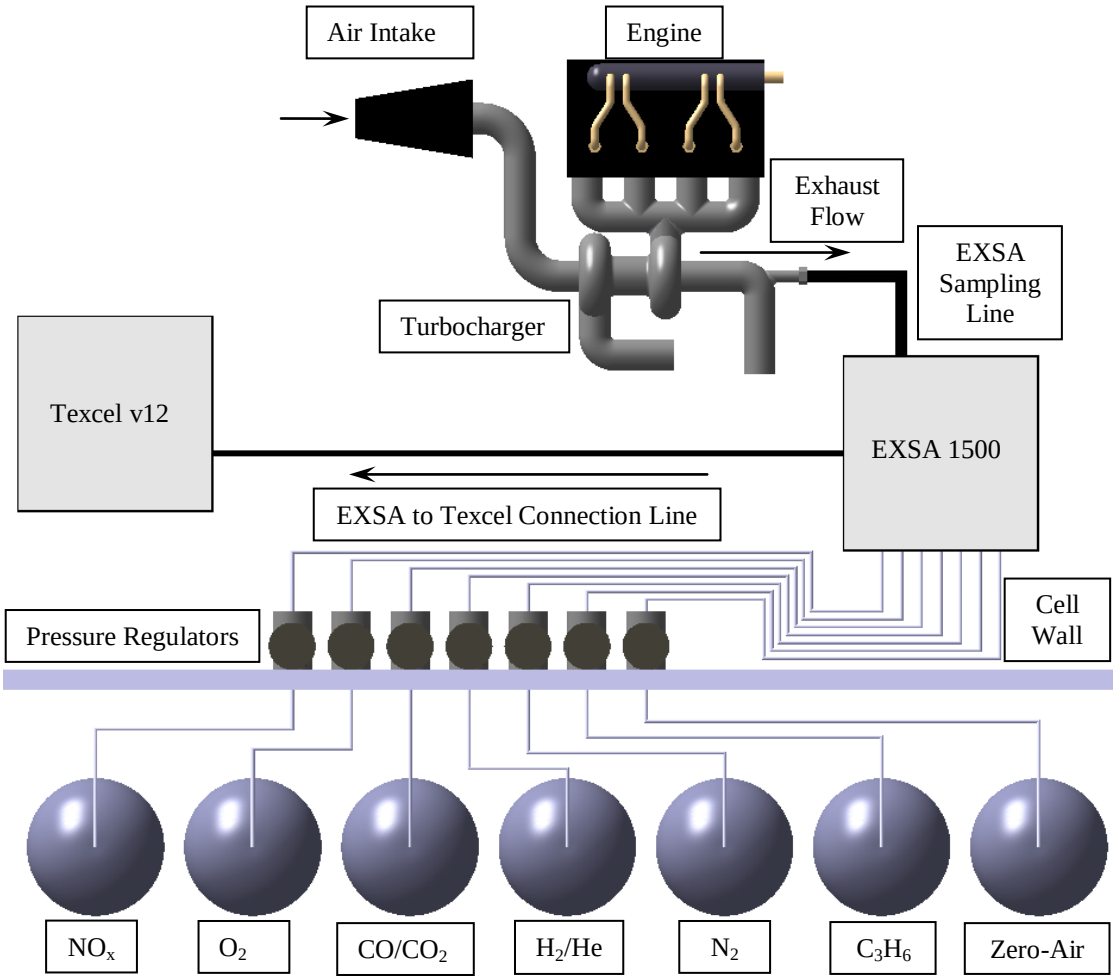

A1.1: EXSA 1500 experimental configuration..

Gas Type	Concentration	Function	Pressure (bar)
NO_x	507ppm NO_x 499ppm NO	Span gas for CLD.	100kPa +/- 10kPa
CO/CO_2	11.85%CO_2 1.9% CO	Span gas for NDIR.	100kPa +/- 10kPa
O_2	99.99% pure O_2	Ozoniser gas.	100kPa +/- 10kPa
H_2/He		Flame ignition gas for FID.	100kPa +/- 10kPa
N_2	99.99% pure N_2	Zeroing gas for all analysers.	100kPa +/- 10kPa
C_3H_6	805ppm (multiply by 3 for analyser concentration)	Span gas for FID.	100kPa +/- 10kPa
Zero-Air	79% N_2 21% O_2	Purge gas for all analysers.	100kPa +/- 10kPa

A1.2: : EXSA required gases.

Appendix 1.2 MEXA Experimental Set-up

A schematic of the experimental set-up for the Horiba MEXA-1170 Nx is presented in A1.3, whilst the required gas concentrations are displayed in A1.4.

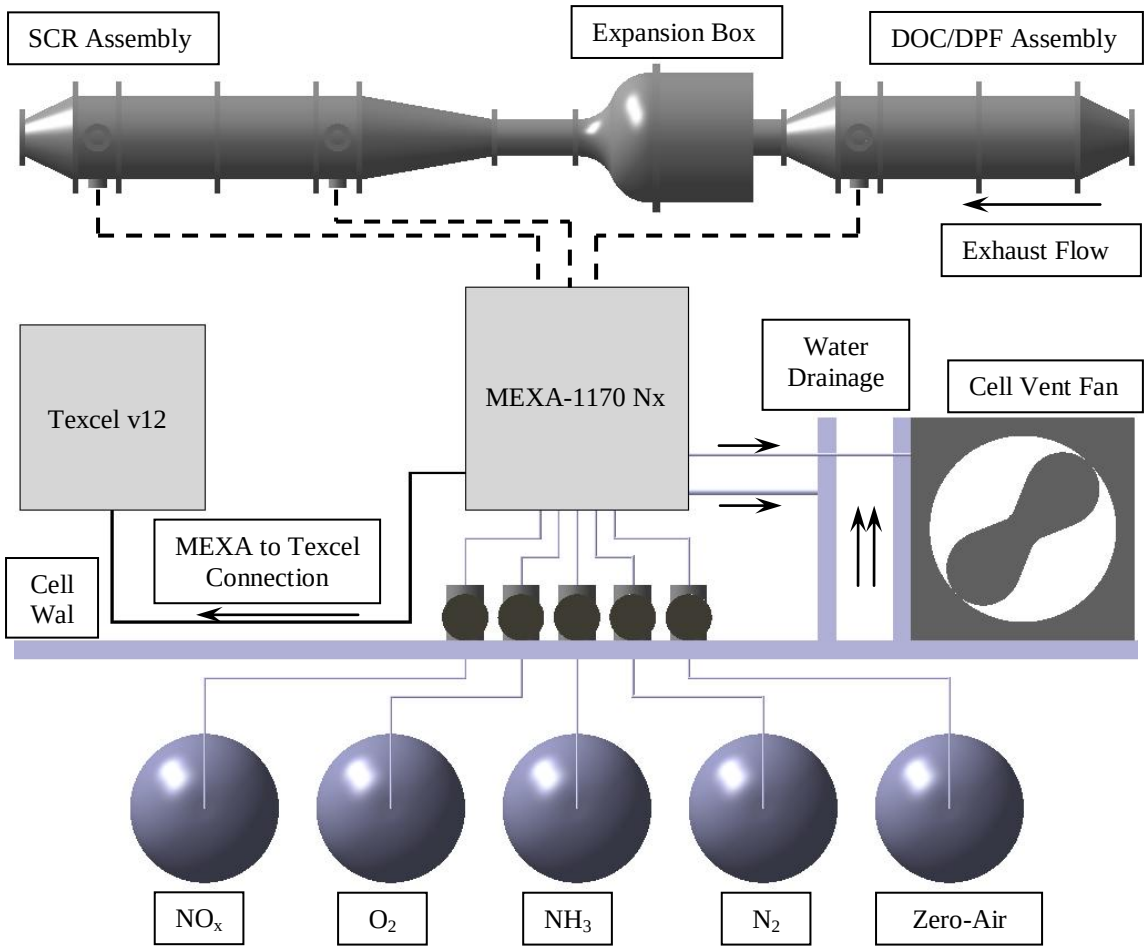

A1.3: MEXA-1170 Nx experimental configuration. The sampling lines, denoted by dashes, were switched between locations manually.

Gas Type	Concentration	Function	Pressure (bar)
NO_x	507ppm NO_x consisting of 499ppm NO in balance-N_2	Span gas.	100kPa +/- 10kPa
O_2	99.99% pure O_2	Ozoniser gas.	100kPa +/- 10kPa
NH_3	95ppm NH_3 in balance-N_2	Span gas.	100kPa +/- 10kPa
N_2	99.99% pure N_2	Zeroing gas.	100kPa +/- 10kPa
Zero-Air	79% N_2 21% O_2	Purge gas.	100kPa +/- 10kPa

A1.4: Gases required for the MEXA.

Appendix 2: CFD Coding and Derivations

Appendix 2.1 Kinetic Parameters

The kinetic parameters sued in this study are displayed in A2.1, and can also be found in the open literature [Olsson et al, 2008]:

A2.1: Reaction rate constants, pre-exponential factors, and activation energies obtained from the literature, which have been used in this study. [Olsson et al, 2008]

The reaction rate constant $k_{3,b}$ is calculated from the thermodynamic restrictions as described in the literature. [Olsson et al, 2008]

The activation energy for ammonia desorption is coverage dependant. The following term is used to describe desorption: $E_{1,b} = E_{1,b}(0)(1 - \alpha_3\theta_{NH3\text{-}S1})$, where $\alpha = 0.98$. [Olsson et al, 2008]

Appendix 2.2 Parameter Initialisation

A2.2 describes the input parameters used in the 'include' file 'para.inc'; this file is for the input parameters that remain constant throughout this study, with the exception being the species input values.

Substrate Properties			
Hydraulic Diameter	0.86mm	Gas Filled Pore Occupation of Wascoat	0.055
Wetted Surface Area Per Unit Volume	2128 $m^2.m^{-3}$	Number of Available Reaction Sites (Ω)	200 – 500 mol-sites.m^{-3}
Nusselt Number	3.608	Porosity Fraction	0.457
	Gas Constant	8.314 $J.mol^{-1}.K^{-1}$	
Mass Transfer Coefficients (Values for 500K shown here)			
	$m.s^{-1}$		
NO	0.209	NH_3	0.199
NO_2	0.165	O_2	0.180
N_2O	0.128	-	-
Diffusivity Coefficients for Air and Washcoat (Values for 838K shown here)			
	$m^2.s^{-1}$		
NO	Air: 0.000143 Washcoat: 0.0000300	NH_3	Air: 0.000136 Washcoat: 0.0000410
NO_2	Air: 0.000113 Washcoat: 0.0000230	O_2	Air: 0.000123 Washcoat: 0.0000349
N_2O	Air: 0.0000877 Washcoat: 0.0000210	-	-
Molecular Mass Ratios			
NO	0.9653	NH_3	1.704
NO_2	0.6296	O_2	0.9050
N_2O	0.658	-	-

A2.3: Input parameters.

The value for the number of available reaction sites (Ω) and the inlet species cocnentrations are entered by the user. Mass transfer and diffusivity coefficients are corrected for temperature as explained in Section 2.2.3.

Appendix 2.3 User-Subroutines

Appendix 2.3.1 Boundary Condition Definition

The inlet values for velocity, temperature, and species concentrations for steady-state and transient analyses are described in this section.

The inlet velocity is calculated via the equation ofcontinuity , where the cross-sectional area of the catalyst, and the mass flow rate are known values. Although only a small cross-section of the catalyst is modelled. The cross-sectional of the experimental catalyst, denoted by A, is used in calculating the inlet velocity. Equation (75) calculates the inlet velocity:

$$U = \frac{\dot{m}}{\rho A} \quad \text{.....} \quad (75)$$

where the cross-sectional area is equal to $0.01m^2$.

Inlet species concentrations for the steady-state analyses are read from 'para.inc', for the transient analyses, however, where the inlet ammonia varies over time, the amount of ammonia injected is subject to the following conditioning:

```
IF (TIME.LT.(33.0 + 300.0)) THEN
 SCALAR(7) = 0.000004
END IF
IF (TIME.GE.(33.0 + 300.0).AND.TIME.LT.(623.0 + 300.0)) THEN
SCALAR(7) = 0.0006657
END IF
IF (TIME.GE.(623.0 + 300.0).AND.TIME.LT.(921.0 + 300.0)) THEN
SCALAR(7) = 0.0005007
END IF
IF (TIME.GE.(921.0 + 300.0).AND.TIME.LT.(1221.0 + 300.0)) THEN
SCALAR(7) = 0.0003328
END IF
IF (TIME.GE.(1221.0 + 300.0).AND.TIME.LT.(2436.0 + 300.0)) THEN
SCALAR(7) = 0.0001661
END IF
IF (TIME.GE.(2436.0 + 300.0).AND.TIME.LT.(2650.0 + 300.0)) THEN
SCALAR(7) = 0.000002
END IF
```

where SCALAR(7) is the scalar number for the gas phase ammonia.

Due to STAR CD version 4 being unable to initialise the substrate temperatures an initial warm-up time of 300 seconds was included to heat up the substrate to the gas temperature; this warm-up time was chosen for short SCR bricks, however, for longer bricks, the warm-up time would need to be increased.

Appendix 2.3.2 Heat Transfer in the Gas Phase

In version 3, the gas phase heat transfer was calculated in the user-subroutine 'sorent.f' in STAR CD version 3, however, in version 4, a separate user-subroutine was developed to handle this, which calculates the heat transfer coefficient in the gas phase based on the Nusselt Number as described in equation (76):

$$U = \frac{Nu}{kD_h} \quad \text{(76)}$$

where k is the thermal conductivity of air; this is calculated in equation (77) to account for its temperature dependence:

$$k = 0.0000589\ T_{Mean} + 0.010103 \quad \text{(77)}$$

The mean temperature, or T_{Mean} (K), is calculated via the thin film approximation, or the mean value of the substrate and the gas temperature.

The following coding is used to multiply the heat transfer coefficient by the appropriate elevation ratios to account for developing flow at the entrance of the brick, which are modified depending on mesh density:

```
ZZCEL = cx(3,i)
IF (ZZCEL.GT.(0.030).AND.ZZCEL.LE.0.034) THEN
HHH = 1.85*HHH
ELSE IF (ZZCEL.GT.(0.034).AND.ZZCEL.LE.0.038) THEN
HHH = 1.35*HHH
ELSE IF (ZZCEL.GT.(0.038).AND.ZZCEL.LE.0.042) THEN
HHH = 1.25*HHH
ELSE IF (ZZCEL.GT.(0.042).AND.ZZCEL.LE.0.046) THEN
HHH = 1.18*HHH
ELSE IF (ZZCEL.GT.(0.046).AND.ZZCEL.LE.0.050) THEN
HHH = 1.15*HHH
ELSE IF (ZZCEL.GT.(0.050).AND.ZZCEL.LE.0.054) THEN
HHH = 1.11*HHH
ELSE
HHH = 1.0
END IF
```

Appendix 2.3.3 Mass Transfer

Species concentrations in the solid phase, as well as the conversion of species are discussed in this section.

Equations (78) and (79) describe the conversion of species mass fraction into mol fraction, and the conversion of mol fraction into mol.m^{-3} respectively:

$$C_{i,mol-frac} = C_{i,mass-frac} \times \omega_i \quad \text{(78)}$$

where ω_i is the species molecular mass ratio.

$$C_{i,mol/m3} = \frac{C_{i,mol-frac} \times 273}{0.0224 T_{Mean}} \quad \text{(79)}$$

The calculation of the species concentration in mol.m^{-3} is based on Avogadros' Gas Law, which states that 1mol of any gas occupies approximately 22.4 litres at standard temperature and pressure.

The diffusion coefficients for the gas and the substrate are also corrected for temperature by using the multiplier: $\left[\frac{T_{Mean}}{838}\right]^{\Lambda}$, where Λ = 1.75 and 1.4 for the gas and the washcoat respectively. These are then combined to provide a bulk mass transfer coefficient that takes into account the depth of the washcoat, which is approximately 10 microns:

$$K_{bulk} = \left[\frac{KD}{D + KTh \times 0.00001}\right] \quad \text{(80)}$$

Developing flow is also accounted for in the same way as described in Appendix 2.3.2. Equations (81) and (85) describe the mass transfer in the gas phase and the substrate respectively that are input into 'sorsca.f':

$$Q_{Gas} = K_{bulk} \rho_{air} A_V C_{i-solid} - K_{bulk} \rho_{air} A_V C_{i-gas} \quad \text{(81)}$$

where $C_{i\text{-}solid}$ is the species concentration in the solid phase.

$$Q_{Solid} = \left[\frac{\varepsilon}{V_w}\right] \left(K_{bulk} \rho_{air} A_V C_{i-gas} + \rho_i r_{i-prod} \right) - \left(K_{bulk} \rho_{air} A_V C_{i-solid} + \rho_i r_{i-cons} \right) \quad \text{(82)}$$

where $C_{i\text{-}gas}$ is the species concentration in the gas phase, and $R_{i\text{-}prod}$ and $R_{i\text{-}cons}$, in mol.mol-sites^{-1}.s^{-1}, are the reaction rates for the production and consumption of species i.

Appendix 2.4 Mass Transfer and Diffusivity Combination

The combination of mass transfer in the gas phase and diffusivity on the washcoat [Disdale, 2007] is described in this section. The species transport is illustrated in A2.4:

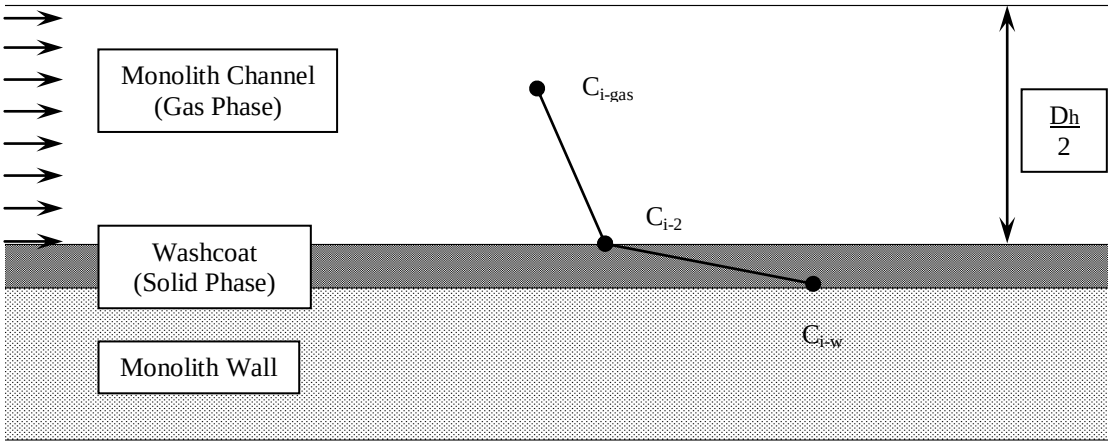

A2.4: Diagram showing half of a monolith channel. $C_{i\text{-}gas}$, $C_{i\text{-}2}$, and $C_{i\text{-}W}$ are the species concentrations (mol-fraction) in the gas phase, on the washcoat surface, and on the monolith wall respectively.

Equation (83) and equation (84) describe the mass transfer in the gas phase and diffusion in the washcoat respectively:

$$q_1 = K\rho_{i-gas}\left(C_{i-gas} - C_{i-2}\right) \quad (83)$$

$$q_2 = \frac{D}{Th}\rho_{i-gas}\left(C_{i-2} - C_{i-W}\right) \quad (84)$$

where the thickness of the washcoat, denoted by T_h, is taken into account when dealing with the washcoat. Continuity of mass mass transfer between the gas and the washcoat is assumed to take place, therefore:

$$q_{Total} = q_1 = q_2 \quad (85)$$

$$q_{Total} = K\rho_{i-gas}\left(C_{i-gas} - C_{i-2}\right) = \left[\frac{D}{Th}\right]\rho_{i-gas}\left(C_{i-2} - C_{i-W}\right) \quad (86)$$

Adding $(C_{i\text{-}gas} - C_{i\text{-}2})$ and $(C_{i\text{-}2} - C_{i\text{-}W})$ and then re-arranging gives:

$$q_{Total} = \left[\frac{KD}{D + KTh}\right]\rho_{i-gas}\left(C_{i-gas} - C_{i-W}\right) \quad (87)$$

where:

$$K_{bulk} = \left[\frac{KD}{D + KTh}\right] \quad (88)$$

Appendix 2.5 Accounting for Developing Flow

Developing flow must be accounted for in both heat and mass transfer as the catalyst brick is quite short. The adjusted Nusselt Numbers for a rectangular duct were obtained from open literature [Shah, 1978].

A2.5 and A2.6 describe the input parameters used in the calculation of the elevation ratios, and the elevation ratios in tabular form respectively.

Cp	k_{Gas}	ρ	Dh	ε	$\dot{m}$	$\dot{V}$	U	Uc
$kJ.kg^{-1}.K^{-1}$	$W.m^{-1}.K^{-1}$	$kg.m^{-3}$	m		$kg.s^{-1}$	$m^{-3}.s^{-1}$	$m.s^{-1}$	$m.s^{-1}$
1055	0.0466	0.588	0.001	0.7	0.03	0.051	4.66	6.66

A2.5: Input parameters for air entering a square or rectangular duct at 600K.

1/x*	Nusselt Number	z Co-ordinate (z)	Elevation Ratio
		mm	
0	3.61	-	-
5	3.91	30.14	1.083
10	4.18	15.07	1.159
20	4.66	7.54	1.292
30	5.07	5.02	1.405
40	5.47	3.77	1.516
50	5.83	3.01	1.616
60	6.14	2.51	1.702
80	6.80	1.88	1.885
100	7.38	1.51	2.045
120	7.90	1.26	2.190
140	8.38	1.08	2.323
160	8.84	0.94	2.450
180	9.28	0.84	2.572
200	9.69	0.75	2.686

A2.6: Elevation ratios and the length along the monolith.

FThe Nusselt Number for fully developed laminar-flow along a rectangular duct is 3.608, the elevation ratio for deloping flow is the Nusselt Number at the location 1/x* divided by the Nusselt Number for fully developed flow.

Equation (92) calculates the z co-ordinate along the monolith that corresponds to the value of the elevation ratio, where z, in metres, is the z co-ordinate:

$$z = \frac{D_h^2 U_C C_P}{k\left[\frac{1}{x*}\right]} \quad \text{(89)}$$

Appendix 2.6 Model Calibration

The CFD model was calibrated against data from the same literature in which the model expressions and kinetics were obtained. Gas inlet concentrations used in these analyses are described in the literature, for simplicity, only the steady-state concentrations are considered. [Olsson et al, 2008] A2.7 and A2.8 plot the steady-state species cocnentations obtained by the CFD model:

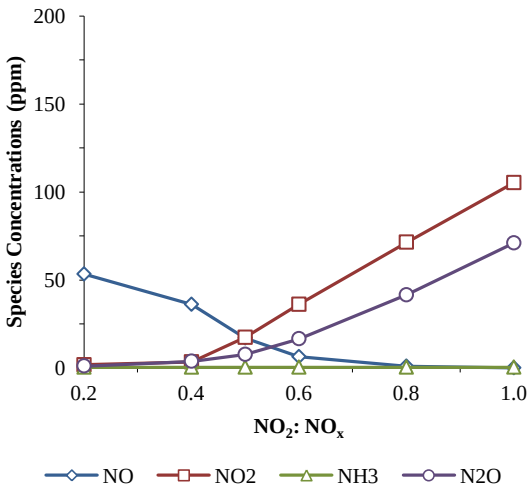

A2.7: Steady-state species concentrations plotted against the inlet NO_2: NO_x ratio when T = 350°C.

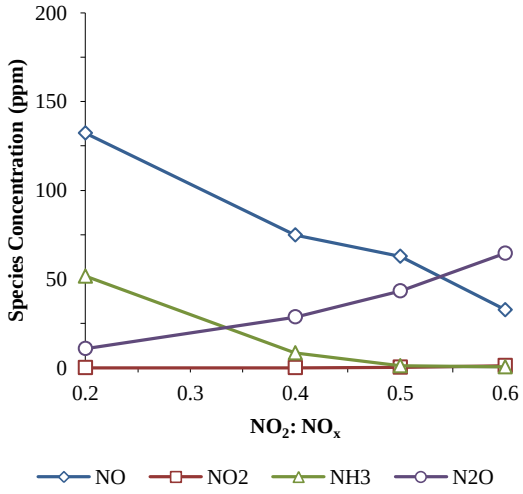

A2.8: Steady-sate species concentrations plotted against the inlet NO_2: NO_x ratio when T = 175°C.

A2.9 and A2.10 plot the species concentration profiles for the same analyses as undertaken by Chalmers University for A2.7 and A2.8 respectively:

A2.9: Species concentrations for different NO_2: NO_x ratios when T = 350°C. [Olsson et al, 2008]

A2.10: Species concentrations for different NO_2: NO_x ratios when T = 175°C. [Olsson et al, 2008]

Appendix 2.7 Ammonia Adsorption Rate Modification Derivation

The derivation for the ammonia adsorption rate modifications, described in Section 8.1, are presented in this section. A2.11 displays a comparison between ammonia species concentrations between the CFD and experimental data at 30mm along the catalyst brick.

α_1	Inlet Ammonia		Ammonia Consumed (Engine Tests)		Ammonia Consumed (CFD Analyses)		Ratio
	ppm	MF	ppm	MF	ppm	MF	
0.5	298	0.000175	241	0.000141	99	0.000058	2.4
1.0	596	0.000350	317	0.000317	192	0.000113	1.7
1.5	895	0.000525	289	0.000289	272	0.000160	1.1
2.0	1134	0.000666	263	0.000263	333	0.000195	0.8

A2.11: Ammonia consumption ratios for experimental and CFD data at 30mm.

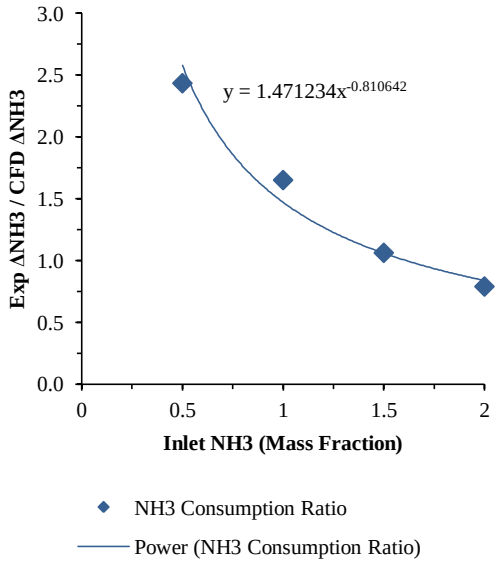

A2.12: $\Delta NH_{3\text{-}Exp}$: $\Delta NH_{3\text{-}CFD}$ ratio at 30mm.

The ratios described in the far right column of A2.11 are plotted in A2.12, where the equation of the line was input into the ammonia adsorption rate in the model.

Appendix 3: Engine Test Data

Appendix 3.1 Engine NO_x Maps

The results of the engine NO_x maps are presented in this section. A3.1 and A3.2 display the NO_x, NO, and NO_2 concentrations when the DOC can was placed upstream and downstream of the DPF respectively.

Analysis	1 DOC Upstream of DPF			2 DOCs Upstream of DPF		
BMEP	3	6	9	3	6	9
EXSA 1500 NO_x	281	567	811	283	571	818
MEXA-1170 NO_x	264	550	772	273	546	770
MEXA-1170 NO	254	397	502	148	140	278
MEXA-1170 NO_2	10	153	270	125	406	492

A3.1: NO_x, NO, and NO_2 concentrations when the DOC(s) are positioned upstream of the DPF.

Analysis	1 DOC Downstream of DPF			2 DOCs Downstream of DPF		
BMEP	3	6	9	3	6	9
EXSA 1500 NO_x	N/A	N/A	N/A	N/A	N/A	N/A
MEXA-1170 NO_x	275	550	772	286	586	850
MEXA-1170 NO	260	314	470	145	108	213
MEXA-1170 NO_2	15	236	302	141	478	637

A3.2: NO_x, NO, and NO_2 concentrations when the DOC(s) are positioned downstream of the DPF.

The perdiodic logs for the NO_x maps undertaken in this study areplotted in A3.3, A3.5, A3.6, and A3.7, whilst A4.4 describes the test procedure used.

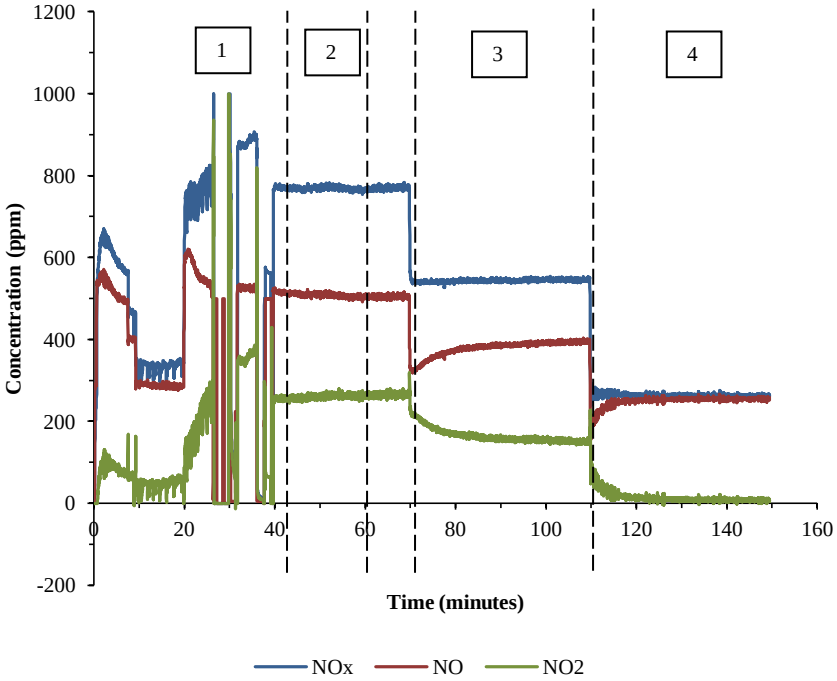

A3.3: Periodic log for test with 1 DOC upstream of the DPF.

Stage Number	Description
1	Engine warm-up stage at 1500rpm, 9bar BMEP
2	Sampling stage at 1500rpm, 9bar BMEP
3	Sampling stage at 1500rpm, 6bar BMEP
4	Sampling stage at 1500rpm, 3bar BMEP

A3.4: Test description. The MEXA was positioned in the instrumentation module downstream of the DOC/DPF assembly. Warm-up times and sampling times remained constant thoughout the NO_x map studies.

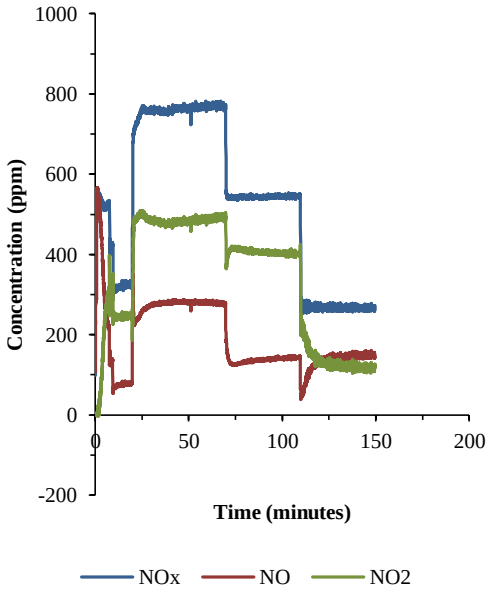

A3.5: Periodic log data for test with 2 DOCs upstream of the DPF.

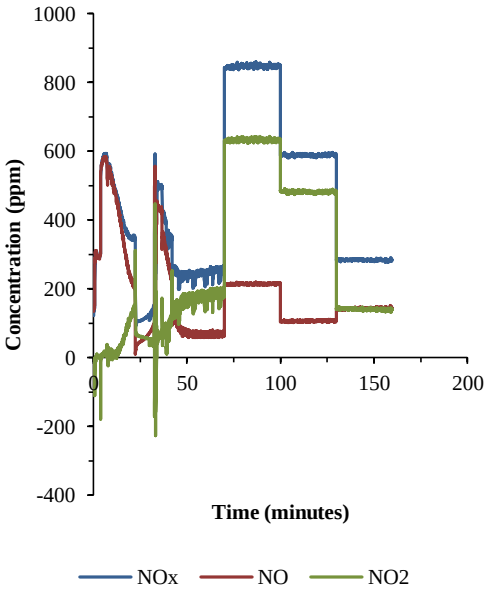

A3.6: Periodic log data for test with 2 DOCs doesntream of the DPF

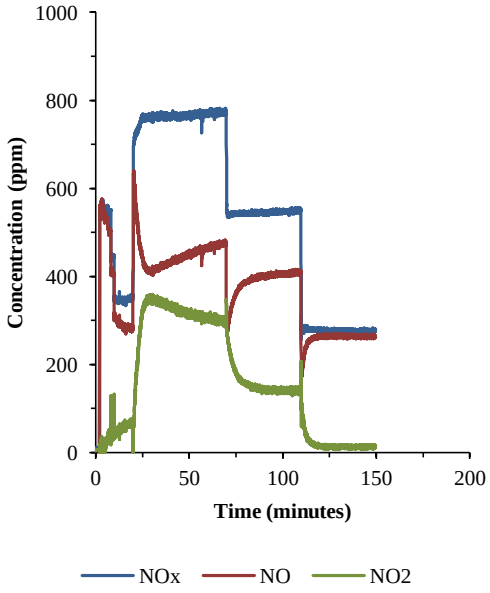

A3.7: Periodic log data for test with 1 DOC downstream of the DPF.

Appendix 3.2

The species concentrations for the steady-state gas tests using 5% ammonia gas in balance-nitrogen are presented in A3.7. Following a discussion with the South West Research Institute regarding the possibility of ammonia oxidation on the NO_x converter catalyst, these values were not corrected using the method described in previous work. [Tamaldin et al, 2010]

Length (mm)	α_1	0.0	30.5	45.5	60.7	76.0	91.0	121.5	136.5	167.0	182.0
					Gas Temperatures (°C)						
Cell Air		16.0	16.0	13.8	17.6	13.0	15.5	15.4	17.0	19.0	18.1
Engine In		9.1	9.1	7.9	9.8	7.3	8.4	9.0	9.9	11.4	12.3
Point 1		283.4	283.4	282.9	285.6	283.2	285.4	279.2	281.7	285.8	291.9
Point 2		260.8	260.8	259.8	261.8	259.8	262.0	257.4	259.3	262.8	267.0
Point 3		214.8	214.8	213.4	213.9	213.6	215.7	212.5	213.9	216.9	218.3
O2 (%)		11.1	11.1	11.4	11.6	11.2	11.3	11.8	11.7	11.7	11.1
	α_1				SCR Inlet Concentrations (ppm)						
NO_x	0.5 1.0 1.5	576	576	580	579	584	576	579	577	577	561
NO	0.5 1.0 1.5	308	308	319	315	316	295	330	329	306	286
NO_2	0.5 1.0 1.5	268	268	261	264	268	281	249	248	271	275
NH_3	0.5 1.0 1.5	279 575 883	279 575 883	291 608 872	262 523 784	296 589 875	283 570 851	285 564 843	276 567 852	274 568 847	271 542 831
NO_2: NO_x		0.47	0.47	0.45	0.46	0.46	0.49	0.43	0.43	0.47	0.49
	α_1				SCR Exit Concentrations (ppm)						
NO_x	0.5 1.0 1.5	576 576 576	353 285 286	316 227 226	336 154 162	308 142 140	314 72 73	317 86 73	317 74 62	301 53 35	297 22 15
NO	0.5 1.0 1.5	308 308 308	228 199 203	215 182 183	204 134 138	206 127 127	200 71 71	217 86 73	225 74 62	193 53 35	180 39 15
NO_2	0.5 1.0 1.5	268 268 268	126 86 83	101 45 43	132 28 26	102 15 13	114 1 2	100 0 0	92 0 0	108 0 0	117 0 0
NH_3	0.5 1.0 1.5	272 594 912	31 277 623	14 250 542	8 111 428	0 128 455	4 38 351	0 34 342	0 31 354	0 11 308	3 0 280

A3.8: Steady-State Upstream and Downstream NO_x, NO, NO_2, and ammonia concentrations.

Appendix 3.3 Steady-State Gas Tests

Appendix 3.3 comntains the periodic log graphs used in the steady-state and transient gas tests. The engine condition used in the sampling stage was 1500rpm 6bar BMEP.

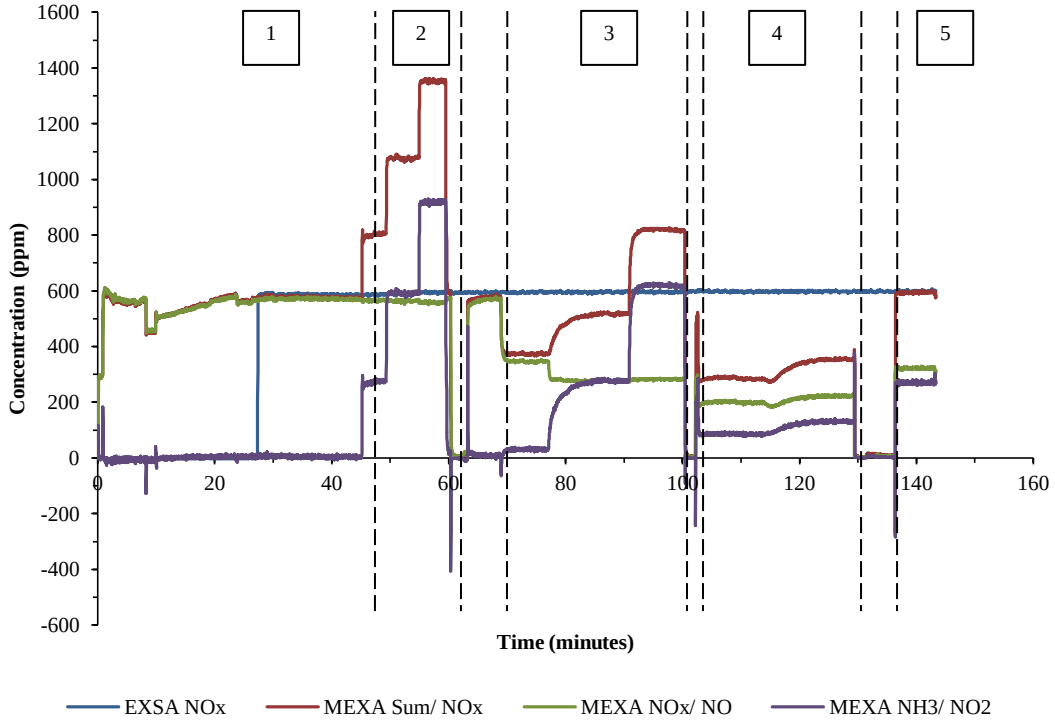

A3.9: Periodic log for the 30mm brick steady-state tests.

The stage numbers are described in A3.9, these are constant for all tests undertaken in this section. Sampling continued for 5 minutes during the gas injection stage, sampling continued for 5 minutes for all values of α.

Stage Number	MEXA Mode	MEXA Position	Gas Injection (α_1)	Description
1	NH_3 Mode	Upstream of SCR	-	Engine warm-up
2	NH_3 Mode	Upstream of SCR	0.5, 1.0, 1.5	Flowmeter setting check, and scrubber check
3	NH_3 Mode	Downstream of SCR	0.5, 1.0, 1.5	First sampling stage
4	NO_2 Mode	Downstream of SCR	1.5, 1.0, 0.5	Second sampling stage
5	NO_2 Mode	Upstream of SCR	-	NO_2: NO_x sampling stage

A3.10: Warm-up and sampling stage descriptions. The gas injection column, refers to α, which is the NH_3: NO_x ratio.

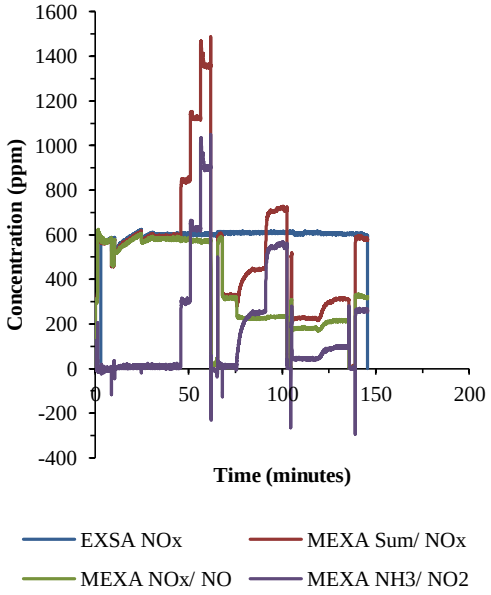

A3.11: Periodic log data for 45.5mm brick steady-state tests.

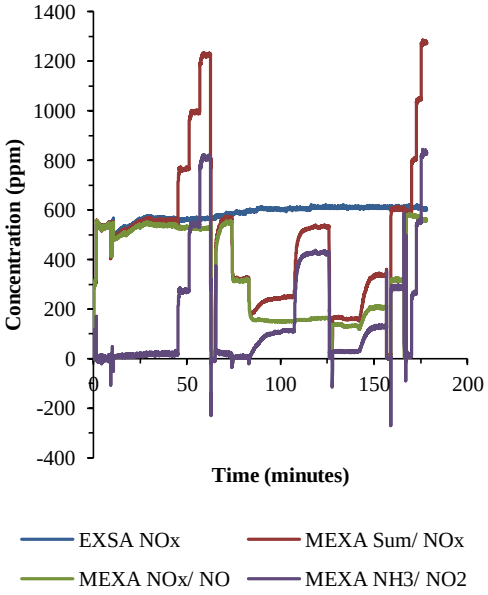

A3.12: Periodic log data for 60mm brick steady-state tests.

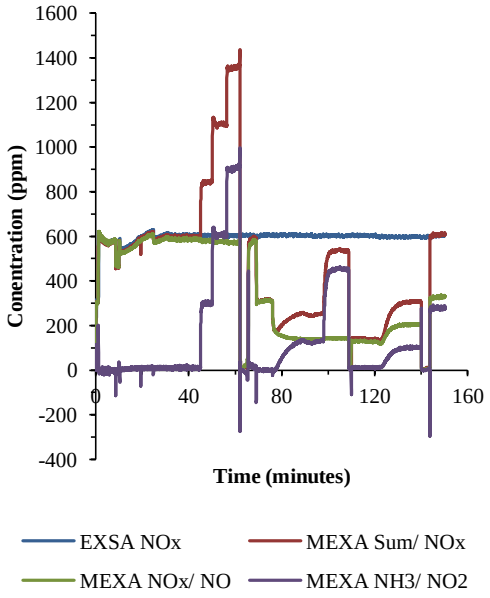

A3.13: Periodic log data for 75.5mm brick steady-state tests.

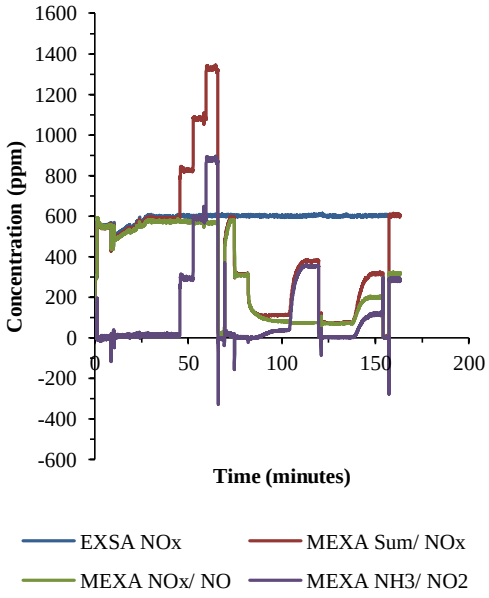

A3.14: Periodic log data for 91mm brick steady-state tests.

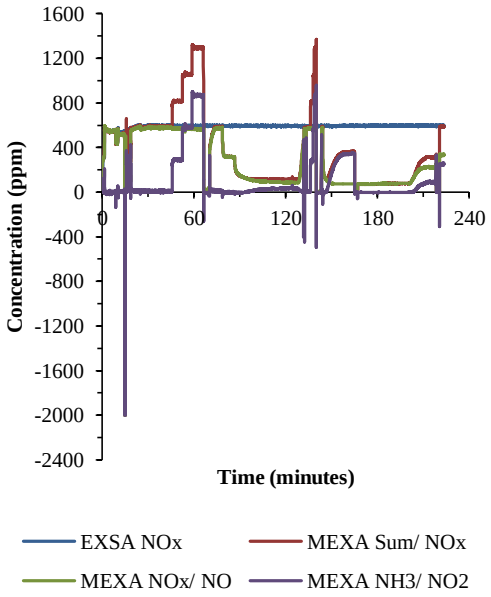

A3.15: Periodic log data for 121mm brick steady-state tests.

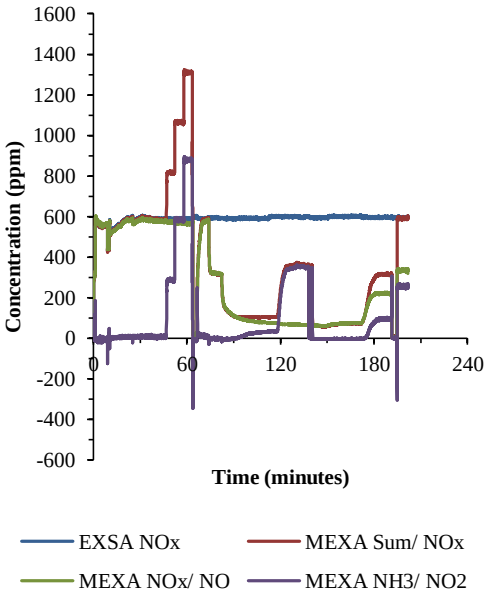

A3.16: Periodic log data for 136.5mm brick steady-state tests.

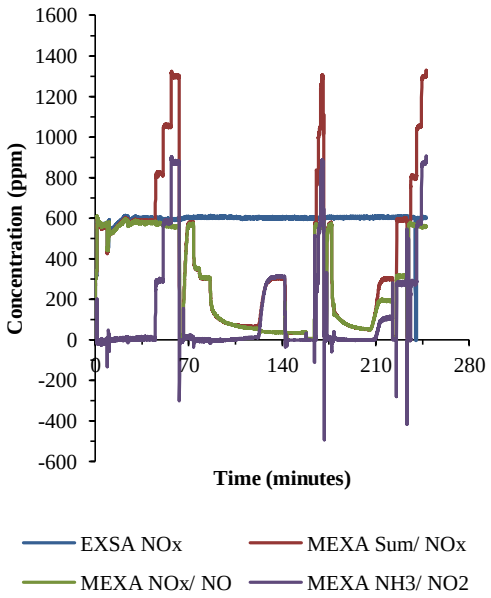

A3.17: Periodic log data for 166.5mm brick steady-state tests.

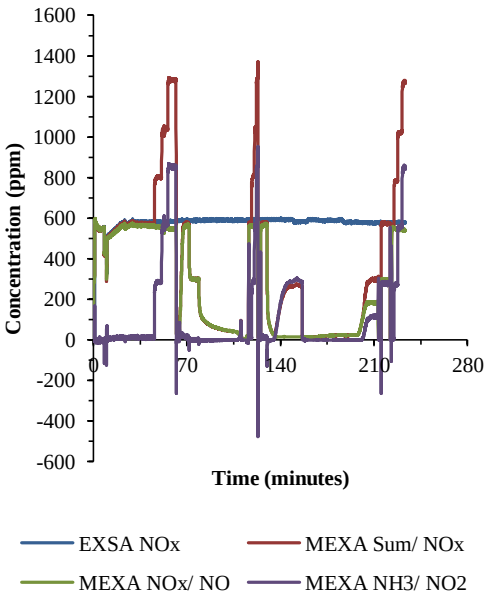

A3.18: Periodic log data for 182mm brick steady-state tests.

Appendix 3.4 Transient Gas Tests

Appendix 3.4 contains the periodic logs used in the transient tests that are described in Chapter 7 of this thesis.

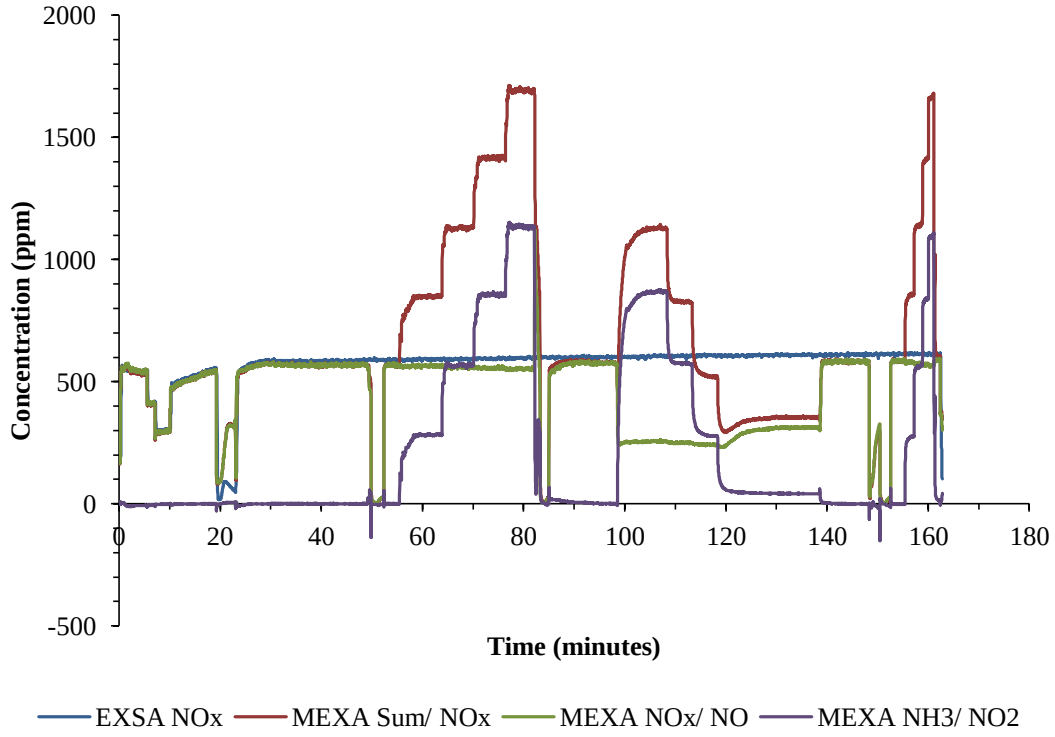

A3.19: Periodic log for the 30mm brick, NO_2: NO_x = 0.60, sampling mode: NH_3 mode.

The measurement strategy is described in A4.15, when the MEXA is in NO_2 in stage 3, the NO_2: NO_x is measured before and after this stage for 5 minutes.

Stage Number	MEXA Mode	MEXA Position	Gas Injection (α_1)	Description
1	NH_3 Mode	Upstream of SCR	-	Engine warm-up
2	NH_3 Mode	Upstream of SCR	0.5, 1.0, 1.5	Flowmeter setting check, and scrubber check
3	NH_3 Mode/ NO_2 Mode	Downstream of SCR	0.5, 1.0, 1.5	Sampling stage
4	NH_3 Mode	Upstream of SCR	0.5, 1.0, 1.5	Scrubber check

A3.20: Warm-up and sampling stage descriptions. The gas injection column refers to α, which is the NH_3: NO_x ratio.

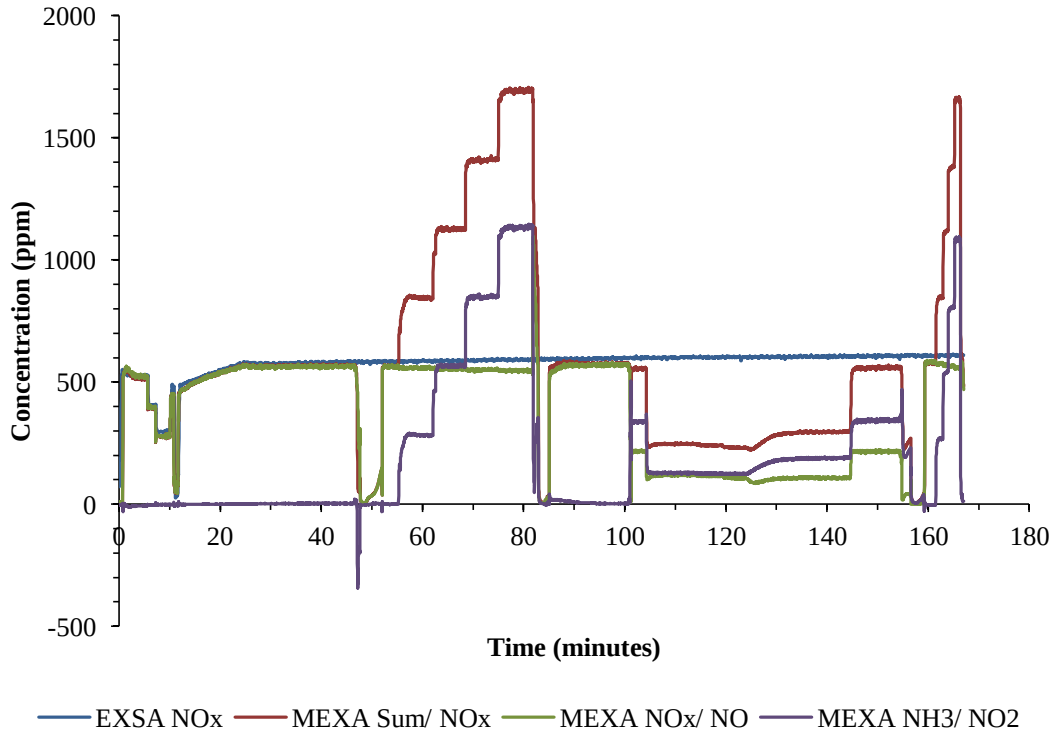

A3.21: Periodic log for the 30mm brick, NO_2: NO_x = 0.60, sampling mode: NO_2 mode.

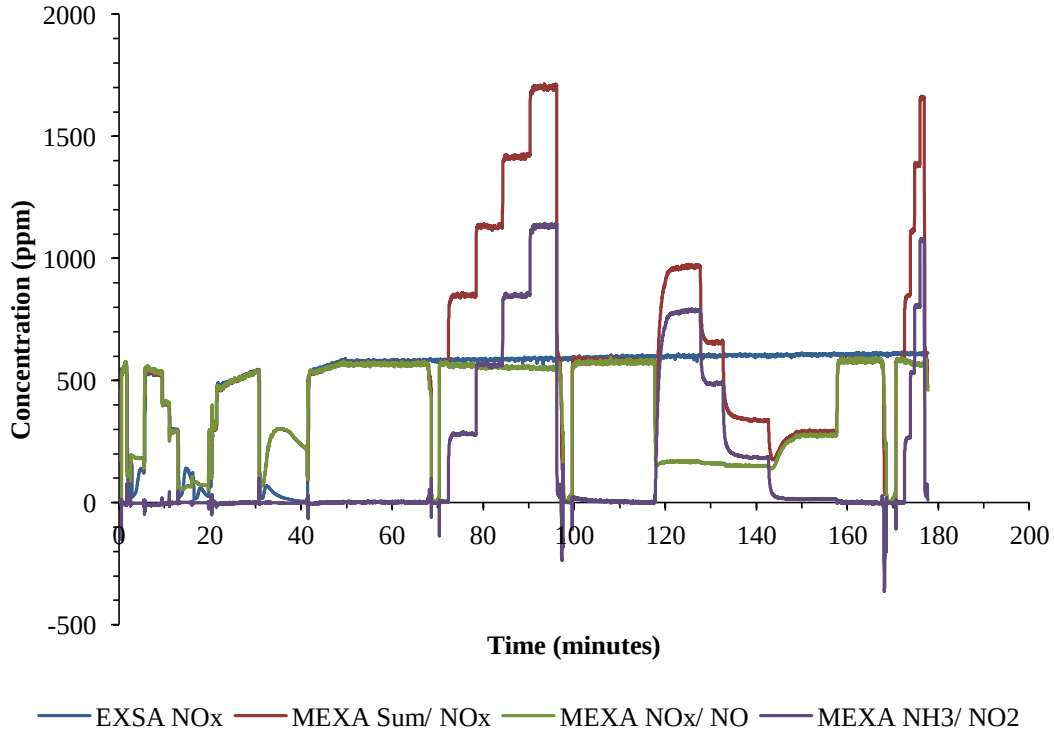

A3.22: Periodic log for the 45.5mm brick, NO_2: NO_x = 0.64, sampling mode: NH_3 mode.

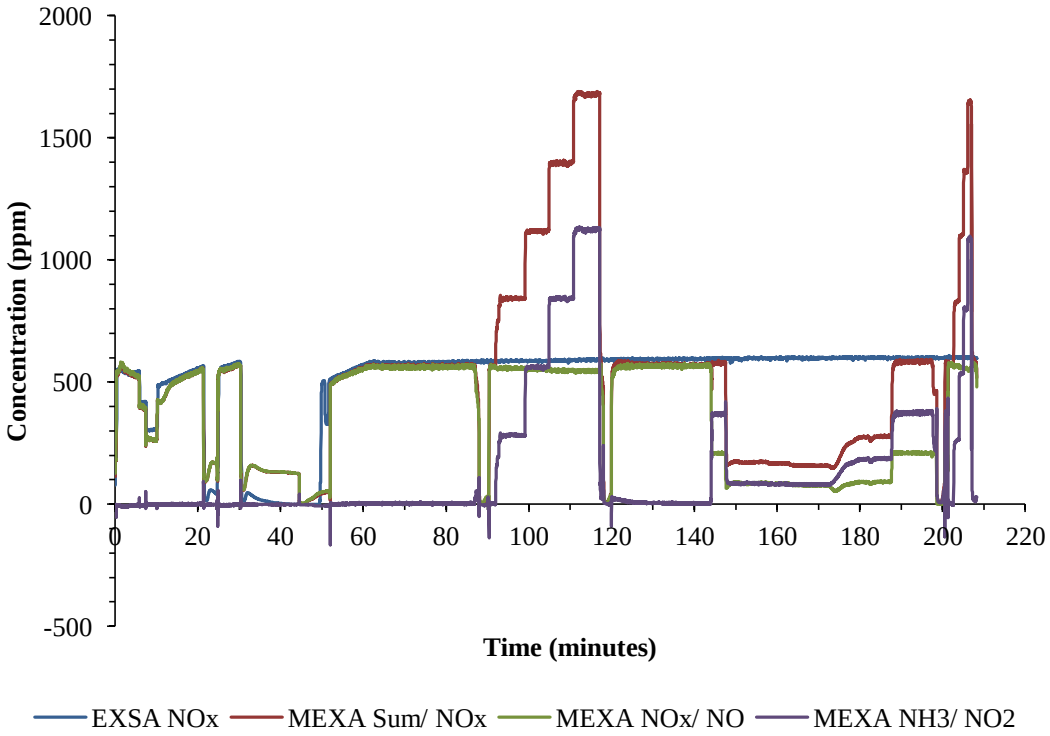

A3.23: Periodic log for the 45.5mm brick, NO_2: NO_x = 0.64, sampling mode: NO_2 mode.

The periodic log for the transient tests with no DOC in the exhaust is presented in A4.19, unlike the tests described in A4.14 – A4.18, both MEXA measurement modes were used. The MEXA was calibrated before stages 2, 5, and 7, as well as before and after the test. The sampling stages are described in A4.20.

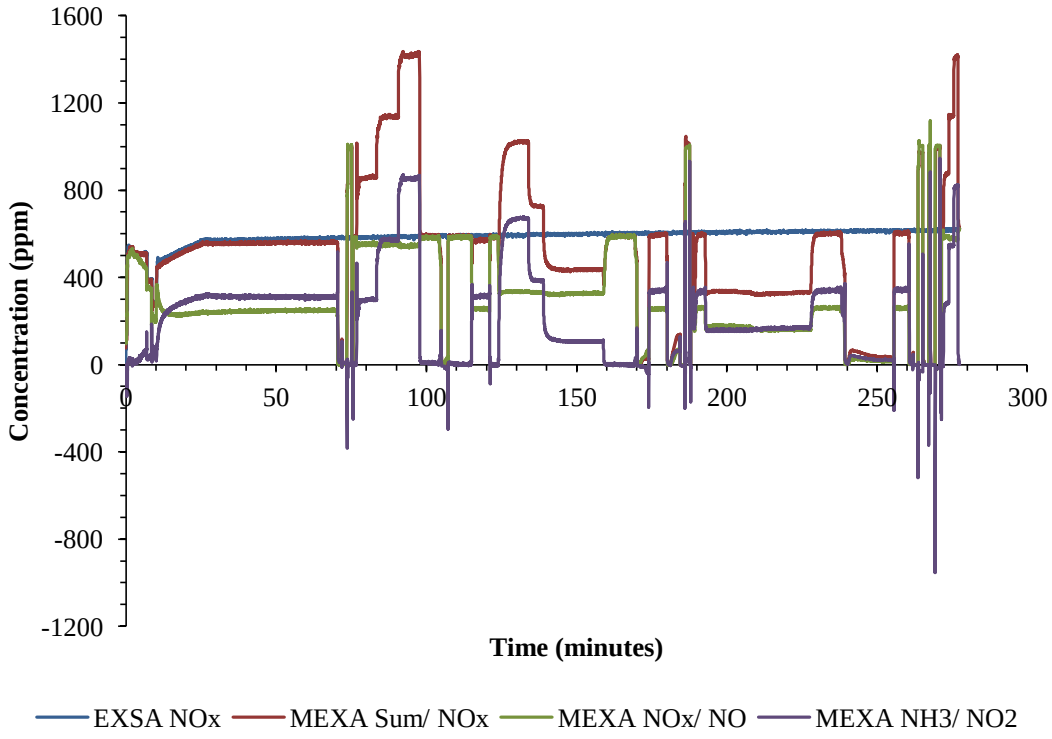

A3.24: Periodic log for the 45.5mm brick, NO_2: NO_x = 0.07, both NH_3 and NO_2 modes were used during this test.

Stage Number	MEXA Mode	MEXA Position	Gas Injection (α_1)	Description
1	NH_3 Mode	Upstream of SCR	-	Engine warm-up
2	NH_3 Mode	Upstream of SCR	0.5, 1.0, 1.5	Flowmeter setting check, and scrubber check
3	NO_2 Mode	Upstream of SCR	-	NO_2: NO_x sampling stage
4	NH_3 Mode	Downstream of SCR	0.5, 1.0, 1.5	First sampling stage
5	NO_2 Mode	Upstream of SCR	-	NO_2: NO_x sampling stage
6	NO_2 Mode	Downstream of SCR	0.5, 1.0, 1.5	Second sampling stage
7	NO_2 Mode	Upstream of SCR	-	NO_2: NO_x sampling stage
8	NH_3 Mode	Upstream of SCR	0.5, 1.0, 1.5	Scrubber check

A3.24: Warm-up and sampling stage descriptions. The gas injection column refers to α, which is the NH_3: NO_x ratio.

Appendix 3.5

The method for determining the amount of ammonia stored on the catalyst washcoat is presented in Appendix 3.5. The calculations were only carried out for the first ammonia injection stage. A3.25 plots one of the transient tests that was undertaken.

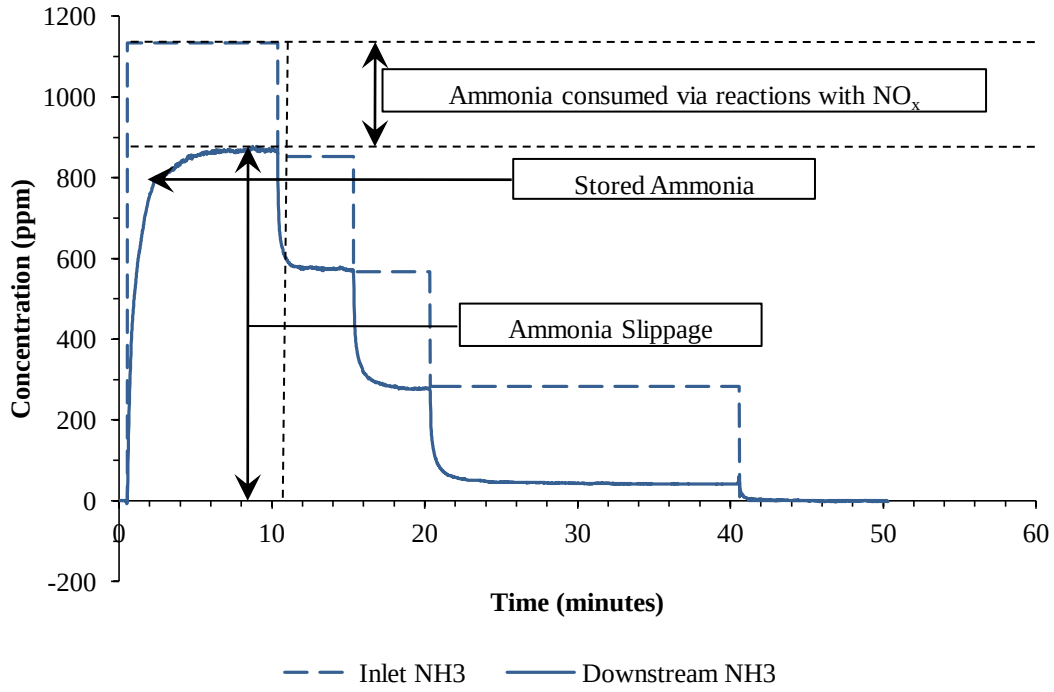

A3.25: Transient ammonia plot.

It is observed that the steady-state NO_x response time is fairly instantaneous when compared with that of the ammonia, thus it is ignored.

Ammonia adsorption is calculated via equation (90) below, where $m_{NH3\text{-}consumed}$ (in grams), is the steady-state ammonia consumption via SCR reactions; this is assumed to have a very fast steady-state response time:

$$m_{NH3-ads} = m_{NH3-inlet} - m_{NH3-slip} - m_{NH3-consumed} \quad \text{(90)}$$

Equation (91) and equation (92) calculate the total inlet ammonia (g), and the total amount of ammonia consumed via SCR reactions (g) respectively, where t_{STAGE} is the time of that particular stage in seconds, and C_{NH3} is the ammonia concentration expressed as a mass fraction:

$$m_{NH3-inlet} = MFR \times t_{STAGE} \times C_{NH3-inlet} \quad \text{(91)}$$

$$m_{NH3-consumed} = MFR \times t_{STAGE} \times \left(C_{NH3-inlet} - C_{NH3-STEADY-STATE} \right) \quad \text{(92)}$$

Ammonia slip, denoted by $C_{NH3\text{-}slip}$, (in ppm) is calculated from the area under the downstream ammonia curve, which can be broken down into trapezoids. The length is determined via equation (93), where λ is the logging interval, which for all tests, was 1Hz:

$$m_{NH3-Slip} = \frac{\overset{*}{m}\left[\frac{1}{\lambda}\right]}{2} \times \sum_{t=\frac{1}{\lambda}} \left[C_{NH3-t} + C_{NH3-2t} \right] + \left[C_{NH3-2t} + C_{NH3-3t} \right] + \ldots \quad (93)$$

Appendix 3.6

A3.26 plots the decrease in the upstream NO_x upstream of the SCR as discussed in Section 6.4. The objective of this analysis was determine the influence of any reactions involving NO_2, ammonia, and water in the gas phase upstream of the SCR, as well as determine the working efficiency of the ammonia scrubbers.

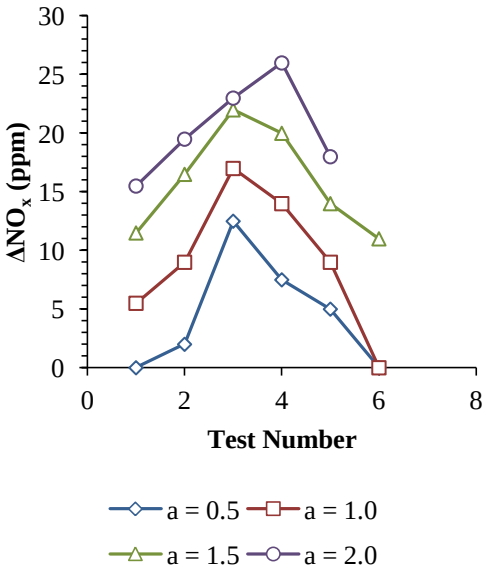

A3.26: ΔNO_x plotted against the test number.

A3.27 displays the test numbers, test descriptions, and their corresponding NO_2: NO_x ratios.

Test Number	Date	Brick Length	NO_2: NO_x	MEXA Measurement Mode
	dd-mm-yyyy	mm		
1	23-07-2010	30	-	NH_3 Mode
2	28-07-2010	30	0.60	NO_2 Mode
3	02-08-2010	45.5	-	NH_3 Mode
4	03-08-2010	45.5	0.64	NO_2 Mode
5	21-10-2010	30	0.07	Both Modes

A3.27: Test descriptions and NO_2: NO_x ratios.

Equation (94) is used to determine whether the ammonia scrubbers are functioning at 100% efficiency, if ΔNO_x: ΔNH_3 is above 1.0, then it is possible that the efficiency is less than 100%:

$$\Delta NO_x : \Delta NH_3 = \frac{C_{i-in} - C_{i-out}}{C_{NH3-in} - C_{NH3-out}} \quad (94)$$

Appendix 4: Steady-State CFD Analysis Results

Appendix 4.1 Steady-State Species Concentrations for CFD Base Cases

Brick Length	Space Velocity	α_1	NO_x	NO	NO_2	NH_3	θ
mm	h^{-1}		ppm	ppm	ppm	ppm	
0	-	0.5	580	310	270	295	-
		1.0	583	311	272	590	-
		1.5	587	313	274	886	-
12	1494049	0.5	519	281	238	233	0.0380
		1.0	466	256	210	472	0.0918
		1.5	420	235	185	718	0.1639
24	724585	0.5	480	263	217	194	0.0279
		1.0	393	222	171	398	0.0660
		1.5	319	187	132	616	0.1272
36	474515	0.5	450	248	202	164	0.0195
		1.0	336	194	142	340	0.0439
		1.5	238	147	91	534	0.0969
48	351410	0.5	424	236	188	138	0.0174
		1.0	289	171	118	292	0.0458
		1.5	173	114	59	468	0.1468
60	278381	0.5	402	225	177	116	0.0167
		1.0	248	151	97	251	0.0549
		1.5	121	86	35	415	0.2725
72	230131	0.5	385	217	168	98	0.0162
		1.0	214	134	80	216	0.0682
		1.5	89	68	21	383	0.3010
84	195922	0.5	369	209	160	83	0.0156
		1.0	184	119	65	186	0.0849
		1.5	72	58	14	365	0.3169
96	170427	0.5	356	203	153	69	0.0148
		1.0	158	106	52	160	0.1049
		1.5	61	51	10	354	0.3249
108	150708	0.5	345	198	147	58	0.0138
		1.0	136	95	41	137	0.1280
		1.5	53	46	7	346	0.3293
120	135010	0.5	335	193	142	49	0.0126
		1.0	118	86	32	119	0.1541
		1.5	47	42	5	339	0.3317
132	122222	0.5	328	190	138	41	0.0114
		1.0	102	77	25	103	0.1828
		1.5	32	38	4	335	0.3332
144	111609	0.5	321	186	135	34	0.0102
		1.0	89	70	19	89	0.2122
		1.5	38	35	3	331	0.3341
156	102662	0.5	316	184	132	28	0.0091
		1.0	78	64	14	78	0.2376
		1.5	35	33	2	327	0.3348
168	95018	0.5	311	182	129	24	0.0079
		1.0	69	58	11	69	0.2544
		1.5	32	30	2	324	0.3352
180	88415	0.5	307	180	127	20	0.0069
		1.0	62	54	8	62	0.2640
		1.5	29	28	1	322	0.3355

A4.1: Species concentrations and fraction of ammonia storage sites taken up by ammonia (θ) for and NO_2: NO_x ratio = 0.46, when Ω = 200mol-sites.m^{-3}.

Brick Length	Space Velocity	α_1	NO_x	NO	NO_2	NH_3	θ
mm	h^{-1}		ppm	ppm	ppm	ppm	
0	-	0.5	581	310	271	297	-
		1.0	587	313	274	593	-
		1.5	591	315	276	890	-
12	1494049	0.5	496	270	226	210	0.0367
		1.0	423	236	187	429	0.0999
		1.5	361	207	154	659	0.2007
24	724585	0.5	447	247	200	162	0.0249
		1.0	332	193	139	336	0.0715
		1.5	239	149	90	535	0.1870
36	474515	0.5	412	230	182	126	0.0163
		1.0	265	160	105	268	0.0488
		1.5	149	102	47	443	0.2110
48	351410	0.5	385	217	168	98	0.0141
		1.0	214	135	79	216	0.0562
		1.5	93	70	23	386	0.2872
60	278381	0.5	364	207	157	77	0.0131
		1.0	173	114	59	174	0.0748
		1.5	66	54	12	359	0.3106
72	230131	0.5	347	199	148	60	0.0120
		1.0	140	97	43	141	0.1042
		1.5	52	45	7	344	0.3220
84	195922	0.5	333	192	141	46	0.0108
		1.0	113	83	30	114	0.1381
		1.5	44	39	5	335	0.3279
96	170427	0.5	323	187	136	36	0.0095
		1.0	92	71	21	92	0.1804
		1.5	37	34	3	329	0.3311
108	150708	0.5	315	184	131	28	0.0081
		1.0	76	62	14	76	0.2225
		1.5	32	30	2	324	0.3329
120	135010	0.5	309	181	128	21	0.0068
		1.0	64	54	10	63	0.2494
		1.5	29	27	2	320	0.3339
132	122222	0.5	304	178	126	16	0.0055
		1.0	55	48	7	54	0.2611
		1.5	25	24	1	317	0.3346
144	111609	0.5	300	176	124	13	0.0045
		1.0	48	43	5	47	0.2680
		1.5	23	22	1	314	0.3350
156	102662	0.5	297	175	122	10	0.0036
		1.0	42	39	3	41	0.2707
		1.5	20	19	1	312	0.3353
168	95018	0.5	295	174	121	7	0.0028
		1.0	37	35	2	37	0.2718
		1.5	18	18	0	310	0.3356
180	88415	0.5	293	173	120	6	0.0022
		1.0	34	32	2	33	0.2720
		1.5	16	16	0	308	0.3357

A4.2: Species concentrations and fraction of ammonia storage sites taken up by ammonia (θ) for and NO_2: NO_x ratio = 0.46, when Ω = 300mol-sites.m^{-3}.

Brick Length	Space Velocity	α_1	NO_x	NO	NO_2	NH_3	θ
mm	h^{-1}		ppm	ppm	ppm	ppm	
0	-	0.5	583	311	272	298	-
		1.0	589	314	275	596	-
		1.5	595	317	278	895	-
12	1494049	0.5	477	261	216	191	0.0353
		1.0	387	219	168	392	0.1085
		1.5	314	185	129	611	0.2445
24	724585	0.5	422	235	187	136	0.0225
		1.0	283	170	113	287	0.0803
		1.5	187	124	63	482	0.2697
36	474515	0.5	384	217	167	98	0.0141
		1.0	213	135	78	215	0.0587
		1.5	106	79	27	399	0.2854
48	351410	0.5	359	205	154	71	0.0117
		1.0	162	109	53	163	0.0744
		1.5	68	55	13	361	0.3068
60	278381	0.5	329	195	144	52	0.0102
		1.0	124	89	35	124	0.1078
		1.5	50	43	7	342	0.3193
72	230131	0.5	324	188	136	37	0.0088
		1.0	94	72	22	95	0.1562
		1.5	39	35	4	331	0.3263
84	195922	0.5	314	183	131	27	0.0073
		1.0	73	60	13	73	0.2109
		1.5	32	30	2	324	0.3302
96	170427	0.5	307	180	127	19	0.0058
		1.0	58	50	8	58	0.2462
		1.5	27	25	2	319	0.3323
108	150708	0.5	301	177	124	14	0.0045
		1.0	48	43	5	47	0.2603
		1.5	23	22	1	315	0.3336
120	135010	0.5	297	175	122	10	0.0034
		1.0	40	37	3	40	0.2660
		1.5	20	19	1	311	0.3343
132	122222	0.5	295	174	121	7	0.0025
		1.0	35	33	2	34	0.2681
		1.5	17	17	0	309	0.3349
144	111609	0.5	293	173	120	5	0.0018
		1.0	31	29	2	29	0.2685
		1.5	15	15	0	306	0.3352
156	102662	0.5	291	172	119	3	0.0013
		1.0	27	26	1	26	0.2679
		1.5	13	13	0	304	0.3355
168	95018	0.5	290	171	119	2	0.0010
		1.0	24	23	1	23	0.2668
		1.5	11	11	0	303	0.3357
180	88415	0.5	289	171	118	2	0.0007
		1.0	21	20	1	20	0.2653
		1.5	10	10	0	301	0.3359

A4.3: Species concentrations and fraction of ammonia storage sites taken up by ammonia (θ) for and NO_2: NO_x ratio = 0.46, when Ω = 400mol-sites.m^{-3}.

Brick Length	Space Velocity	α_1	NO_x	NO	NO_2	NH_3	θ
mm	h^{-1}		ppm	ppm	ppm	ppm	
0	-	0.5	585	312	273	300	-
		1.0	593	316	277	599	-
		1.5	599	319	280	899	-
12	1494049	0.5	460	253	207	174	0.0338
		1.0	356	205	151	360	0.1175
		1.5	276	167	109	571	0.2864
24	724585	0.5	402	226	176	115	0.0204
		1.0	245	152	93	248	0.0919
		1.5	156	108	48	450	0.3007
36	474515	0.5	365	208	157	78	0.123
		1.0	174	116	58	176	0.0731
		1.5	88	69	19	381	0.3001
48	351410	0.5	340	196	144	53	0.0097
		1.0	125	90	35	126	0.1004
		1.5	57	48	9	349	0.3130
60	278381	0.5	323	188	135	35	0.0079
		1.0	90	70	20	91	0.1525
		1.5	41	37	4	333	0.3223
72	230131	0.5	311	182	129	24	0.0062
		1.0	66	55	11	66	0.2142
		1.5	31	29	2	323	0.3278
84	195922	0.5	303	178	125	16	0.0047
		1.0	51	45	6	50	0.2480
		1.5	25	24	1	317	0.3310
96	170427	0.5	298	176	122	10	0.0034
		1.0	41	37	4	40	0.2600
		1.5	21	20	1	312	0.3328
108	150708	0.5	295	174	121	7	0.0024
		1.0	33	31	2	33	0.2642
		1.5	18	17	1	309	0.3339
120	135010	0.5	292	173	119	5	0.0017
		1.0	28	27	1	27	0.2653
		1.5	14	14	0	306	0.3345
132	122222	0.5	291	172	119	3	0.0011
		1.0	24	23	1	23	0.2647
		1.5	12	12	0	304	0.3350
144	111609	0.5	289	171	118	2	0.0008
		1.0	21	20	1	20	0.2633
		1.5	10	10	0	302	0.3354
156	102662	0.5	289	171	118	1	0.0005
		1.0	18	18	0	17	0.2614
		1.5	9	9	0	300	0.3356
168	95018	0.5	289	171	118	1	0.0003
		1.0	15	15	0	15	0.2592
		1.5	7	7	0	299	0.3358
180	88415	0.5	288	170	118	1	0.0002
		1.0	14	14	0	13	0.2568
		1.5	6	6	0	297	0.3360

A4.4: Species concentrations and fraction of ammonia storage sites taken up by ammonia (θ) for and NO_2: NO_x ratio = 0.46, when Ω = 500mol-sites.m^{-3}.

Appendix 4.2 Steady-State Species Concentrations for Modified Kinetic Schemes

Brick Length	Space Velocity	α_1	NO_x	NO	NO_2	NH_3	θ
mm	h^{-1}		ppm	ppm	ppm	ppm	
0	-	0.5	583	311	272	298	-
		1.0	589	314	275	595	-
		1.5	594	316	278	893	-
12	1494049	0.5	479	264	215	193	0.0599
		1.0	398	228	170	401	0.1675
		1.5	338	201	137	633	0.3023
24	724585	0.5	425	240	185	138	0.0386
		1.0	297	182	115	299	0.1223
		1.5	222	146	76	515	0.2796
36	474515	0.5	388	223	165	100	0.0243
		1.0	227	147	80	226	0.0863
		1.5	153	97	36	424	0.2746
48	351410	0.5	361	210	151	73	0.0201
		1.0	174	119	55	173	0.1022
		1.5	87	68	19	375	0.2990
60	278381	0.5	342	201	141	53	0.0175
		1.0	135	98	37	133	0.1367
		1.5	62	52	10	351	0.3142
72	230131	0.5	327	194	133	38	0.0150
		1.0	105	80	25	102	0.1811
		1.5	48	42	6	337	0.3230
84	195922	0.5	317	189	128	28	0.0124
		1.0	83	67	16	79	0.2231
		1.5	39	35	4	327	0.3279
96	170427	0.5	309	186	123	20	0.0099
		1.0	68	57	11	63	0.2477
		1.5	33	30	3	321	0.3307
108	150708	0.5	304	183	11	14	0.0076
		1.0	56	49	7	51	0.2588
		1.5	28	26	2	316	0.3323
120	135010	0.5	299	181	118	10	0.0058
		1.0	47	42	5	43	0.2636
		1.5	23	22	1	311	0.3334
132	122222	0.5	297	180	117	7	0.0043
		1.0	40	37	3	36	0.2653
		1.5	20	19	1	308	0.3341
144	111609	0.5	295	179	116	5	0.0031
		1.0	35	33	2	31	0.2653
		1.5	18	17	1	305	0.3345
156	102662	0.5	293	178	115	4	0.0023
		1.0	31	29	2	26	0.2644
		1.5	15	15	0	303	0.3349
168	95018	0.5	292	177	115	3	0.0016
		1.0	27	26	1	23	0.2628
		1.5	13	13	0	301	0.3352
180	88415	0.5	291	177	114	2	0.0012
		1.0	24	23	1	20	0.2607
		1.5	11	11	0	299	0.3354

A4.5: Species concentrations and fraction of ammonia storage sites taken up by ammonia (θ) for and NO_2: NO_x ratio = 0.46 (High Temperature), for CFD scheme [1].

Brick Length	Space Velocity	α_1	NO_x	NO	NO_2	NH_3	θ
mm	h^{-1}		ppm	ppm	ppm	ppm	
0	-	0.5	582	310	272	298	-
		1.0	587	312	275	594	-
		1.5	591	314	277	891	-
12	1494049	0.5	483	272	211	196	0.0984
		1.0	412	245	167	414	0.2491
		1.5	378	232	146	672	0.3308
24	724585	0.5	431	252	179	142	0.0658
		1.0	319	208	111	318	0.1935
		1.5	280	192	88	571	0.3022
36	474515	0.5	393	236	157	104	0.0425
		1.0	247	175	72	245	0.1455
		1.5	194	149	45	482	0.2838
48	351410	0.5	366	225	141	76	0.0354
		1.0	194	149	45	190	0.1780
		1.5	144	121	23	430	0.3013
60	278381	0.5	347	217	130	55	0.0310
		1.0	156	129	27	150	0.2345
		1.5	117	104	13	402	0.3153
72	230131	0.5	332	211	121	40	0.0267
		1.0	130	113	17	123	0.2671
		1.5	100	92	8	385	0.3240
84	195922	0.5	320	206	114	29	0.0222
		1.0	112	102	10	105	0.2810
		1.5	89	84	5	374	0.3289
96	170427	0.5	313	203	110	21	0.0178
		1.0	100	93	7	92	0.2877
		1.5	80	77	3	365	0.3317
108	150708	0.5	307	201	106	15	0.0138
		1.0	91	86	5	83	0.2908
		1.5	73	71	2	358	0.3333
120	135010	0.5	303	199	104	11	0.0105
		1.0	83	80	3	75	0.2921
		1.5	67	66	1	352	0.3343
132	122222	0.5	300	198	102	7	0.0078
		1.0	77	75	2	69	0.2924
		1.5	62	61	1	347	0.3349
144	111609	0.5	298	197	101	5	0.0057
		1.0	71	70	1	63	0.2921
		1.5	58	57	1	342	0.3353
156	102662	0.5	296	196	100	4	0.0041
		1.0	66	65	1	58	0.2915
		1.5	53	53	0	338	0.3355
168	95018	0.5	296	196	100	3	0.0030
		1.0	62	61	1	54	0.2906
		1.5	49	49	0	334	0.3357
180	88415	0.5	294	195	99	2	0.0021
		1.0	59	58	1	50	0.2896
		1.5	46	46	0	331	0.3358

A4.6: Species concentrations and fraction of ammonia storage sites taken up by ammonia (θ) for and NO_2: NO_x ratio = 0.46 (High Temperature), for CFD scheme [2].

Brick Length	Space Velocity	α_1	NO_x	NO	NO_2	NH_3	θ
mm	h^{-1}		ppm	ppm	ppm	ppm	
0	-	0.5	582	310	272	297	-
		1.0	586	311	275	593	-
		1.5	587	311	276	887	-
12	1494049	0.5	489	280	209	201	0.1517
		1.0	436	263	173	437	0.3075
		1.5	424	259	165	718	0.3429
24	724585	0.5	438	264	174	147	0.1054
		1.0	353	234	119	351	0.2358
		1.5	337	228	109	627	0.3090
36	474515	0.5	401	250	151	109	0.0700
		1.0	281	202	79	274	0.1870
		1.5	244	183	61	530	0.2749
48	351410	0.5	374	240	134	80	0.0585
		1.0	225	174	51	216	0.2088
		1.5	182	148	34	465	0.2913
60	278381	0.5	353	232	121	59	0.0512
		1.0	183	151	32	173	0.2471
		1.5	146	126	20	427	0.3080
72	230131	0.5	338	226	112	43	0.0442
		1.0	155	134	21	144	0.2701
		1.5	123	111	12	404	0.3190
84	195922	0.5	327	222	105	31	0.0368
		1.0	135	121	14	123	0.2820
		1.5	109	101	8	389	0.3255
96	170427	0.5	318	219	99	22	0.0297
		1.0	121	111	10	108	0.2881
		1.5	97	92	5	377	0.3293
108	150708	0.5	312	216	96	16	0.0232
		1.0	109	102	7	96	0.2912
		1.5	88	84	4	368	0.3316
120	135010	0.5	308	215	93	11	0.0177
		1.0	100	95	5	87	0.2926
		1.5	81	78	3	360	0.3329
132	122222	0.5	305	214	91	8	0.0132
		1.0	92	89	3	79	0.2929
		1.5	74	72	2	353	0.3338
144	111609	0.5	303	213	90	6	0.0097
		1.0	85	83	2	72	0.2927
		1.5	68	67	1	348	0.3343
156	102662	0.5	301	212	89	4	0.0071
		1.0	80	78	2	66	0.2921
		1.5	63	62	1	342	0.3347
168	95018	0.5	299	211	88	3	0.0051
		1.0	74	73	1	61	0.2912
		1.5	59	58	1	338	0.3350
180	88415	0.5	299	211	88	2	0.0036
		1.0	69	68	1	56	0.2901
		1.5	54	54	0	334	0.3352

A4.7: Species concentrations and fraction of ammonia storage sites taken up by ammonia (θ) for and NO_2: NO_x ratio = 0.46 (High Temperature), for CFD scheme [3].

Brick Length	Space Velocity	α_1	NO_x	NO	NO_2	NH_3	θ
mm	h^{-1}		ppm	ppm	ppm	ppm	
0	-	0.5	586	311	275	302	-
		1.0	586	311	275	594	-
		1.5	587	311	276	887	-
12	1494049	0.5	442	265	177	152	0.2578
		1.0	427	260	167	427	0.3333
		1.5	424	259	165	717	0.3459
24	724585	0.5	378	243	135	85	0.1567
		1.0	341	229	112	338	0.2910
		1.5	336	227	109	625	0.3127
36	474515	0.5	341	229	112	47	0.0874
		1.0	258	191	67	251	0.2352
		1.5	242	182	60	528	0.2794
48	351410	0.5	320	221	99	25	0.0570
		1.0	199	159	40	189	0.2560
		1.5	181	148	33	463	0.2943
60	278381	0.5	310	217	93	13	0.0360
		1.0	161	137	24	150	0.2779
		1.5	145	125	20	426	0.3103
72	230131	0.5	303	214	89	7	0.0212
		1.0	138	122	16	126	0.2905
		1.5	123	111	12	403	0.3210
84	195922	0.5	300	213	87	3	0.0117
		1.0	120	110	10	108	0.2973
		1.5	108	100	8	388	0.3273
96	170427	0.5	298	212	86	2	0.0062
		1.0	108	101	7	96	0.3006
		1.5	96	91	5	376	0.3311
108	150708	0.5	298	212	86	1	0.0032
		1.0	99	94	5	86	0.3020
		1.5	88	84	4	367	0.3332
120	135010	0.5	297	212	85	0	0.0016
		1.0	91	87	4	77	0.3023
		1.5	80	77	3	359	0.3345
132	122222	0.5	297	212	85	0	0.0008
		1.0	84	81	3	70	0.3019
		1.5	74	72	2	353	0.3354
144	111609	0.5	296	211	85	0	0.0004
		1.0	78	76	2	64	0.3012
		1.5	68	67	1	347	0.3359
156	102662	0.5	296	211	85	0	0.0001
		1.0	72	71	1	59	0.3002
		1.5	63	62	1	342	0.3363
168	95018	0.5	296	211	85	0	0.0001
		1.0	67	66	1	54	0.2990
		1.5	59	58	1	337	0.3365
180	88415	0.5	297	211	86	0	0.0000
		1.0	63	62	1	49	0.2977
		1.5	54	54	0	333	0.3367

A4.8: Species concentrations and fraction of ammonia storage sites taken up by ammonia (θ) for and NO_2: NO_x ratio = 0.46 (High Temperature), for CFD scheme [4].

List of Amendments – 18/04/2012

1. General Amendments

- Spelling and grammar checked.
- Page numbers moved to the left-hand side of each page
- Word document and PDF files included

2. Page Specific Amendments

The table below describes the changes made to the thesis and the page numbers that these can be found:

Page Number	Amendment
6	First two paragraphs from the 'Abstract' removed.
6	CFD model explained in greater detail.
8 – 12	Units included in the 'Nomenclature' section.
23 and 117	Reference to BBC removed.
36	Fig 2.13 changed.
42	Fig 2.23 refined.
50	Fig 2.26 is explained in greater detail in paragraphs 1 and 2 (symbols not explained as Fig 2.26 is only there for the purpose of visualisation of species transport).
51	Typo corrected in the description of Fig 2.27.
51	"Solid section" of the model explained in the paragraph next to Fig 2.27.
52	Last bullet point in the section 'Current Gaps in Knowledge': the model is now described as 1D.
55	Description of the 'Froude Texcel V12' included in the paragraph next to Fig 4.2.
68	The descriptions of the user-subroutines have been made clearer.
69	Fig 5.2: a description of the analysis process used in all simulations undertaken in this thesis.
70	Last paragraph: the differences between the experimental catalyst and the CFD porous section explained.
71	Equation (63) explained.
72	Equation (65) explained.
73	Equation (68) explained.
77	Typo at the end of paragraph 3 corrected.

83 - 86	Test repeatability included.
117	Third bullet point in the section ‘Modified Kinetic Schemes’: the term $(1 - \alpha\theta)$ is explained.
119	Top paragraph: adsorption on CLD analyser explained.
133 - 134	Section on calculating the total mass transfer coefficient re-written.
136 - 137	CFD model validation section included as ‘Appendix 2.6’.